SPATIO-TEMPORAL EVOLUTION OF EVAPORATING LIQUID FILMS SHEARED BY A GAS

A THESIS SUBMITTED TO

THE GRADUATE SCHOOL OF ENGINEERING AND SCIENCE

OF BILKENT UNIVERSITY

IN PARTIAL FULFILLMENT OF THE REQUIREMENTS FOR

THE DEGREE OF

MASTER OF SCIENCE

IN

MECHANICAL ENGINEERING

By

Omair A. A. Mohamed

November 2019

Spatio-temporal evolution of evaporating liquid films sheared by a gas
By Omair A. A. Mohamed
November 2019

We certify that we have read this thesis and that in our opinion it is fully adequate, in scope and in quality, as a thesis for the degree of Master of Science.

Luca Biancofiore(Advisor)

Seymur Jahangirov

Mustafa Türkyılmazoğlu

Approved for the Graduate School of Engineering and Science:

Ezhan Karaşan
Director of the Graduate School

ABSTRACT

SPATIO-TEMPORAL EVOLUTION OF EVAPORATING LIQUID FILMS SHEARED BY A GAS

Omair A. A. Mohamed
M.S. in Mechanical Engineering
Advisor: Luca Biancofiore
November 2019

The main purpose of this work is the investigation of the spatio-temporal characteristics of an evaporating liquid film under the influence of inertia, hydrostatic pressure, thermocapillary effects, vapor recoil, and shear stress imparted by a gas. The effects of the shearing gas are included via the introduction of a constant shear agent quantity modeling the effect of a constant shear stress applied along the liquid interface. Subsequently, long wave theory is used to derive an interface evolution equation accounting for all the previous effects which then is used to analyze the linear stability characteristics of the film for different parameter combinations. First a temporal analysis is performed to determine the stable/unstable parameter sets, followed by spatio-temporal analysis to differentiate the absolute/convective stability domains. It is demonstrated that the shear agent acts as a modifier to the base flow's existing inertia and therefore doesn't change perturbation growth rates in a stationary base flow, however it does have a strong effect on the phase speed. Therefore it can cause convective/absolute transitions of thermal instabilities. As for its effect on inertial instabilities, namely the H-mode, positive values of the shear agent promote its growth, while negative ones suppress it, to the point of completely eliminating it for sufficiently negative values. As for the effects of evaporation it is found that the reduction in film height due to evaporation suppresses the advection of perturbations through the film and therefore promotes absolute instabilities.

In order to investigate the non-linear evolution of the interface, the evolution equation is solved numerically. Initially, the interface evolution is simulated for infinitesimal perturbations over a periodic domain for the purposes of validation by comparison to the linear temporal stability results, and also to existing literature. Once the numerical procedure is validated, the non-linear evolution of the interface is studied. Finally, the shear gas's effect on film rupture location

and time are studied where it is found that the shear agent can strongly affect rupture location and time, but doesn't change the self-similar rupture mechanics as the minimum film height approaches zero.

Keywords: Spatio-temporal instability, liquid film, gas shear, evaporation.

ÖZET

BIR GAZLA KESILMIş BUHARLASAN SIVI FILMLERIN UZAMSAL-ZAMANSAL DENGESIZLIGI

Omair A. A. Mohamed
Makine Mühendisliği, Yüksek Lisans
Tez Danışmanı: Luca Biancofiore
Kasım 2019

Bu çalışmanın temel amacı, buharlaşan bir sıvı filmin uzaysal-zamansal özelliklerinin atalet, hidrostatik basınç, termokapiller etkiler, buhar geri tepmesi ve bir gazın verdiği kesme gerilmesi etkisi altında incelenmesidir. Kesme gazının etkileri, ara yüz boyunca uygulanan sabit bir kesme gerilmesinin etkisini modelleyen sabit bir kesme sabiti sayısı eklenmesiyle dahil edilir. Uzun dalga teorisi, önceki tüm etkileri hesaba katan bir arayüz gelişim denklemini türetmek için kullanılır ve bu denklem daha sonra farklı parametre kombinasyonları için filmin doğrusal stabilite özelliklerini analiz etmek için kullanılır. İlk önce kararlı/ kararsız parametre setlerini belirlemek için bir zamansal analiz yapılır, ardından mutlak / konvektif stabilite alanlarını ayırt etmek için uzamsal zamansal analiz yapılır. Kesme sabitinin, baz akışının mevcut ataletine bir modifiye edici görevi gördüğü ve bu nedenle sabit baz durumunda bozulma büyüme oranlarını değiştirmediği, ancak faz hızları üzerinde güçlü bir etkisi olduğu gösterilmiştir. Bu nedenle, termal kararsızlıkların konvektif / mutlak geçişlerine neden olabilir. Ataletsiz dengesizlikler, yani H modu üzerindeki etkisine gelince, kesme sabitinin pozitif değerleri, büyümesini teşvik ederken, negatif olanları onu yeterince negative değerler için tamamen ortadan kaldırma noktasına kadar bastırır. Buharlaşmanın etkileri ile ilgili olarak, buharlaşma nedeniyle film yüksekliğindeki azalmanın, film boyunca bozulmaların baskılanmasını bastırdığı ve bu nedenle mutlak dengesizlikleri arttırdığı bulunmuştur.

Arayüzün doğrusal olmayan gelişimini araştırmak için gelişim denklemi sayısal olarak çözülmüştür. İlk olarak, ara yüz evrimi, lineer zamansal kararlılık sonuçlarıyla ve ayrıca mevcut literatürle karşılaştırılarak doğrulama amacıyla bir periyodik alan üzerinde sonsuz küçük sapmalar için simüle edilir. Sayısal prosedür onaylandıktan sonra, arayüzün doğrusal olmayan gelişimi incelenir. Son olarak, kesme gazının film yırtılma yeri ve süresi üzerindeki etkisi incelenmiştir, kesme

sabitinin yırtılma yeri ve zamanını güçlü bir şekilde etkileyebileceği, ancak minimum film yüksekliği sıfıra yaklaştıkça kendi kendine benzer yırtılma mekaniğini değiştirmeyeceği tespit edilmiştir.

Anahtar sözcükler: Uzamsal-zamansal dengesizlik, sıvı filmi, gaz kesme, buharla, stırma.

Acknowledgement

I want to thank God for blessing me with the opportunity to take a path in life that makes me happy and fulfilled.

I also want to thank my parents for their continuous inspiration, and support, and kind words.

I want to thank my supervisor Dr. Luca Biancofiore for giving the opportunity to work with him despite being away from academia for more than 5 years, and for his continuous guidance during the course of this work.

I want to express my deepest gratitude to my wife Nada for her encouragement, patience, and the sacrifices she makes every single day to help me focus on my work, and also to our little bundle of joy, my daughter Salwa for making our days that much brighter.

I also want to thank my brothers Hammam and Derar for all the help and assistance they provided and whom without my path to this point would have been much harder.

I want to thank my colleague Humayun Ahmed for all the fruitful discussions we have, and Dr. Micheal Dallaston for providing the initial MATLAB code and on many occasions taking the time to meet and discuss my research's progress.

I also want to thank the Scientific and Technological Research Council of Turkey (TÜBİTAK) for supporting this project.

Contents

List of Figures

Nomenclature

Dimensionless numbers

$\bar{M}$	modified Marangoni number
C	capillary number
D	density ratio
E	evaporation number
K	equilibrium parameter
M	Marangoni number
P	Prandtl number
Re	Reynolds number
S	nondimensional surface tension
V_r	vapor recoil strength parameter

Greek Letters

α	accommodation coefficient
β	flow inclination angle
χ	thermal diffusivity
δ	Dirac impulse

κ mean interface curvature

μ dynamic viscosity

ν kinematic viscosity

ω angular frequency

ρ mass density

σ surface tension

τ shear agent quantity

Indices

$\blacksquare_g$ gas quantity $\blacksquare$

$\blacksquare_i$ imaginary part of $\blacksquare$

$\blacksquare_v$ vapor quantity $\blacksquare$

Latin Letters

ℓ base flow horizontal characteristic length

J evaporation mass flux

k thermal conductivity

L latent heat of evaporation

T temperature

T_i interface temperature

T_s saturation temperature

T_w solid wall temperature

u streamwise velocity component

v spanwise velocity component

w cross-stream velocity component

$\bar{h}$ base flow height

$\mathbf{n}$ normal unit vector

$\mathbf{P}$ deviatoric stress tensor

$\mathbf{S}$ strain rate tensor

$\mathbf{T}$ general stress tensor

$\mathbf{t}$ tangent unit vector

$\mathbf{u}$ general velocity vector

F body force vector

g gravitational acceleration

k wavenumber

M_W molecular weight

p pressure

R_g universal gas constant

Operators

∇ gradient operator

∇^2 Laplacian operator

∇_s surface gradient operator

$\Re\{\blacksquare\}$ real part of $\blacksquare$

D/Dt material derivative operator

Chapter 1

Introduction

1.1 Motivation

Liquid films have many important technological applications across a wide range of industries. Examples include rocket engine nozzle protection, the cooling of electronics, coating processes, distillation operations, combustion engines, and even emerging technologies such as post-combustion carbon dioxide capture. The properties of the liquid films utilized in these systems significantly affect their performance and efficiency, which if enhanced can result in large economic and environmental gains. For example, the power consumed in distillation processes used in chemical separation amounts to 10% of the entire industrial energy consumption in the United States [1].

The shape of a liquid film's interface has a significant effect on its performance in the system it is part of. Some applications require the film's interface to remain uniform such as coating processes, while in others it is desirable for it to be dynamic. For example, studies have showed that the heat/mass transport across a film can potentially increase by 10-100% when the film surface is wavy as opposed to being flat [2]. Therefore, the evolution of a liquid film's interface has garnered significant attention, particularly investigating the domains for which it

is stable/unstable to disturbances by means of stability theory. The importance of these studies is further enhanced by the fact that they can shed light on the origins of turbulence in liquid films since some finite turbulent structures can be traced back to specific linear instabilities [3, 4].

The dynamics of evaporating liquid films sheared by a gas are strongly tied to phenomena such as flooding, which affects the performance of systems including gas-liquid contactors and nuclear reactors, and therefore forming a better understanding of them is of significant interest.

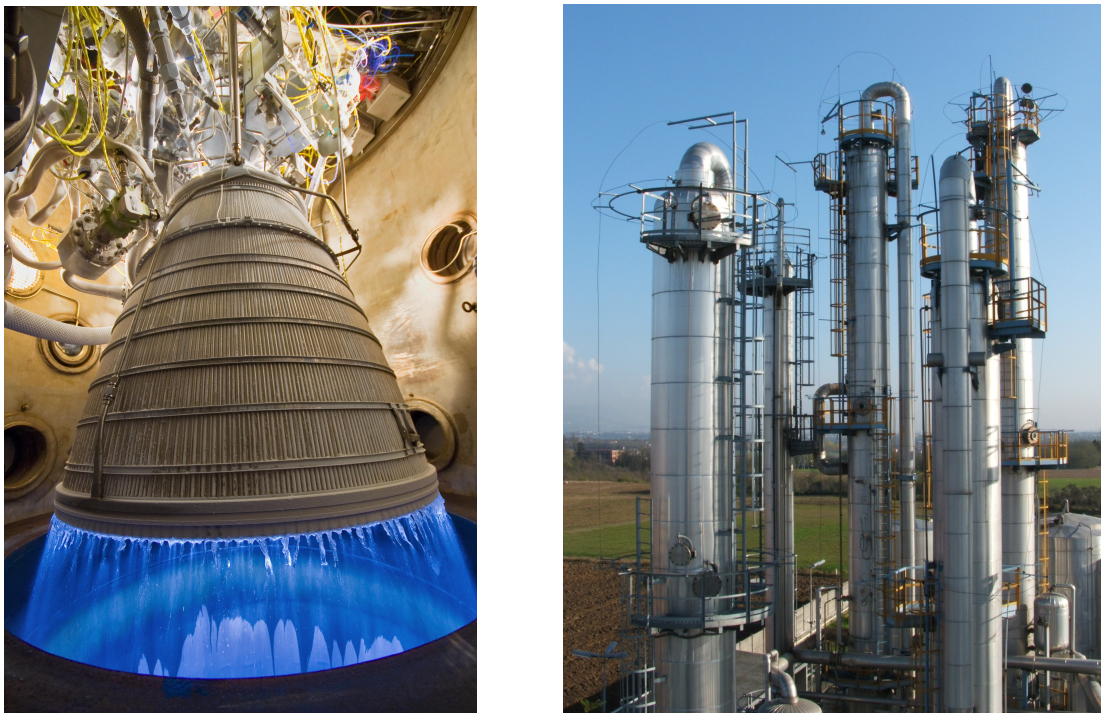

Figure 1.1: Technological applications utilizing evaporating liquid films sheared by a gas. (a) The Common Extensible Cryogenic Engine (CECE)[1]. (b) Industrial distillation towers [2].

[1]https://upload.wikimedia.org/wikipedia/commons/8/8a/Common_Extensible_Cryogenic_Engine.jpg

[2]https://upload.wikimedia.org/wikipedia/commons/c/cc/Colonne_distillazione.jpg

1.2 Background

A liquid film flowing down an inclined surface is influenced by many different forces, such as gravitational acceleration, hydrostatic pressure, inertia, surface tension and its gradients, evaporation, and shear stress; and it is the result of the competition between these different forces which determines flow's ultimate behavior. The dynamics of this contest are complex and the forces participating in it depend on the film's flow domain. For example, at low Reynolds numbers the competition occurs between the destabilizing effects of thermocapillarity and vapor recoil against the stabilizing forces of hydrostatic pressure and surface tension. On the other hand, for relatively larger Reynolds numbers, the competition is mainly between viscosity and inertial effects. Several of these instability modes arising in the different flow domains have been identified and explained by various efforts as summarized ahead.

Surface wave instability

This type of instability, first officially documented by Kapitza [5, 6], takes the form of streamwise long-wave deformations of the film's surface and is therefore suitably called the *surface wave instability*, often called the H-mode. This is a purely hydrodynamic phenomenon resulting from the balance between streamwise gravitational acceleration which pulls the liquid in the streamwise direction, cross-stream gravitational acceleration which manifests itself through the stabilizing hydrostatic pressure, and inertia.

The H-mode instability mechanism is explained as follows. If the film's surface is perturbed upwards at a point on the film's surface, then the base flow's semi-parabolic velocity profile dictates that the fluid velocity at this point on the crest is larger than it at the trough, which results in fluid being drawn towards the crest. As this is occurring, the base flow's inertia delays its adjustment to the new flow profiles such that the flow behind the crest does not decelerate fast enough and that under it does not accelerate fast enough, leading to the accumulation

of fluid under the crest causing it to rise even further. However, the heightened film surface causes an increase in hydrostatic pressure which tries to push the fluid away from under the crest. It is the balance between these two reflexes which determines whether the perturbation grows further or decays; if inertia is dominant enough such that there is a net accrual of fluid under the crest then the perturbation grows and the flow is unstable. On the other hand, if the outflux of fluid from under the crest due to the hydrostatic pressure increase is large enough, the perturbation decays and the flow is stable.

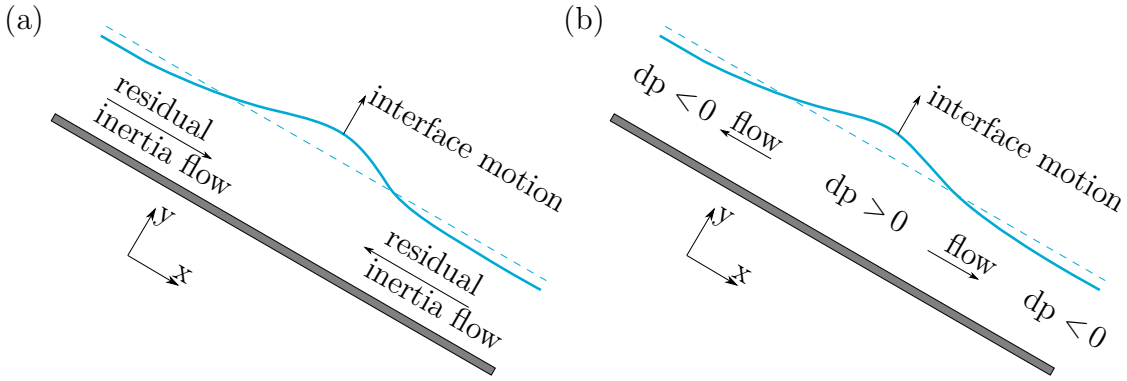

Figure 1.2: H-mode instability mechanism. The dashed line represents the unperturbed base flow height. (a) Accumulation of fluid under the perturbation crest due to inertia. (b) Outflow of fluid from under the perturbation crest due to the increase in hydrostatic pressure.

Thermocapillary instability

Temperature gradients across a liquid film can result in nonuniform surface tension along its interface, causing specific patterns of fluid motion called the *Marangoni effect*, also known as the *thermocapillary effect*. This effect results in two different instability modes named the *P-mode* and the *S-mode* as first classified by Goussis and Kelly in [7]. The P-mode instability is also known as the "Marangoni-Bernard instability" and takes the form of "steady convection rolls" or hexagonal square cells whose size is of the same order of magnitude as the film's thickness, and is classified as a short wave instability [8, 9]. On the other hand, the S-mode takes the form of long-wave surface deformations on a scale

much larger than the film's thickness, and is named the *long-wave Marangoni instability* [10].

The mechanism of the S-mode instability can be explained by considering a liquid film above a surface heated from below, which results in a temperature gradient across the film's thickness. If the film's interface is perturbed downwards towards the plate, then the perturbation's trough will be closer to the heated plate than the crests and will therefore have a higher temperature. Now under the assumption that the liquid's surface tension reduces with temperature, as is the case for most liquids, the surface tension at the trough will consequently be lower than it at the crest. This will result in the fluid being pulled from troughs towards the crests by the stronger surface tension forces, lowering the height of the former, and increasing that of the latter. This motion amplifies the original perturbation and can eventually lead to the formation of dry spots in the locations where the film ruptures at the troughs. However, this instability mechanism has to compete against the stabilizing effect of hydrostatic pressure which tends to push the fluid away from under the crest, and the final fluid state is determined by the dominant effect.

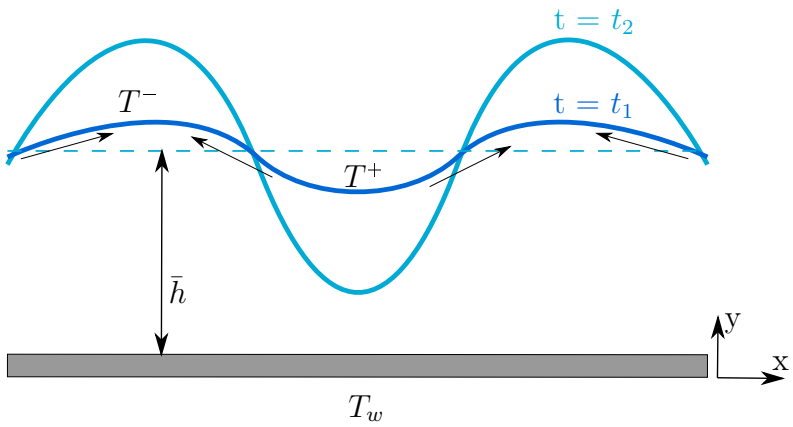

Figure 1.3: The thermocapillary instability mechanism. T^+ and T^- denote higher and lower interface temperatures, respectively, and $t_1 < t_2$. The dashed line represents the unperturbed base flow height.

Evaporation instability

The evaporation instability is caused by the vapor recoil imparted on the liquid interface by the departing vapor. The vapor molecules accelerate greatly when they leave the liquid interface as dictated by mass conservation; since the large difference in density between the liquid and gas phases is compensated for by the large velocity of the vapor molecules. Keeping this in mind, if the liquid interface is perturbed bringing it closer to the heated wall, then the evaporation rate at this trough will increase due to the liquid interface having a higher temperature, and consequently the trough will experience stronger vapor recoil, since its strength is proportional to the evaporation rate. The ensuing pressure rise under the trough will force liquid outwards towards the crests further increasing the disturbance's amplitude and amplifying the perturbation.

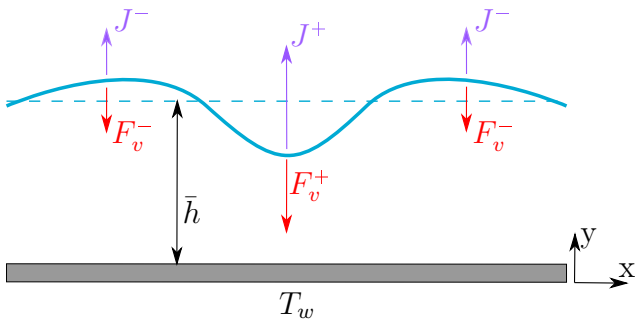

Figure 1.4: The evaproation instability mechanism. J^+, J^- and F_v^+, F_v^- denote higher and lower evaporation mass flux and vapor recoil force, respectively. The dashed line represents the unperturbed base flow height.

1.2.1 Evaporation model

The evaporation model used in this work follows the procedure in Burelbach et al. [11], which in turn is based on the interface jump conditions derived by Delhaye in [12] combined with a constitutive relationship based on kinetic theory [13], which relates the evaporation mass flux to the local surface temperature in terms of the fluid's physical properties and the deviation from saturation temperature.

In this model, the liquid dynamics are decoupled from those of the vapor by considering a limiting case in which the density, viscosity, and thermal conductivity of the liquid are much larger than those of the vapor. Additionally, it is further assumed that the vapor velocity is sufficiently small that both the liquid and the vapor can be treated as incompressible.

1.2.2 Gas shear model

The effects of the shearing gas are introduced into the mathematical system via a shear agent quantity. This variable models the effects of a shearing gas applying a constant shear stress along the entire liquid-gas interface and replaces the complicated gas stress tensor in the interface's shear stress balance with a constant value representing the strength of the applied shear stress. This simplification greatly reduces the complexity of the problem since it becomes no longer required to solve the coupled liquid-gas problem, while also capturing the gas's qualitative effects on the interface's evolution. The derivation of the shear agent quantity is presented in subsection 2.2.2.

1.2.3 Spatio-temporal terminology

The spatio-temporal stability terminology used is that originally developed by Briggs [14] and Bers [15] in their study of plasma instabilities, and later introduced into the stability analysis of fluids by Huerre and Monkewitz [16]. Within this framework, the flow's stability is assessed by examining its long-time response to an impulse source; such that if the disturbance grows but is advected away from its origin the flow is deemed *convectively* unstable. On the other hand, if the disturbance grows at its origin and spreads to contaminate the entire flow domain, the flow is classified as *absolutely* unstable.

1.2.4 Literature review

Several works have investigated the effect of a shearing gas on the stability of a falling liquid film. Vellingiri et al. [17] found that a counter-flowing turbulent shearing gas can cause an initially convective instability, to become absolute and then upward convective with higher gas shear strengths. They found that the cutoff wavenumber either increases, decreases, or displays monotonic behavior depending on the parameter set considered.

Alekseenko et al. [18] studied the effects of a co-flowing and counter-flowing turbulent gas on the stability of a liquid film falling along the inner surface of a vertical tube. Their results showed that increasing the velocity of the counter-flowing gas reduces the cutoff wavenumber, but increases the maximum growth rate. On the other hand, they observed that a co-flowing gas will increase both the cutoff wavenumber and the maximum growth rate.

Lavalle et al. [19] studied the effects of a counter-flowing shearing gas on a liquid film driven by gravity down an inclined plate, specifically focusing on the effects of confinement on the stability of the film. The authors were able to consolidate the different results obtained by previous investigations and attributed the differences to differing levels of flow confinement. They also demonstrated that the H-mode instability can be completely suppressed by strong enough confinement.

Notably, all of the works reviewed considered the effect of the shearing gas on the inertial H-mode instability in flow domains void of any significant thermal effects, whereby this work considers both inertial and thermal instabilities albeit using a simplified analytical model.

1.3 Objectives and outline

The main objective of this work is to investigate the effect of a shearing gas on the stability of an evaporating liquid film, both when stationary and when flowing under the influence of gravity. Specifically, the spatio-temporal behavior of the thermal instabilities i.e the long wave Marangoni S-mode and the E-mode caused by evaporation. This is done by the application of temporal and spatio-temporal analysis methods to study the linear stability characteristics, and a numerical simulation of the interface to study non-linear behavior.

This work is divided as follows. Chapter 2 presents the mathematical model to be used in the stability analysis, including the formulation of the shear agent used to model the effects of the shearing gas. Chapter 3 includes the theoretical concepts behind the temporal and spatio-temporal stability analysis methods used. Chapter 4 presents the parametric study that was performed in order to investigate the effects of the different flow parameters on the stability characteristics of the base flow. Chapter 5 outlines the non-linear evolution results. Finally, chapter 6 summarizes the current findings and also the future outlooks.

Chapter 2

Mathematical model

2.1 Introduction

The flow domain is governed by the fundamental equations of fluid mechanics; the Navier-Stokes momentum equation governing the momentum balance, the continuity equation governing the mass balance, and the Fourier equation governing the energy balance. The solution of this system of equations requires the specification of an appropriate set of boundary conditions on the solid wall and on the gas-liquid interface. The solid wall boundary conditions are relatively simple as they consist of the no slip/no penetration condition for the velocities and a constant value for wall temperature. On the other hand, the liquid-gas interface boundary conditions are more complicated as they involve the balance of several competing forces. In addition to the boundary conditions, a constitutive relationship derived from kinetic theory [13] is required in order to fully close the system.

2.2 Governing equations

Figure 2.1 shows the general liquid film problem considered; an evaporating liquid film being driven by gravity down a solid wall held at a constant temperature, while being sheared by a gas. Note that the schematic depicts a counter-flowing shearing gas, however we consider both counter and co-flowing cases. In the following discussions, quantities associated with the vapor will be denoted with the subscript v, those associated with the gas will be denoted with the subscript g, and quantities associated with the liquid will not be given any particular subscript.

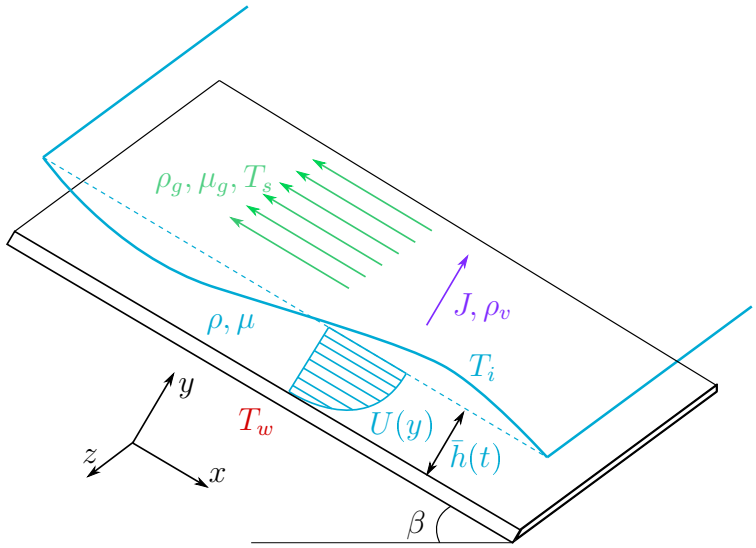

Figure 2.1: Schematic of an evaporating liquid film heated from below, flowing under the influence of gravity while being sheared by a counter-flowing gas. The dashed line represents the unperturbed base flow height.

2.2.1 Vectorized equations

The governing equations along with the complete set of boundary conditions and constitutive relationship can be written as in vector form as:

- Continuity equation

$$\nabla \cdot \mathbf{u} = 0, \tag{2.1a}$$

- Navier-Stokes equation

$$\frac{D\mathbf{u}}{Dt} + \mathbf{u} \cdot \nabla \mathbf{u} = -\frac{1}{\rho}\nabla p + \nu \nabla^2 \mathbf{u} + \mathbf{F}, \tag{2.1b}$$

- Energy equation

$$\frac{DT}{Dt} = \chi \nabla^2 T, \tag{2.1c}$$

- Wall boundary conditions at $y = 0$

  - $u = v = w = 0,$ (2.1d)
  - $T = T_w,$ (2.1e)

- Interface boundary conditions at $y = h(t)$

  - Mass balance

$$J = \rho \left(\mathbf{v} - \mathbf{v_i}\right) \cdot \mathbf{n} = \rho_v \left(\mathbf{v}_v - \mathbf{v_i}\right) .\mathbf{n}, \tag{2.1f}$$

  - Energy balance

$$J \left[\bar{L} + \frac{1}{2}\left(\frac{J}{\rho_v}\right)^2\right] = -k \nabla T \cdot \mathbf{n}, \tag{2.1g}$$

  - General stress balance

$$\frac{J^2}{\rho_v}\mathbf{n} + \left(\mathbf{T} - \mathbf{T}_g\right) \cdot \mathbf{n} = 2\sigma\kappa\mathbf{n} + \nabla_s \sigma, \tag{2.1h}$$

  - Constitutive relationship

$$J = \left(\frac{\alpha \rho_v \bar{L}}{T_s^{\frac{3}{2}}}\right)\left(\frac{M_W}{2\pi R_g}\right)^{\frac{1}{2}} (T_i - T_s), \tag{2.1i}$$

where

$\mathbf{F} = (gsin\beta, -gcos\beta, 0)$, is the gravitational body force vector,

σ_0 is the mean surface tension at the saturaiton temperature,

$\kappa = -\frac{1}{2}\nabla_s \cdot \mathbf{n}$, is the mean interface curvature,

$\mathbf{T} = -p\mathbf{I} + \mathbf{P}$, is the general stress tensor,

$\mathbf{P} = 2\mu\mathbf{S}$, is the deviatoric stress tensor,

$\mathbf{S} = \frac{1}{2}\left(\frac{\partial u_j}{\partial x_i} + \frac{\partial u_i}{\partial x_j}\right)$, is the strain rate tensor,

J, is the evaporation mass flux across the interface,

k, is the thermal conductivity,

$\sigma = \sigma_0 - \gamma\left(T_i - T_s\right)$, is the surface tension function where,

T_i is the liquid interface temperature,

T_s is the saturation temperature,

$\gamma = -d\sigma/dT$ is positive for most liquids,

$\bar{L}$, is the latent heat of vaporization.

$\mathbf{n} = \frac{1}{N}(-\partial_x h, 1)$, is the unit normal vector to the interface in (x, y) with modulus N.

$\mathbf{t_1} = \frac{1}{T_1}(1, \partial_x h)$, is the unit tanget vector to the interface in (x, y) with modulus T_1.

$\mathbf{t_2} = \frac{1}{T_2}(1, \partial_x h)$, is the unit tanget vector to the interface in (x, z) with modulus T_2.

The roles of the aforementioned boundary conditions can be summarized as follows:

1. Mass balance: Gives rise to the kinematic boundary condition which relates the interface height's spatial and temporal gradients to the evaporation mass flux across it.

2. Energy balance boundary condition: Relates the evaporation mass flux across the interface to the temperature gradients along the interface and within the liquid.

3. Stress balance: Relates the stresses across the interface to the forces acting on it, such as pressure, surface tension, thermocapillary forces, and vapor recoil.

4. Constitutive relationship: Relates the evaporation mass flux across the interface to the local surface temperature in terms of the liquid's physical properties.

The following assumptions are now made:

- The liquid's density is constant.
- The liquid is a newtonian fluid.
- The surrounding gas's temperature remains constant and equal to the saturation temperature.
- The boundary between the liquid and the gas has a finite thermal resistance such that the heat transfer across it is governed by *Newton's law of cooling*.
- The contribution of viscous dissipation in the heat equation is neglected.
- Changes in other fluid parameters such as viscosity, thermal conductivity, and thermal diffusivity are negligible.

2.2.2 Shear agent introduction

The shear agent quantity is introduced into the system of equations as follows:

Expanding $\mathbf{T}$ and $\mathbf{T}_g$ in equation (2.1h)

$$\frac{J^2}{\rho_v}\mathbf{n} + \mathbf{P}\cdot\mathbf{n} - p\mathbf{n} - \mathbf{P}_g\cdot\mathbf{n} + p_g\mathbf{n} = 2\sigma\kappa\mathbf{n} + \nabla_s\sigma, \tag{2.2a}$$

Taking the dot product with $\mathbf{n}$ for the normal stress balance

$$\frac{J^2}{\rho_v} + (\mathbf{P}\cdot\mathbf{n})\cdot\mathbf{n} - p - (\mathbf{P}_g.\mathbf{n}).\mathbf{n} + p_g = 2\sigma\kappa, \tag{2.2b}$$

Taking the dot product with $\mathbf{t}_1$ for the shear stress balance in the (x, y) plane

$$(\mathbf{P}.\mathbf{n}) \cdot \mathbf{t}_1 - (\mathbf{P}_g.\mathbf{n}) \cdot \mathbf{t}_1 = \nabla_s \sigma \cdot \mathbf{t}_1, \tag{2.2c}$$

Taking the dot product with $\mathbf{t}_2$ for the shear stress balance in the (x, z) plane

$$(\mathbf{P}.\mathbf{n}) \cdot \mathbf{t}_2 - (\mathbf{P}_g \cdot \mathbf{n}).\mathbf{t}_2 = \nabla_s \sigma \cdot \mathbf{t}_2. \tag{2.2d}$$

The following modifications are now introduced

- The quantity $-(\mathbf{P}_g \cdot \mathbf{n}) \cdot \mathbf{n} + p_g$ in equation (2.2b) is neglected. This is justified by the fact that the time frame during which this model is applied extends from the initial flow conditions in which the gas flow is exactly parallel to the liquid interface's surface, and therefore imparts no normal stress on it; to the end of the initial perturbation growth during which the interface's slope remains relatively small.
- The quantity $(\mathbf{P}_g \cdot \mathbf{n}) \cdot \mathbf{t}_1$ in equation (2.2c) is replaced with the shear agent τ_{xy}.
- The quantity $(\mathbf{P}_g \cdot \mathbf{n}) \cdot \mathbf{t}_2$ in equation (2.2d) is replaced with the shear agent τ_{xz}.

As stated earlier, the magnitudes of the shear agent quantities represent the strength of the shear gas flowing against the interface. On the other hand, their sign represents the momentum difference between the gas and the liquid phases. Positive values of τ_{xy}/τ_{xz} are indicative of a gas which is adding kinetic energy to the liquid interface by flowing along it in the same direction with higher momentum, while negative values of τ_{xy}/τ_{xz} represent cases where the shearing gas is taking away momentum from the liquid interface. This can occur either when the gas is flowing in a direction counter to the liquid's, or flowing in the same direction albeit with lower momentum. This relationship between τ_{xy}/τ_{xz} and the liquid interface's momentum is further highlighted in the base state velocity profile as τ_{xy}/τ_{xz} appears as an algebraic variation to the liquid velocity, according to its sign. Therefore, while the first derivative of the velocity function is zero for

a base flow without any shear stress at the interface, this derivative is positive for positive values of τ and vice versa, as shown in figure 2.2.

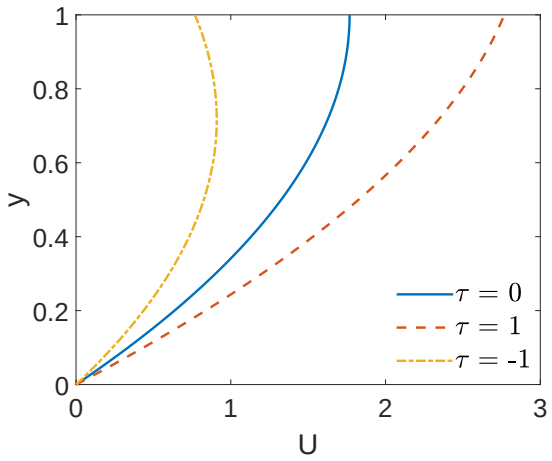

Figure 2.2: The effects of the shear agent on the velocity profile of an arbitrary base flow.

As for the physical interpretation of the shear agent, then by comparing to the results of previous investigations it can deduced that the qualitative effect of the shear agent on an isothermal base flow in this model matches that of a turbulent counter-flowing shearing gas on a strongly confined base flow [19].

2.2.3 Component form equations

The modified system of equations (2.1) is rewritten in component form in order to facilitate the consecutive steps of nondimensionalization and reduction to two dimensions.

- Continuity equation

$$\partial_x u + \partial_y v + \partial_z w = 0, \tag{2.3a}$$

- Navier-Stokes equation

$$\partial_t u + u\partial_x u + v\partial_y u + w\partial_z u = -\frac{1}{\rho}\partial_x p + \nu\left(\partial_{xx}u + \partial_{yy}u + \partial_{zz}u\right) + gsin\beta, \tag{2.3b}$$

$$\partial_t v + u\partial_x v + v\partial_y v + w\partial_z v = -\frac{1}{\rho}\partial_y p + \nu\left(\partial_{xx}v + \partial_{yy}v + \partial_{zz}v\right) - gcos\beta, \tag{2.3c}$$

$$\partial_t w + u\partial_x w + v\partial_y w + w\partial_z w = -\frac{1}{\rho}\partial_z p + \nu\left(\partial_{xx}w + \partial_{yy}w + \partial_{zz}w\right), \tag{2.3d}$$

- Energy equation

$$\partial_t T + u\partial_x T + v\partial_y T + w\partial_z T = \chi\left(\partial_{xx}T + \partial_{yy}T + \partial_{zz}T\right), \tag{2.3e}$$

- Wall boundary conditions at $y = 0$

  - $u = v = w = 0,$ (2.3f)
  - $T = T_w,$ (2.3g)

- Interface boundary conditions at $y = h(t)$

  - Kinematic boundary condition

$$J = \rho\frac{1}{N}\left(-u\partial_x h + v - w\partial_z h - \partial_t h\right), \tag{2.3h}$$

  - Energy balance

$$J\left[\bar{L} + \frac{1}{2}\left(\frac{J}{\rho_v}\right)^2\right] = -\frac{k}{N}\left[-\partial_x h\partial_x T + \partial_y T - \partial_z T\partial_z h\right], \tag{2.3i}$$

  - Normal stress balance

$$\begin{aligned}\frac{J^2}{\rho_v} + \frac{2\mu}{N^2}\Big[&\partial_x u(\partial_x h)^2 + {}^2 + \partial_z w(\partial_z h)^2 + \partial_x h\partial_z h(\partial_x w + \partial_z u)\\ &- \partial_x h(\partial_y u + \partial_x v) - \partial_z h(\partial_z v + \partial_y w) + \partial_y v\Big] - p\\ &= \sigma\left[\frac{\partial_{xx}h[1 + (\partial_z h)^2] + \partial_{zz}h[1 + (\partial_x h)^2] - 2\partial_x h\partial_z h\partial_{xx}h}{N^3}\right],\end{aligned} \tag{2.3j}$$

▫ Shear stress balance (x, y)

$$\frac{\mu}{N}\,[\,2\partial_x h(\partial_y v - \partial_x u) + [1-(\partial_x h)^2](\partial_y u + \partial_x v) \\ - \partial_z h(\partial_x w + \partial_z u) - \partial_x h \partial_z h(\partial_z v + \partial_y w)\,] - \tau_{xy} = (\partial_x \sigma + \partial_x h \partial_y \sigma), \tag{2.3k}$$

▫ Shear stress balance (x, z)

$$\frac{\mu}{N}\,[\,2\partial_z h(\partial_y v - \partial_z w) + [1-(\partial_z h)^2](\partial_z v + \partial_y w) \\ - \partial_x h(\partial_x w + \partial_z u) - \partial_x h \partial_z h(\partial_y u + \partial_x v)\,] - \tau_{xz} = (\partial_z \sigma + \partial_z h \partial_y \sigma), \tag{2.3l}$$

▫ Constitutive relationship

$$J = \left(\frac{\alpha \rho_v \bar{L}}{T_s^{\frac{3}{2}}}\right)\left(\frac{M_W}{2\pi R_g}\right)^{\frac{1}{2}}(T_i - T_s). \tag{2.3m}$$

2.2.4 Nondimensionalization

The following scales are now introduced into the system of equations (2.3)

$$(x, y, z) \to (x^*, y^*, z^*)\bar{h}_0, \tag{2.4a}$$

$$t \to \frac{\bar{h}_0^2}{\nu} t^*, \tag{2.4b}$$

$$(u, v, w) \to (u^*, v^*, w^*)\frac{\nu}{\bar{h}}, \tag{2.4c}$$

$$p \to \frac{\rho \nu^2}{\bar{h}_0^2} p^*, \tag{2.4d}$$

$$T \to T_s + T\Delta T^*, \tag{2.4e}$$

$$J \to \frac{k\Delta T}{\bar{h}_0 \bar{L}} J^*. \tag{2.4f}$$

Where $\Delta T = T_w - T_s$ is the temperature difference across the film and $\bar{h}_0$ is the mean film thickness at initial time t_0. Note that the star notation will be dropped from this point on for conciseness, and the plain variables will be nondimensional unless otherwise stated.

Applying these scales we obtain the following system of equations:

- Continuity equation

$$\partial_x u + \partial_y v + \partial_z w = 0, \tag{2.5a}$$

- Navier-Stokes equation

$$\partial_t u + u\partial_x u + v\partial_y u + w\partial_z u = -\partial_x p + \partial_{xx} u + \partial_{yy} u + \partial_{zz} u + Resin\beta, \tag{2.5b}$$

$$\partial_t v + u\partial_x v + v\partial_y v + w\partial_z v = -\partial_y p + \partial_{xx} v + \partial_{yy} v + \partial_{zz} v - Recos\beta, \tag{2.5c}$$

$$\partial_t w + u\partial_x w + v\partial_y w + w\partial_z w = -\partial_z p + \partial_{xx} w + \partial_{yy} w + \partial_{zz} w, \tag{2.5d}$$

- Energy equation

$$P\left[\partial_t T + u\partial_x T + v\partial_y T + w\partial_z T\right] = \partial_{xx} T + \partial_{yy} T + \partial_{zz} T, \tag{2.5e}$$

- Wall boundary conditions at $y = 0$

  - $u = v = w = 0,$ (2.5f)
  - $T = 1,$ (2.5g)

- Interface boundary conditions at $y = h(t)$

  - Mass balance

$$EJ = \frac{1}{N}\left[-u\partial_x h + v - w\partial_x h - \partial_t h\right], \tag{2.5h}$$

  - Energy balance

$$J + \frac{E^2}{D^2\bar{L}} J^3 = \frac{1}{N}\left[\partial_x h \partial_x T - \partial_y T + \partial_z T\right], \tag{2.5i}$$

  - Normal stress

$$\begin{aligned} -\frac{3}{2}\frac{E^2}{D} J - \frac{2}{N^2}\big[&\partial_x u(\partial_x h)^2 + \partial_z w(\partial_z h)^2 + \partial_x h \partial_z h(\partial_x w + \partial_z u) \\ &-\partial_x h(\partial_y u + \partial_x v) - \partial_z h(\partial_z v + \partial_y w) + \partial_y v\big] + p \\ &= -3S(1 - CT)\left[\frac{\partial_{xx} h[1 + (\partial_z h)^2] + \partial_{zz} h[1 + (\partial_x h)^2] - 2\partial_x h \partial_z h \partial_{xz} h}{N^3}\right], \end{aligned} \tag{2.5j}$$

▫ Shear stress (x, y)

$$2\partial_x h(\partial_y v - \partial_x u) + [1 - (\partial_x h)^2][\partial_y u + \partial_x v] - \partial_z h(\partial_x w + \partial_z u) - \partial_x h \partial_z h(\partial_z v + \partial_y w) - \tau_{xy} = -2\frac{M}{P}\left[\partial_x T - \partial_x h \partial_y T\right] N, \tag{2.5k}$$

▫ Shear stress (x, z)

$$2\partial_z h(\partial_y v - \partial_z w) + [1 - (\partial_z h)^2][\partial_z v + \partial_y w] - \partial_x h(\partial_x w + \partial_z u) - \partial_x h \partial_z h(\partial_y u + \partial_x v) - \tau_{xz} = -2\frac{M}{P}\left[\partial_z T - \partial_z h \partial_y T\right] N, \tag{2.5l}$$

▫ Constitutive relationship

$$KJ = T. \tag{2.5m}$$

The scaling of the system produces the following nondimensional parameters:

Reynolds Number: $Re = \dfrac{g\bar{h}_0^3}{\nu^2}$

Prandtl Number: $P = \dfrac{\nu}{\chi}$

Evaporation Number: $E = \dfrac{k\Delta T}{\rho \bar{L} \nu}$

Density Ratio: $D = \dfrac{3\rho_v}{2\rho}$

Nondimensional latent heat: $L = \dfrac{8\bar{h}_0^2 \bar{L}}{9\nu^2}$

Nondimensional surface tension: $S = \dfrac{\sigma_0 \bar{h}_0^2}{3\rho\nu^2}$

Capillary Number: $C = \dfrac{\gamma \Delta T}{\sigma_0}$

Marangoni Number: $M = \dfrac{\gamma \Delta T \bar{h}_0}{2\mu\chi}$

Dimensionless shear agent: $\tau_{xy} = \dfrac{N\bar{h}_0^2}{\mu\nu}\tau_{xy}$

Dimensionless shear agent: $\tau_{xz} = \dfrac{N\bar{h}_0^2}{\mu\nu}\tau_{xz}$

Equilibrium parameter: $K = \left(\dfrac{kT_i^{3/2}}{\alpha \bar{h}_0 \rho_v \bar{L}^2}\right)\left(\dfrac{2\pi R_g}{M_W}\right)^{1/2}$

The parameter K represents the degree of non-equilibrium at the gas-liquid interface such that $K = 0$ corresponds to the quasi-equilibrium case where $T_i = T_s$ along the liquid-gas interface, and $K^{-1} = 0$ represents a nonvolatile liquid and zero mass flux across the interface.

2.2.5 Reduction to 2D

The main focus of this work is on streamwise perturbations in a stream-wise parallel flow, therefore the three-dimensional scaled system is reduced to two dimensions by setting $w = \partial_z = 0$ in the system of equations (2.5). Note that from this point on, τ_{xy} will be referred to simply as τ since there is no longer a need to distinguish it from τ_{xz}.

- Continuity equation

$$\partial_x u + \partial_y v = 0, \tag{2.6a}$$

- Navier-Stokes equation

$$\partial_t u + u\partial_x u + v\partial_y u = -\partial_x p + \partial_{xx} u + \partial_{yy} u + Re sin\beta, \tag{2.6b}$$

$$\partial_t v + u\partial_x v + v\partial_y v = -\partial_y p + \partial_{xx} v + \partial_{yy} v - Re cos\beta, \tag{2.6c}$$

- Energy equation

$$P\left[\partial_t T + u\partial_x T + v\partial_y T\right] = \partial_{xx} T + \partial_{yy} T, \tag{2.6d}$$

Wall boundary conditions at $y = 0$

- $u = v = 0$, (2.6e)
- $T = 1$, (2.6f)

- Interface boundary conditions at $y = h(t)$

- Kinematic boundary condition

$$EJ = \frac{1}{N}\left[-u\partial_x h + v - \partial_t h\right], \tag{2.6g}$$

- Energy balance

$$J + \frac{E^2}{D^2 L}J^3 = \frac{1}{N}\left[\partial_x h \partial_x T - \partial_y T\right], \tag{2.6h}$$

- Normal stress balance

$$-\frac{3}{2}\frac{E^2}{D}J - \frac{2}{N^2}\Big[\partial_x u\left[(\partial_x h)^2 - 1\right] - \partial_x h(\partial_y u + \partial_x v)\Big] + p = -3S(1 - CT)\left[\frac{\partial_{xx} h}{N^3}\right], \tag{2.6i}$$

- Shear stress balance (x, y)

$$[1 - (\partial_x h)^2][\partial_y u + \partial_x v] - 4\partial_x h \partial_x u - \tau = -2\frac{M}{P}\left[\partial_x T - \partial_x h \partial_y T\right] N, \tag{2.6j}$$

- Constitutive relationship

$$KJ = T. \tag{2.6k}$$

The dimensionless system of equations (2.6) is the main system of equations upon which the rest of this work is based.

Chapter 3

Linear stability methodologies

3.1 Introduction

Linear stability is concerned with the flow's response to infinitesimal perturbations. The condition that the perturbations are infinitesimal results in a system of equations which is linear in the perturbation variables, and this linearity allows analyzing the stability of the system using different methods.

In the long wave domain, a dispersion relationship $D(k, \omega)$ relating a perturbation's wavenumber with the resulting perturbation growth rate and phase speed can be derived and utilized to analyze the flow's spatial, temporal, and spatio-temporal stability. As for perturbations with finite wavenumbers, the linearity again allows the decomposition of the solution into normal modes, leading to the formulation of the Orr-Sommerfeld eigenvalue problem which can then be solved outright using matrix methods, or analyzed using techniques such as continuation.

In both approaches, the type of stability analysis depends on the assumptions made about the nature of the wavenumber k and the angular frequency ω, and the characterization of the flow's stability is based on their values under these

assumptions.

3.2 Temporal stability

In a temporal stability analysis it is assumed that the perturbation is a spatially periodic wave which is either decaying, neutral, or growing in time with respect to a reference frame moving with the wave. To meet this assumption, k is considered to be a real number and ω a complex one. This leads to ω_i being the temporal growthrate which determines whether the base state is temporally stable or not, and ω_r being the wave's angular frequency such that $\omega_r = ck$. A base flow's temporal stability is classified as follows:

- $\omega_i < 0$ indicates that the base flow state is *temporally stable*, and the perturbation decays in time at a rate proportional to ω_i.
- $\omega_i = 0$ indicates that the base flow state is *neutrally stable*, and the perturbation does not grow or decay in time but rather maintains a constant amplitude. The locus of points where $\omega_i = 0$ in a given parameter space forms what is known as the *neutral curve* which divides this parameter space into stable and unstable regions.
- $\omega_i > 0$ indicates that the base state is *temporally unstable*, and the perturbation grows in time at a rate proportional to ω_i.

Temporal stability analysis does not provide any insight as to whether the perturbation is growing in space or not, since the assumed perturbation solution is that of a wave growing or decaying in time, but not in space.

3.3 Spatial stability

In contrast to temporal stability analysis, in spatial stability theory it is assumed that the perturbation originates at a point belonging to the domain with a temporal sinusoidal forcing frequency, and then either grows or decays in space. Therefore ω is constrained to be a real number and k a complex one. In this case $-k_i$ is the spatial growthrate determining whether the base state is spatially stable or not, and again $\omega = ck_r$ relates the forcing frequency to the perturbation wave's phase speed and the real part of its wavenumber. A base flow's spatial stability is classified as follows:

- $k_i > 0$ indicates that the base flow state is *spatially stable*, and the perturbation decays in space at a rate proportional to k_i.
- $k_i = 0$ indicates that the base flow state is *neutrally stable*, and the perturbation does not grow or decay in space but rather maintains a constant amplitude. The locus of points where $k_i = 0$ in a given parameter space forms what is known as the *neutral curve* which divides this parameter space into stable and unstable regions.
- $k_i < 0$ indicates that the base flow state is *spatially unstable*, and the perturbation grows in space at a rate proportional to k_i.

Note that in the description of the temporal and spatial stability frameworks no distinction was made between states that are *temporally* neutrally stable and *spatially* neutrally stable, since a base state which is temporally neutrally stable will also be spatially neutrally stable and vice versa. However, this is not true for general spatio-temporal instability since both ω and k are complex quantities.

3.4 Spatio-temporal stability

In general spatio-temporal stability analysis it is assumed that both the perturbation function's wavenumber and frequency are complex quantities, therefore perturbations can grow both in space and in time. This significantly increases the complexity of the analysis and required the development of a rigorous analytical framework. The approach employed in this work is based on the work of Huerre and Monkewitz [16], which is the inspiration behind the following discussion.

3.4.1 Fundamental concepts

The fundamental idea upon which this formulation of spatio-temporal analysis rests is the representation of the perturbation function, which has multiple spatial dimensions, by a one-dimensional complex scalar field $\psi(x,t)$. Additionally, the response of $\psi(x,t)$ to a source function $S(x,t)$ is governed by a linear operator $\mathbf{L}$ corresponding to the dispersion relationship $D(\omega,k;R)$ governing the perturbation's behavior, where R is a given set of flow parameters. Note that the explicit dependence of $D(\omega,k)$ on R is omitted from here on for conciseness.

$$\mathbf{L}\psi(x,t) = S(x,t). \tag{3.1}$$

By setting $\mathbf{L} = \left(-i\frac{\partial}{\partial_x}, i\frac{\partial}{\partial_t}\right)$ (3.1) becomes

$$D\left(-i\frac{\partial}{\partial_x}, i\frac{\partial}{\partial_t}\right)\psi(x,t) = S(x,t). \tag{3.2}$$

Since $\mathbf{L}$ is homogeneous in space-time, equation (3.2) admits the normal mode solution

$$\psi(x,t) = Ae^{i(kx-\omega t)}. \tag{3.3}$$

By substituting equation (3.3) into equation (3.2) it becomes readily apparent that the evolution of $\psi(x,t)$ as governed by $\mathbf{L}$ is correspondent to the evolution of the perturbation as governed by $D(\omega,k;R)$ since $-i\frac{\partial}{\partial_x} = k$ and $i\frac{\partial}{\partial_t} = \omega$.

Equation (3.2) admits several forms of $S(x,t)$ representing different physical settings, however for the purpose of determining the spatio-temporal nature of $\psi(x,t)$ it is sufficient to set $S(x,t) = \delta(x)\delta(t)$ where δ denotes the Dirac delta. This forms the well known *impulse response problem* where the base state evolves freely after being perturbed at $(x,t) = (0,0)$. In this context, $\psi(x,t)$ is equivalent to the Green function $G(x,t)$ and therefore equation (3.2) can be written as

$$D\left(-i\frac{\partial}{\partial_x}, i\frac{\partial}{\partial_t}\right) G(x,t) = \delta(x)\delta(t). \tag{3.4}$$

The criteria by which the spatio-temporal character of $G(x,t)$ is determined are as follows

- The base flow is linearly *stable* if

$$\lim_{t\to\infty} G(x,t) = 0, \qquad \text{along all rays } \frac{x}{t} = \text{constant}. \tag{3.5}$$

  In this case the impulse response is wave packet which decays as it travels in the (x,t) plane.

- The base flow is linearly *unstable* if

$$\lim_{t\to\infty} G(x,t) = \infty, \qquad \text{along at least one ray } \frac{x}{t} = \text{constant}. \tag{3.6}$$

  In this case the impulse response is a wave packet which grows as it travels in the (x,t) plane.

If the flow is deemed unstable, then the following further distinction named the *Briggs-Bers criterion* can be made:

- The base flow is *convectively* unstable if

$$\lim_{t\to\infty} G(x,t) = 0, \qquad \text{along the ray } \frac{x}{t} = 0. \tag{3.7}$$

  In this case growing wavepacket is convected away from the origin of the source, and initial conditions are recovered at $\psi(0,t)$.

- The base flow is *absolutely* unstable if

$$\lim_{t\to\infty} G(x,t) = \infty, \qquad \text{along the ray } \frac{x}{t} = 0. \tag{3.8}$$

  In this case the wavepacket grows in time at the source's origin and spreads to eventually contaminate the entire domain.

A third spatio-temporal classification exists called *absolutely marginally unstable* behavior, where the perturbation packet's frontal edge spreads downstream of the origin while its rear edge has zero velocity. Graphical depictions of these cases are presented in figure 3.1.

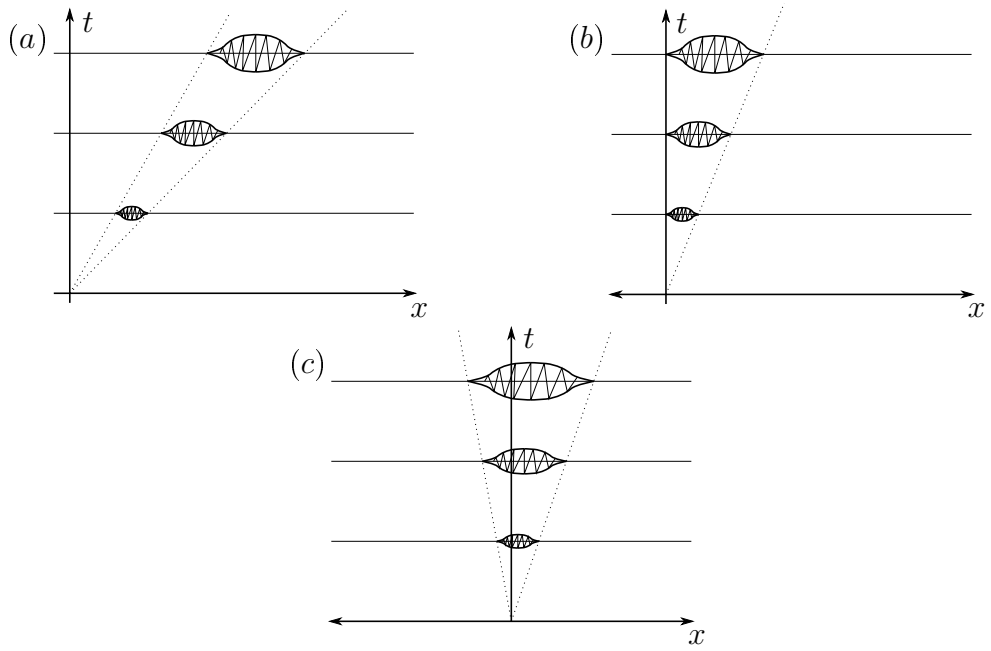

Figure 3.1: The 3 different types of spatio-temporal behavior of a perturbation wave packet in the (x,t) plane. (a) Convectively unstable. (b) Absolutely marginally unstable. (c) Absolutely unstable.

3.4.2 Solving in Fourier space

The following procedure aims at solving equation (3.4) utilizing the concept of transferring a difficult problem into Fourier space, performing the necessary

manipulations, and then returning the solution to physical space. A benefit of this approach is the expression of the final solution in terms of k and ω which are fundamental quantities in stability theory. Note that the following procedure is generalized for any suitable source function $S(x,t)$, so at this stage in the formulation $\psi(x,t)$ is not necessarily $G(x,t)$. The procedure beings by assuming $\psi(k,\omega)$ exists and writing $\psi(x,t)$ as the double inverse Fourier integral

$$\psi(x,t) = \frac{1}{(2\pi)^2}\int_{L_\omega}\int_{F_k}\psi(k,\omega)e^{i(kx-\omega t)}dkd\omega, \tag{3.9}$$

where F_k and L_ω are straight line contours extending along $(-\infty,\infty)$ in the complex k and ω planes respectively. These contours cannot be set arbitrarily as they must meet two requirements; the first of which is to guarantee the convergence of the integrals, while the second, specific to L_ω, is to comply with the principle of *causality.* The essence of this principle is that *"an effect cannot precede its cause"* and therefore

$$\psi(x,t) = 0, \qquad S(x,t) = 0, \qquad \text{for } t < 0. \tag{3.10}$$

This principle plays a significant role in setting the integration contours as will be seen further in the discussion. Once F_k and L_ω are determined, the integrals can be evaluated by closing each line contour with a semicircular arc of infinite radius [20] while ensuring that this additional segment does not contribute to the integral. This is achieved by invoking Jordan's lemma whereby the signs of x and t dictate the side on which the line contours are closed. The constraints on the selection of F_k and L_ω are now explained.

1. **Setting the F_k contour**

   The constraint on the countour F_k arises from the convergence requirement and can be deduced by first examining

   $$\psi(k,t) = \int_{-\infty}^{\infty}\psi(x,t)e^{-ikx}dx. \tag{3.11}$$

   For a line contour F_k lying some finite distance above the real k axis, the integral is well defined for $x \to -\infty$ since the term e^{-ikx} decays exponentially towards this limit. However this term grows exponentially for $x \to +\infty$, and

therefore to ensure convergence $\psi(x,t)$ must decay at least exponentially fast. We can see that F_k meets this requirement by examining

$$\psi(x,t) = \frac{1}{2\pi}\int_{F_k} \psi(k,\omega)e^{ikx}dk, \tag{3.12}$$

where e^{ikx} causes the exponential decay of the integral. Now the exponential growth in (3.11) is balanced by exponential decay and therefore this choice of F_k ensures the convergence of (3.9) under the condition that the choice of L_ω does not violate it. The argument presented above can be reversed for F_k lying a finite distance below the real k axis. Ultimately, to ensure convergence the line countor F_k can be set within a finite strip around the real axis in the complex k space, and for the purposes of the current analysis, it will be chosen to lie exactly on the real k axis. The side on which F_k is closed is determined by examining

$$\psi(x,\omega) = \frac{1}{2\pi}\int_{F_k} \psi(k,\omega)e^{ikx}dk. \tag{3.13}$$

The presence of the exponential term in (3.13) and the fact that the rest of the integrand decays exponentially fast for $\omega \to \infty$ [21] satisfy the conditions set by Jordan's lemma for the integral to vanish on the semicircle. Therefore and in accordance with this proposition, F_k is closed from the above for $x > 0$, and from below for $x > 0$.

2. **Setting the L_ω contour**

We choose the L_ω to lie a finite distance above the real ω axis. It can be shown that this choice of L_ω satisfies convergence requirements by an argument analogous to that made for F_k. However there is an additional constraint on L_ω arising from the causality principle. The latter is not immediately obvious and therefore will be the focus of this discussion. The argument begins by rewriting (3.11) as

$$\psi(k,t) = \frac{1}{2\pi}\int_{L_\omega} \psi(k,\omega)e^{-i\omega t}d\omega. \tag{3.14}$$

In a manner similar to the integral in (3.13), this integral can be solved by closing the line contour L_ω with a semicircular arc of infinite radius since it

also satisfies the conditions required by Jordan's lemma. Therefore, in order for the integral to vanish on the semicircle it must lie below L_ω for $t > 0$ and above it for $t < 0$. This implies that L_ω must be above all the singularities of $\psi(k, \omega)$; since their presence above L_ω would lead to $\psi(k, \omega) \neq 0$ for $t < 0$ when the integral is solved using the residue theorem, which would violate the causality condition. It will be shown in the next part of the derivation that these singularities are actually the poles of $\psi(k, \omega)$ i.e the solutions of the dispersion relationship $D(k, \omega) = 0$. Now that the line contours F_k and L_ω are set, the derivation proceeds ahead.

3. **Solving the problem in Fourier space**

For this current analysis, F_k will be chosen to lie precisely on the real axis in the complex k plane, while L_ω is set a finite distance above the real ω axis in the complex ω plane. Note that other choices of F_k and L_ω are possible as long they meet the necessary conditions. Using a straightforward Fourier transform, the governing equation (3.2) can be written in Fourier space as

$$D(k, \omega)\psi(k, \omega) = S(k, \omega), \tag{3.15}$$

which can be rearranged for $\psi(k, \omega)$ into

$$\psi(k, \omega) = \frac{S(k, \omega)}{D(k, \omega)}. \tag{3.16}$$

Substituting (3.16) into (3.14) we obtain

$$\psi(k, t) = \frac{1}{2\pi} \int_{L_\omega} \frac{S(k, \omega)}{D(k, \omega)} e^{-i\omega t} d\omega. \tag{3.17}$$

Now it is assumed that $D(k, \omega)$ and $S(k, \omega)$ are analytic in k and ω and therefore the only singularities of $\psi(k, t)$ are the solutions of $D(k, \omega)$. We further presume that $D(k, \omega)$ has a single temporal root denoted $\omega(k)$; which is a reasonable assumption for the stability problems to be handled in this thesis. The locus of points $\omega(k)$ represents the image of the contour F_k in the complex ω space, and as dictated by causality, it lies below L_ω to ensure $\psi(k, t) = 0$ for $t < 0$.

The implications of causality

The implications of the principle of causality also appear in the complex k space. The image of L_ω in the complex k space appears as two separate loci of points which must lie on opposite sides of the contour F_k; since an intersection between one of these spatial modes and F_k at a single point would mean that this particular value of k corresponds to a value of $\omega(k)$ intersecting the contour L_ω, which would violate causality. These spatial modes are denoted $k^+(\omega)$ and $k^-(\omega)$ where the $+$ and $-$ superscripts denote modes lying above and below F_k, respectively.

As will be discussed ahead, the simultaneous intersection between a spatial branch with F_k, and $\omega(k)$ with L_ω, is fundamental for this formulation of spatio-temporal theory, and also forms the basis of a clever geometrical method [15] for determining the spatio-temporal character of a base flow.

These approaches rely on the fact that if the line contour L_ω is lowered closer to $\omega(k)$ in the complex ω space, the spatial branches $k^+(\omega)$ and $k^-(\omega)$ also approach the line contour F_k in the complex k space. However, F_k can always be deformed such that it avoids intersecting the spatial branches and the integrals can still be evaluated without violating causality. Eventually a value of L_{w_i} is reached where the two spatial branches "pinch" the contour F_k such that it cannot be deformed any further to avoid the intersection and comply with causality. This point of intersection on F_k is therefore a double root of $D(\omega, k)$ denoted k^*, which along with its corresponding complex frequency ω^* forms the criteria used to determine the spatio-temporal nature of the base flow as explained in the following discussions.

3.4.3 Reverting the problem to physical space

The derivation proceeds by evaluating the integral (3.17) by closing L_ω from below and invoking the residue theorem to get

$$\psi(k,t) = -i\frac{S[k,\omega(k)]}{(\partial D/\partial\omega)[k,\omega(k)]}e^{-i\omega(k)t}. \tag{3.18}$$

Taking the inverse Fourier transform of (3.17) with resepct to k gives

$$\psi(x,t) = -\frac{i}{2\pi}\int_{F_k}\frac{S[k,\omega(k)]}{(\partial D/\partial\omega)[k,\omega(k)]}e^{i[kx-\omega(k)t]}dk. \tag{3.19}$$

This integral implies that the response of $\psi(x,t)$ to a source function $S(x,t)$ takes the form of a wave packet whose growth or decay is dictated the the temporal mode $\omega(k)$ such that

- If $\omega_i(k) < 0$ then the base flow is linearly *stable* and the integrand decays at a rate proportional to $\omega_i(k)$.
- If $\omega_i(k) > 0$ then the base flow is linearly *unstable* and the integrand grows at a rate proportional to $\omega_i(k)$.
- If $\omega_i(k) = 0$ then the base flow is linearly *neutrally stable* and a nonlinear analysis is required to determine its ultimate behavior.

The integral (3.19) is generally not solvable explicitly, but as mentioned in subsection 3.4.1, the flow's stability character can be determined by examining the long time response to an impulse source function $S(x,t) = \delta(x)\delta(t)$ along rays $\dfrac{x}{t} = constant$. For the impulse response problem, $\psi(x,t) \equiv G(x,t)$ and $S(k,\omega) = 1$ and therefore (3.19) becomes

$$G(x,t) = -\frac{i}{2\pi}\int_{F_k}\frac{1}{(\partial D/\partial\omega)[k,\omega(k)]}e^{i[kx-\omega(k)t]}dk. \tag{3.20}$$

This integral is part of a class of integrals in which integrand is dominated by an exponential term correlated with a large parameter, which makes it suitable for approximation by the method of steepest descent as explained ahead.

3.4.4 Approximate solution for G(x,t)

The next set of steps require lowering the line contour L_ω such that it intersects $\omega(k)$ at ω^* in the complex ω space, and consequently the line contour F_k has to be deformed away from the real k axis in order to to avoid intersecting the spatial branches and violating causality. This deformed line contour is denoted F_p and is "pinched" by the spatial branches $k^+(\omega)$ and $k^-(\omega)$ in the complex k space at a value denoted k^* for a general ray $\frac{x}{t} = constant$.
As mentioned previously, the order of magnitude of the integrand in (3.20) is governed at leading order by the real part of the exponent, which for $t \to \infty$ reads

$$\Re\Big\{i[kx - \omega(k)t]\Big\} = \Re\Big\{i[k\frac{x}{t} - \omega(k)]t\Big\}. \approx \omega_i(k)t \tag{3.21}$$

In other words, the long time value of the integral (3.20) along the ray $\frac{x}{t} = 0$ is governed by the height of the surface $\omega_i(k)$ in the (k_r, k_i, ω_i) space. The value of k^* associated with the ray $\frac{x}{t} = 0$ and its corresponding frequency $\omega_0 = \omega(k_0)$ are the basis for the criterion determing the flow's spatio-temporal character. These quantities are named the *absolute wavenumber* and *absolute frequency*, respectively. The following steps derive an asymptotic impulse response along the ray $\frac{x}{t} = 0$, which will then be generalized for any arbitrary ray $\frac{x}{t} = constant$ via a coordinate transformation.

To proceed, the geometric properties of the surface $\omega_i(k)$ around k_0 are exploited to approximate the integral along F_p; the fact that k_0 is a double root of $D(k, \omega)$ implies

$$D(k_0, \omega_0) = 0, \quad \text{and} \quad \frac{\partial D}{\partial k}(k_0, \omega_0) = 0, \tag{3.22}$$

Utilizing the derivative chain rule and assuming $\frac{\partial D}{\partial \omega}(k_0, \omega_0) \neq 0$ one obtains

$$\frac{\partial \omega}{\partial k}(k_0) = 0. \tag{3.23}$$

This means that k_0 is a stationary point of the function $\omega(k)$, and since $\omega(k_0)$ is the highest point along the $\omega(k)$ contour in the complex ω space, then it is also a global maximum of the function $\omega(k)$. This implies that $\omega_i(k_0)$ is also a global maximum in the surface (k_r, k_i, ω_i) along F_p. It can be further shown that $\omega_i(k_0)$

is in fact a saddle point [22] and therefore there are no other extrema points around k_0.

Based on the previous arguments, it is reasonable to expect the dominant contribution to the integral to arise from a small region $k_0 \pm \epsilon$ on F_p. Now the steepest descent method is applied and F_p is deformed to lie on the path of steepest descent through the complex k plane such that it avoids any extrema that can contribute significantly to the integral, and the surface $\omega_i(k)$ is approximated around k_0 by its Taylor expansion. Finally, the resultant expression reads as

$$G(x,t) \approx \frac{e^{i\left(\frac{\pi}{4}+k_0 x-\omega(k_0)t\right)}}{\frac{\partial D}{\partial \omega}[k_0,\omega(k_0)]\Big[2\pi\frac{\partial^2\omega}{\partial k^2}(k_0)t\Big]^{1/2}}. \tag{3.24}$$

Where $G(x,t)$ is the impulse response along the ray $\frac{x}{t} = 0$ i.e the laboratory frame. By examining the resultant expression in (3.24) it can be seen the impulse response takes the shape of a wavepacket with a temporal growth rate

$$\sigma_0 = \omega_{0,i}. \tag{3.25}$$

Based on (3.25), the Briggs-Bers criterion is stated as follows:

- The base flow state is *convectively* unstable if

$$\omega_{i,max} > 0 \quad \text{and} \quad \sigma_0 < 0, \qquad along \quad \frac{x}{t} = 0. \tag{3.26}$$

- The base flow state is *absolutely* unstable if

$$\omega_{i,max} > 0 \quad \text{and} \quad \sigma_0 > 0, \qquad along \quad \frac{x}{t} = 0. \tag{3.27}$$

These results can be generalized for an arbitrary spatio-temporal ray $\frac{x}{t} = V$ as $t \to \infty$ by making the transformation

$$x' = x - Vt, \tag{3.28a}$$

$$t' = t', \tag{3.28b}$$

$$k' = k, \tag{3.28c}$$

$$\omega' = \omega - kV. \tag{3.28d}$$

Under this transformation, (3.20) reads

$$G(x',t') = -\frac{i}{2\pi}\int_{F_k} \frac{1}{(\partial D'/\partial\omega')[k',\omega'(k')]} e^{i[k'x'-\omega(k')t']}dk', \tag{3.29}$$

where the integration contours are not changed, and the transformed dispersion relationship D' is related to the original by

$$D'(k',\omega') = D'(k',\omega'+k'V). \tag{3.30}$$

In terms of the original variables, pinching occurs at $k^* = k'_0$ and $\omega^* = w'_0 + k'_0 V$ such that

$$\omega^* = \omega(k^*) \quad \text{and} \quad \frac{\partial\omega}{\partial k}(k^*) = V. \tag{3.31}$$

Note that although $\partial\omega/\partial k$ is in general complex, it only represents a physical quantity when it is real, where it represents the group velocity of the wave packet traveling along the ray $\dfrac{x}{t} = V$.

By repeating the same procedure previously outlined, the asymptotic impulse response along an arbitrary ray $\dfrac{x}{t} = \textit{constant}$ for $t \to \infty$ reads

$$G(x,t) \approx \frac{e^{i\left(\pi/4 + k^* x - \omega(k^*)t\right)}}{\dfrac{\partial D}{\partial\omega}[k^*,\omega(k^*)]\left[2\pi\dfrac{\partial^2\omega}{\partial k^2}(k^*)t\right]^{1/2}}. \tag{3.32}$$

From this result it can be seen that the temporal growthrate perceived by an observer moving along the ray $\dfrac{x}{t}$ with a velocity V is

$$\sigma = \omega_i^* - k_i^* V \tag{3.33}$$

and therefore for an arbitrary spatio-temporal ray $\dfrac{x}{t} = \textit{constant}$

- If $\sigma > 0$ peturbations will grow in time along the ray $\dfrac{x}{t} = \textit{constant}$.
- If $\sigma < 0$ peturbations will decay in time along the ray $\dfrac{x}{t} = \textit{constant}$.

If a range of V values is plotted against their corresponding temporal growthrates in the (V,σ) plane, then the following observations can be made.

- The peak of the temporal growthrate curve σ_{max} corresponds to a wavenumber k_{max}, and represents the wave packet's highest amplitude. This point moves at the wave packet's group velocity denoted V_{max}. Note that this value σ_{max} corresponds to the maximum temporal growthrate $\omega_{i,max}$ obtainable using a purely temporal stability analysis.

- The points of two intersection between the temporal growthrate curve and the $\sigma = 0$ axis represent the velocities of the wave packet's leading and trailing edges in the (x, t) plane. This further clarifies the two distinct spatio-temporal behaviors. When both intersection points lie on the same side of the origin, both of wave packet's fronts are moving in the same direction and the wavepacket is advected away. However when the intersection points lie on opposite sides of the origin, the wavepacket's fronts are moving in opposite directions and therefore the instability will spread away from the origin in both directions until it contaminates the entire domain.

3.4.5 Geometric method for determining k_0 and ω_0

As discussed previously, the absolute/convective nature of the instability can be determined by finding the absolute wavenumber and frequency corresponding to the group velocity $\partial\omega/\partial k = x/t = 0$. However, this condition is not sufficient on its own since the saddle points considered in the impulse response must be formed by two spatial branches originating in opposite halves of the complex k plane in order for it to correspond to a double root of $D(k, \omega)$. Therefore only the saddle points satisfying both these conditions are sought, since the (ω_i, k_r, k_i) space could contain other saddle points which are formed by spatial branches originating on the same side of the F_k contour. These saddle points are not physically relevant and are therefore not included in the impulse response integral.

Bers devised a geometrical method [15] for identifying this particular type of saddle point which relies on starting with a contour L_ω high enough in the complex ω plane to be above all singularities of $D(k, \omega)$ and such that the spatial branches $k^+(\omega)$ and $k^-(\omega)$ lie on opposite sides of the contour F_k. Subsequently, L_ω is

lowered gradually while monitoring the development of the spatial branches in the complex k plane. It is assumed that the contour F_k is continuously deformed to avoid intersecting the spatial branches in order to not violate causality.

Eventually, a value of $L_{\omega,i}$ is reached such that the two spatial branches simultaneously pinch F_k at k_0 and therefore the value k_0 is suitably named the *pinching point*. Now the absolute wavenumber k_0 is identified as double root of $D(k,\omega)$ and the saddle point is of the type which contributes to the integral.

Notably, the saddle point is formed due to the combination of waves traveling in the positive and negative x directions. The corresponding image in the complex ω space is that of a cusp formed by the temporal mode $\omega(k)$ at its intersection point with L_ω. This intersection point is the absolute frequency $\omega_0 = \omega(k_0)$ such that the temporal growthrate at the origin is $\omega_{0,i}$ whereby if $\omega_{0,i} < 0$ (resp $\omega_{0,i} > 0$) an unstable state is convectively (resp. absolutely) unstable. Lowering L_ω any further violates causality. Additionally, as emphasized in [15], the first pinching point encountered is sufficient to determine the spatio-temporal character of the flow.

Chapter 4

Long wave theory

4.1 Derivation of the interface evolution equation

4.1.1 Rescaling

In a procedure inspired by Benney's [23] expansion for small wavenumbers, we perform the following steps:

1. Define a small parameter $\epsilon = \dfrac{\bar{h}}{\ell}$, where ℓ is the flow's horizontal characteristic length such that $\ell \gg \bar{h}$.

2. Rescale the system's independent variables as:

$$x \to \epsilon x, \tag{4.1a}$$

$$y \to y, \tag{4.1b}$$

$$t \to \epsilon t. \tag{4.1c}$$

3. Expand the system's dependent variables in terms of ϵ as:

$$u = u_0 + \epsilon u_1 + O(\epsilon^2), \tag{4.2a}$$

$$v = \epsilon(v_0 + \epsilon v_1 + O(\epsilon^2)), \tag{4.2b}$$

$$p = p_0 + \epsilon p_1 + O(\epsilon^2), \tag{4.2c}$$

$$T = T_0 + \epsilon T_1 + O(\epsilon^2), \tag{4.2d}$$

$$J = J_0 + \epsilon J_1 + O(\epsilon^2). \tag{4.2e}$$

4. Scale the following dimensionless parameters as:

$$E \to \epsilon \bar{E}, \tag{4.3a}$$

$$D \to \epsilon^2 \bar{D}, \tag{4.3b}$$

$$S \to \frac{\bar{S}}{\epsilon^2}. \tag{4.3c}$$

5. We consider the shear agent quantity τ and the interface height function $h(t)$ to be zero order quantities.

Substituting these scales into the system of equations (2.6) we obtain 2 sets of equations at first and zero order, which can be solved to obtain the base state solutions for the problem's dependent variables up to $O(\epsilon)$.

4.1.2 Zero order system

By collecting the zero order terms in equation (2.6) we obtain the following system of equations:

- Continuity equation: No terms appear at zero order.

- Navier-Stokes equation

$$\partial_{yy} u_0 + Re sin\beta = 0, \tag{4.4a}$$

$$-\partial_y p_0 - Re cos\beta = 0, \tag{4.4b}$$

- Energy equation

$$\partial_{yy} T_0 = 0, \tag{4.4c}$$

- Wall boundary conditions at $y = 0$
  - $u_0 = v_0 = 0,$ (4.4d)
  - $T_0 = 1,$ (4.4e)

- Interface boundary conditions $y = h(t)$
  - Kinematic boundary condition: No terms appear at zero order.
  - Energy balance

$$J_0 = -\partial_y T_0, \tag{4.4f}$$

  - Normal stress balance

$$p_0 = \frac{3}{2}\frac{E^2}{D} J_0^2 - 3\bar{S}\partial_{xx} h, \tag{4.4g}$$

  - Shear stress balance

$$\partial_y u_0 = \tau, \tag{4.4h}$$

  - Constitutive relationship

$$K J_0 = T_0. \tag{4.4i}$$

Solving the zero order system we obtain the solutions for the dependent variables at zero order.

$$u_0(y) = Re sin\beta \left(hy - \frac{1}{2} y^2 \right) + \tau y, \tag{4.5a}$$

$$p_0(y) = Re cos\beta (h - y) + \frac{3}{2}\frac{E^2}{D}\frac{1}{(h+K)^2} - 2\bar{S}\partial_{xx} h, \tag{4.5b}$$

$$T_0(y) = 1 - \frac{1}{h+K} y, \tag{4.5c}$$

$$J_0 = \frac{1}{(h+K)}. \tag{4.5d}$$

Note that v_0 does not appear in the solution to the zero-order system since it is a quantity of O(ϵ). Additionally, as mentioned in subsection (2.2.2), τ appears as an algebraic modifier to the base state velocity.

4.1.3 First order system

By collecting the terms of $O(\epsilon)$ in (2.6) we obtain the following system:

- Continuity equation

$$\partial_x u_0 = -\partial_y v_0, \tag{4.6a}$$

- Navier-Stokes equation

$$\partial_t u_0 + u_0 \partial_x u_0 + v_0 \partial_y u_0 = -\partial_x p_0 + \partial_{yy} u_1, \tag{4.6b}$$

$$-\partial_y p_1 + \partial_{yy} v_0 = 0, \tag{4.6c}$$

- Energy equation

$$P(\partial_t T_0 + u_0 \partial_x T_0 + v_0 \partial_y T_0) = \partial_{yy} T_1, \tag{4.6d}$$

- Wall boundary conditions at $y = 0$

  - $u_1 = v_1 = 0,$ (4.6e)
  - $T_1 = 0,$ (4.6f)

- Interface boundary conditions at $y = h(t)$

  - Mass balance

$$v_0 - \partial_t h - u_0 \partial_x h = \bar{E} J_0, \tag{4.6g}$$

  - Energy balance

$$J_1 = -\partial_y T_1, \tag{4.6h}$$

  - Normal stress

$$p_1 = 3\frac{E^2}{D} J_0 J_1 - 2\partial_x u_0 + \partial_x h \partial_y u_0, \tag{4.6i}$$

▫t Shear stress

$$\partial_y u_1 + 2\left(\frac{M}{P}\right)\left[\partial_x T_0 + \partial_x h \partial_y T_0\right] = 0, \tag{4.6j}$$

▫ Constitutive relationship

$$KJ_1 = T_1. \tag{4.6k}$$

Solving the first order system and combining with the zero order solutions we obtain the expressions for the dependent variables up to $O(\epsilon)$:

• Streamwise velocity $u(x, y, t)$

$$\begin{aligned} u(x,y,t) =& Resin\beta(hy - \frac{y^2}{2} + \tau y) \\ &+ \epsilon\Bigg[(Recos\beta\partial_x h - \phi)(\frac{y^2}{2} - yh) + \frac{2M}{P}\partial_x\left(\frac{h}{h+K}\right)y \\ &+ Resin\beta\partial_t h\frac{y^3}{6} - Resin\beta\ \partial_t h\frac{h^2}{2}y + \partial_x h(Resin\beta)^2\frac{y^4}{24} \\ &+ \partial_x h Resin\beta\frac{y^4}{24}\tau - \frac{1}{6}\partial_x h(Resin\beta)^2 h^4 y - \frac{1}{6}\partial_x h Gsin\beta h^3\tau y\Bigg] + O(\epsilon^2), \end{aligned} \tag{4.7a}$$

where $\phi = 3\frac{E^2}{D}\frac{1}{(h+K)^3}\partial_x h + 3\bar{S}\partial_{xxx}h$.

• Cross-stream velocity at the interface $v(x, h, t)$

$$\begin{aligned} v(x,h,t) =& \epsilon\Bigg[-\frac{1}{2}Resin\beta\partial_x h y^2\Bigg] \\ &+ \epsilon^2\Bigg[Recos\beta\frac{h^3}{3}\partial_{xx}h + Recos\beta\frac{h^2}{2}(\partial_x h)^2 - \partial_x\phi\frac{h^3}{3} - \phi\frac{h^2}{2}\partial_x h \\ &+ \frac{5}{24}Resin\beta\partial_{tx}h + Resin\beta\frac{h^3}{2}\partial_t h\partial_x h + \frac{13}{40}(Resin\beta)^2(\partial_x h)^2 h^5 \\ &+ \frac{3}{40}(Resin\beta)^2 h^6\partial_{xx}h + \frac{1}{4}Resin\beta h^4(\partial_{xx}h)^2\tau - \frac{M}{P}\partial_{xx}\left(\frac{h}{h+K}h^2\right) \\ &+ \frac{3}{40}Resin\beta h^5\partial_{xx}h\tau\Bigg] \quad + O(\epsilon^3). \end{aligned} \tag{4.7b}$$

- Temperature $T(x,y,t)$

$$\begin{aligned} T(y,t) =& 1-\frac{1}{(h+K)}y \\ & \epsilon\Bigg[P\Big\{\frac{\partial_t h}{(h+K)^2}\big(\frac{y^3}{6}-\frac{h^2}{2}y\big)+Resin\beta\frac{h\partial_x h}{(h+K)^2}\big(\frac{y^4}{12}-\frac{h^3}{3}y\big) \\ & +\frac{\partial_x h}{(h+K)^2}\big(\frac{y^4}{12}+\frac{h^3}{3}y\big)\tau-Resin\beta\frac{\partial_x h}{(h+K)^2}\big(\frac{y^5}{40}-\frac{h^4}{8}y\big) \\ & +Resin\beta\frac{\partial_x h}{(h+K)}\big(\frac{y^4}{24}-\frac{h^3}{6}y\big)-J_1 y\Big\}\Bigg]+O(\epsilon^2). \end{aligned} \tag{4.7c}$$

- Heat flux $J(x,t)$

$$\begin{aligned} J(x,t) =& \frac{1}{(h+K)}+\epsilon\Bigg[-\frac{h^3}{(h+K)^3}P\Big\{\frac{\partial_t h}{3} \\ & +Resin\beta h\partial_x h\big(\frac{11}{40}h+\frac{K}{8}\big)+\frac{1}{4}h\partial_x h\tau\Big\}\Bigg]+O(\epsilon^2). \end{aligned} \tag{4.7d}$$

4.1.4 The Benney-like equation

The scales (4.1), (4.2), and (4.3) are substituted into the liquid-gas interface's kinematic boundary condition equation (2.6g). Collecting terms of similar order together, the following expression is obtained:

$$\partial_t h+u_0\partial_x h+\bar{E}J_0-v_0+\epsilon\Big[\bar{E}J_1+u_1\partial_x h-v_1\Big]=0. \tag{4.8}$$

Substituting the flow variables' solutions from equation (4.7) into equation (4.8), we obtain a Benney-like equation for the interface's temporal evolution. Note that the following new dimensionless parameters are now defined

- Vapor recoil parameter: $V_r=\bar{E}^2/D$, which represents the strength of the vapor recoil forces on the liquid interface.

- Modified Marangoni number: $KM/P = \bar{M}$, which represents mainly the strength of the thermocapillary forces along on the liquid interface.

$$
\begin{aligned}
&\partial_t h + Resin\beta h^2 \partial_x h + \frac{\bar{E}}{h+K} + h\partial_x h\tau \\
&+\epsilon\Bigg[\frac{2}{15}(Resin\beta)^2\left(h^6\partial_{xx}h + 6h^5(\partial_x h)^2\right) \\
&\quad + \bar{M}\left(\frac{h^2}{(h+K)^2}\partial_{xx}h + 2\frac{h^2}{(h+K)^2}(\partial_x h)^2 - 2\frac{h^2}{(h+K)^3}(\partial_x h^2)\right) \\
&\quad + V_r\left(\frac{h^3}{(h+K)^3}\partial_{xx}h + 3\frac{h^2}{(h+K)^3}(\partial_x h)^2 - 3\frac{h^3}{(h+K)^4}(\partial_x h)^2\right) \\
&\quad - \frac{1}{3}Recos\beta\Big(h^3\partial_{xx}h + 3h^2(\partial_x h)^2\Big) + \bar{S}\Big(3h^2\partial_x h\partial_{xxx}h + h^3\partial_{xxxx}h\Big) \\
&\quad + \frac{5}{24}\bar{E}Resin\beta\left(4\frac{h^3}{(h+K)}\partial_x h - \frac{h^4}{(h+K)^2}\partial_x h\right) \\
&\quad + \bar{E}P\frac{h^3}{(h+K)^3}\left(\frac{\bar{E}}{3}\frac{1}{(h+K)} + \frac{1}{120}Resin\beta(7h-15K)h\partial_x h\right) \\
&\quad + \tau\left(\frac{1}{12}\bar{E}P\frac{h^4}{(h+K)^3} + \frac{2}{3}Resin\beta h^4(\partial_x h)^2 + \frac{2}{15}Resin\beta h^5\partial_{xx}h\right)\Bigg] + O(\epsilon^2).
\end{aligned}
\tag{4.9}
$$

Equation (4.9) describes the interface's temporal evolution under the effects of gravity, hydrostatic pressure, thermocapillarity, evaporation, and gas shear. It is identical to equation (3.13) in [24] except for the additional terms proportional to τ.

4.2 Dispersion relationship derivation

4.2.1 Base flow state

Equation (4.9) is a general equation for the interface height function $h(t)$ which can admit a range of base flows. The base flow state to be analyzed is one that is spatially uniform but temporally dynamic and whose governing equation can

be found by setting $\partial_x = 0$ in equation (4.9) to get:

$$\partial_t \bar{h} + \frac{\bar{E}}{\bar{h} + K} + \epsilon \bar{E}^2 \frac{P \bar{h}^3}{3(\bar{h} + K)^4} = 0. \tag{4.10}$$

Solving equation (4.10) we get:

$$\bar{h}(t) = \Omega - K + \epsilon \frac{\bar{E} P}{3\Omega} \Big(\frac{K(2K^2 + 6K + 3)}{1 + K} + \frac{3K^2}{2} ln \frac{\Omega}{1 + K} + \frac{K^3}{\Omega} - 3K\Omega - \bar{E}t \Big) + O(\epsilon^2), \tag{4.11}$$

where $\Omega = (K^2 + 2K + 1 - 2\bar{E}t)^{1/2}$.

The amount of time it takes a liquid film governed by a particular parameter set to completely evaporate is called *dry-out time*, denoted t_D. An analytical expression for t_D can be found by setting $\bar{h}(t) = 0$ and solving for t in equation (4.11):

$$t_D = \frac{1 + 2K}{2\bar{E}}. \tag{4.12}$$

Fractions of the quantity t_D are used in the stability analysis to represent how much remains of the evaporating liquid film at the point in time at which stability is investigated. This fraction of t_D is denoted t_f.

4.2.2 Introducing the perturbations

We assume that the interface height function $h(t)$ is perturbed by an infinitesimal harmonic perturbation such that:

$$h(t) = \bar{h}(t) + \xi H e^{i(kx - \omega t)}, \quad \text{where } \xi \ll 1. \tag{4.13}$$

Initially equation (4.10) is subtracted from equation (4.9) in order to get rid of the base state terms since they do not contribute to the instability, afterwhich

equation (4.13) is substituted into equation (4.9) to get the following expression:

$$\begin{aligned}\omega(k) = &-i\epsilon\bar{S}\bar{h}^3k^4 + i\epsilon\Big[\frac{2}{15}(Resin\beta)^2\bar{h}^6 \\ &+ V_r\frac{\bar{h}^3}{(\bar{h}+K)^3} + \bar{M}\frac{\bar{h}^2}{(\bar{h}+K)^2} - \frac{1}{3}Recos\beta\bar{h}^3 + \frac{2}{15}Resin\beta\bar{h}^5\tau\Big]k^2 \\ &+ \Bigg[Resin\beta\bar{h}^2 + \bar{h}\tau + \epsilon\Big(\frac{5}{6}Resin\beta\bar{E}\frac{\bar{h}^3}{\bar{h}+K} + \frac{7}{120}\bar{E}Resin\beta P\frac{\bar{h}^5}{(\bar{h}+K)^3} \\ &- \frac{5}{24}Resin\beta\bar{E}\frac{\bar{h}^4}{(\bar{h}+K)^2} - \frac{1}{8}Resin\beta\bar{E}P\frac{\bar{h}^4}{(\bar{h}+K)^3}K + \frac{1}{12}\bar{E}P\frac{\bar{h}^4}{(\bar{h}+K)^3}\tau\Big)\Bigg]k \\ &+ i\frac{\bar{E}}{(\bar{h}+K)^2} - i\epsilon P\bar{E}^2\frac{\bar{h}^2(3K-\bar{h})}{3(\bar{h}+K)^5}.\end{aligned} \tag{4.14}$$

Note that the last two terms in equation (4.14) are not proportional to any power of k, but rather are an algebraic addition to the imaginary part of ω, as a function of base state height $\bar{h}$. This quantity is larger than zero for the range of parameters considered in this work, and therefore causes an increase in the perturbation's growthrate not related to the flow's stability, but instead to the reduction in base state height due to mass loss. This increment to the growthrate caused by the decrease in $\bar{h}$ with time can cause an otherwise stable flow ($\omega_i < 0$) to be characterized as unstable because of ω_i being incremented to a positive value. Therefore these terms will be omitted, and the dispersion relationship now becomes:

$$\begin{aligned}\omega(k) = &-i\epsilon\bar{S}\bar{h}^3k^4 + i\epsilon\Big[\frac{2}{15}(Resin\beta)^2\bar{h}^6 \\ &+ V_r\frac{\bar{h}^3}{(\bar{h}+K)^3} + \bar{M}\frac{\bar{h}^2}{(\bar{h}+K)^2} - \frac{1}{3}Recos\beta\bar{h}^3 + \frac{2}{15}Resin\beta\bar{h}^5\tau\Big]k^2 \\ &+ \Bigg[Resin\beta\bar{h}^2 + \bar{h}\tau + \epsilon\Big(\frac{5}{6}Resin\beta\bar{E}\frac{\bar{h}^3}{\bar{h}+K} + \frac{7}{120}\bar{E}Resin\beta P\frac{\bar{h}^5}{(\bar{h}+K)^3} \\ &- \frac{5}{24}Resin\beta\bar{E}\frac{\bar{h}^4}{(\bar{h}+K)^2} - \frac{1}{8}Resin\beta\bar{E}P\frac{\bar{h}^4}{(\bar{h}+K)^3}K + \frac{1}{12}\bar{E}P\frac{\bar{h}^4}{(\bar{h}+K)^3}\tau\Big)\Bigg]k.\end{aligned} \tag{4.15}$$

In the following discussions, the temporal and spatio-temporal stability of equation (4.9) is analyzed using the dispersion relationship (4.15) which for conciseness

will be written as

$$\omega(k) = Ak^4 + Ck^2 + Dk. \tag{4.16}$$

4.3 Temporal stability analysis

As discussed in section 3.2, for the purposes of temporal stability analysis it is assumed that the wavenumber k is real and the frequency ω is complex. Under these assumptions, equation (4.15) can be written as

$$\omega(k) = \omega_r + i\omega_i. \tag{4.17}$$

where $\omega_r = kc$ is the the real angular frequency

$$\omega_r = k\Big[Resin\beta\bar{h}^2 + \bar{h}\tau + \epsilon\Big(\frac{5}{6}Resin\beta\bar{E}\frac{\bar{h}^3}{\bar{h}+K} + \frac{7}{120}\bar{E}Resin\beta P\frac{\bar{h}^5}{(\bar{h}+K)^3} - \frac{5}{24}Resin\beta\bar{E}\frac{\bar{h}^4}{(\bar{h}+K)^2} - \frac{1}{8}Resin\beta\bar{E}P\frac{\bar{h}^4}{(\bar{h}+K)^3}K + \frac{1}{12}\bar{E}P\frac{\bar{h}^4}{(\bar{h}+K)^3}\tau\Big)\Big], \tag{4.18a}$$

and ω_i is the temporal growthrate

$$\omega_i = \epsilon\Big[\frac{2}{15}Resin\beta\bar{h}^6\big(Resin\beta + \frac{\tau}{\bar{h}}\big) + \bar{M}\frac{\bar{h}^2}{(\bar{h}+K)^2} + V_r\frac{\bar{h}^3}{(\bar{h}+K)^3} - \frac{1}{3}Recos\beta\bar{h}^3 - \bar{S}\bar{h}^3k^2\Big]k^2. \tag{4.18b}$$

The first 3 terms in equation (4.18b) contribute positively to the instability's temporal growth rate and are therefore destabilizing. These terms represent in order: inertia due to gravitational acceleration as modified by the shear agent $\boldsymbol{\tau}$, thermocapillary forces, and vapor recoil. On the other hand, the last 2 terms are stabilizing since they are negative, and they represent the effects of hydrostatic pressure and surface tension, respectively.

It can be seen from this expression the shear agent τ acts strictly as a modifier to *existing* instability modes by adjusting the inertial contribution arising from gravitational acceleration. Consequently, non-inertial contributions to the

temporal growthrate i.e those due to thermocapillarity and vapor recoil are independent of τ. As for the effect of the shear agent on the perturbation phase speed, equation (4.18a) indicates that it is not strictly tied to the base flow's inertia.

Generally speaking, the role of τ can be summarized as

- A positive (resp. negative) value of τ increases (resp. decreases) the width of the band of wavenumbers for which the base flow is unstable thereby increasing (resp. decreasing) the cutoff wavenumber k_c. This only applies when the base state is flowing i.e $Re \neq 0$.
- A positive (resp. negative) value of τ increases (resp. decreases) the temporal growth rate ω_i at all unstable wavenumbers. This only applies when the base state is flowing i.e $Re \neq 0$.
- A positive (resp. negative) value of τ increases (resp. decreases) the perturbation phase speed, whereby this is not strictly tied to the base flow's inertia.

This general behavior has several significant implications. Namely, for a negative enough value of τ the contribution from gravitational acceleration can be negated completely. Practically this means that the inertial instability mode (H-mode) can be completely stabilized by a strong enough counter-flowing shearing gas as shown in figure 4.1. However, since the contributions of thermal instability sources are not diminished by $\tau < 0$, this suggests the possibility of the existence thermal perturbation with a negative phase speed being advected up stream by a counter-flowing shearing gas.

The results of the temporal stability study are now presented. Note that throughout this investigation, the following parameter values are fixed

$$\epsilon = 0.1, \quad \bar{S} = 0.1, \quad K = 0.1, \quad P = 1.$$

4.3.1 The effects of τ on an isothermal base flow

An isothermal base flow's temporal stability is governed by

$$\omega_r = k\Big[Resin\beta\bar{h}^2 + \bar{h}\tau\Big], \text{ and} \tag{4.19a}$$

$$\omega_i = \epsilon\Big[\frac{2}{15}Resin\beta\bar{h}^6\big(Resin\beta + \frac{\tau}{\bar{h}}\big) - \frac{1}{3}Recos\beta\bar{h}^3 - \bar{S}\bar{h}^3k^2\Big]k^2. \tag{4.19b}$$

For an isothermal base flow, The shear agent τ affects the value of the cut-off wavenumber k_c and the temporal growth rates across the range of unstable wavenumbers depending on its sign. Consequently the critical Reynolds number i.e the value of Re where the ω_i first becomes positive is shifted by an amount proportional to the value of τ.

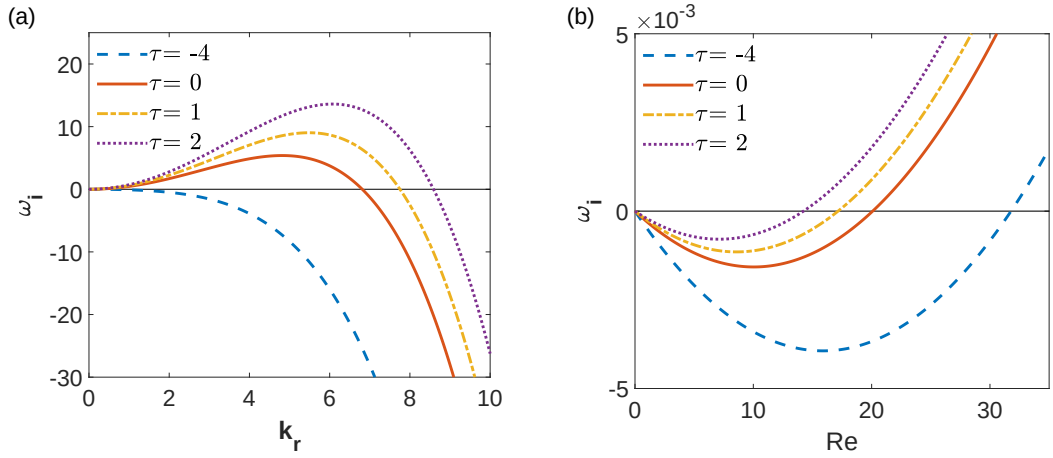

Figure 4.1: The effects of the shear agent τ on the temporal growth rate of a perturbation in an isothermal base flow for $\beta = 20$, $\bar{M}$=0, $\bar{E} = 0$, $V_r = 0$. (a) Temporal growth rate vs wavenumber at $Re = 30$. (b) Temporal growth rate vs Reynolds number at $k = 0.1$.

Figures 4.1(a) and 4.1(b) show the presence of a single instability mode (the H-mode) and its expansion (resp. shrinkage) with larger (resp. smaller) values of τ. Note in part (b) how the H-mode instability has been completely suppressed in the case of $\tau = -4$, rendering the film completely stable for the given parameter set.

4.3.2 The effects of τ on the Marangoni instability of a nonvolatile base flow

A nonvolatile base flow subject to thermocapillary effects exhibits two possible modes of instability. The first is the S-mode which appears when the liquid film is stationary or flowing with relatively small Reynolds numbers, while the second is the H-mode which appears at higher Reynolds numbers, albeit modified by the thermocapillary effects. The effects of τ on both of these modes is studied.

The temporal stability of this base flow is governed by

$$\omega_r = k\Big[Re sin\beta\bar{h}^2 + \bar{h}\tau\Big], \text{ and} \tag{4.20a}$$

$$\omega_i = \epsilon\Big[\frac{2}{15}Re sin\beta\bar{h}^6\big(Re sin\beta + \frac{\tau}{\bar{h}}\big) + \bar{M}\frac{\bar{h}^2}{(\bar{h}+K)^2} - \frac{1}{3}Re cos\beta\bar{h}^3 - \bar{S}\bar{h}^3k^2\Big]k^2. \tag{4.20b}$$

- **Stationary base flow ($\boldsymbol{\beta = 0}$)**

By setting $\beta = 0$, all inertial contributions vanish and equations (4.20) now show that in the case of a stationary nonvolatile base state, the perturbation phase speed is a linear function of τ exclusively. When this base state is subject to thermocapillary forces, its stability is determined by the competition between the destabilizing effects of thermocapillarity and the stabilizing forces of hydrostatic pressure and surface tension. The shear agent does not influence the temporal growth rate since its effect is tied to inertial instabilities, which in this case are absent. The plots in figure 4.2 show the variation in ω_i with $\bar{M}$, where as expected higher values of $\bar{M}$ lead to a stronger S-mode instability as represented by the higher temporal growth rates and the wider band of unstable wave numbers.

Figure 4.2(b) shows the existence of a single region of positive temporal growth rate above the Re axis representing the S-mode instability. As for the phase speed c, then its linear variation with τ is seen in figure 4.2(c). Note how the phase speed becomes negative for $\tau < 0$ indicating the fact that the perturbation is

traveling upstream for this particular parameter set.

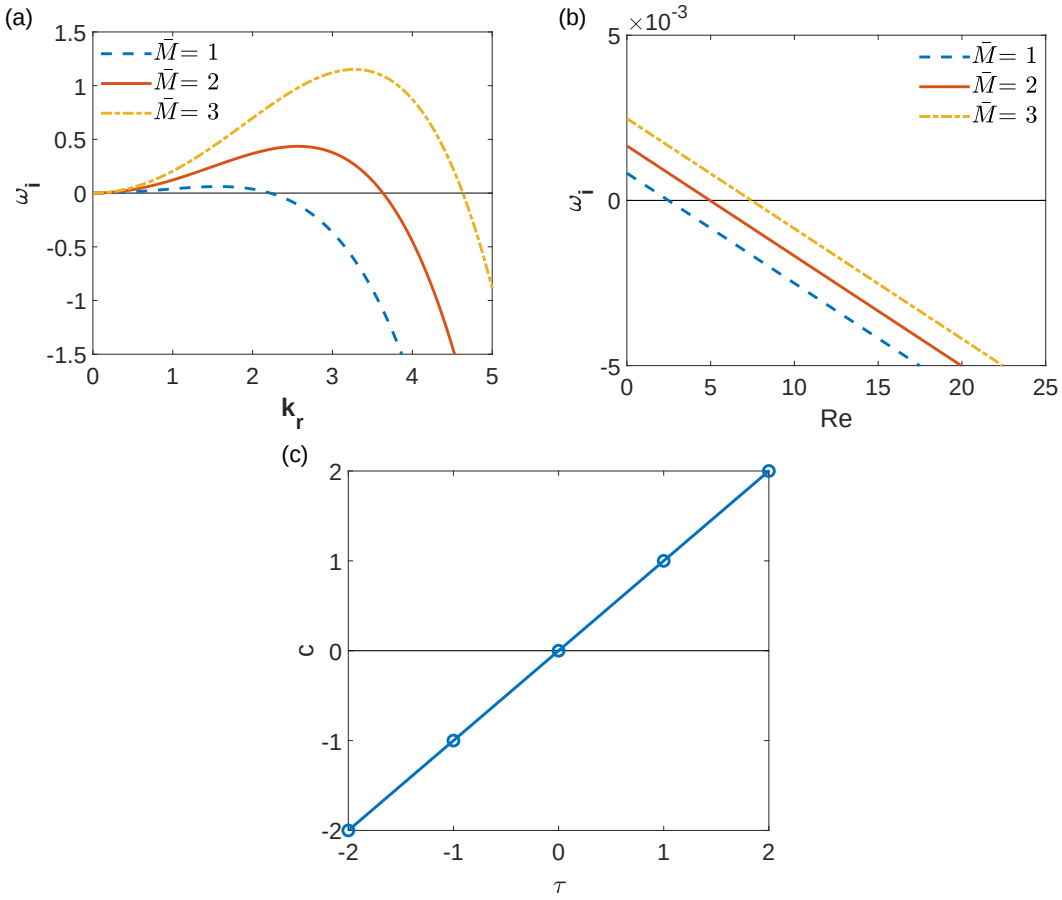

Figure 4.2: The effects of the modified Marangoni number $\bar{M}$ on a perturbation in a nonvolatile stationary base flow subject to the Marangoni instability for $\beta = 0$, $\bar{E} = 0$, $V_r = 0$. (a) Temporal growth rate vs wavenumber at $Re = 1$. (b) Temporal growth rate vs Reynolds number at $k = 0.1$. (c) Phase speed vs shear agent at $Re = 1$.

- **Moving base flow ($\beta > 0$)**

In the case of a moving base flow, the stabilizing forces now have to compete against inertia as modified by the shear agent, in addition to thermocapillary effects. Consequently, both the H and S instability modes appear at their respective parameter domains.

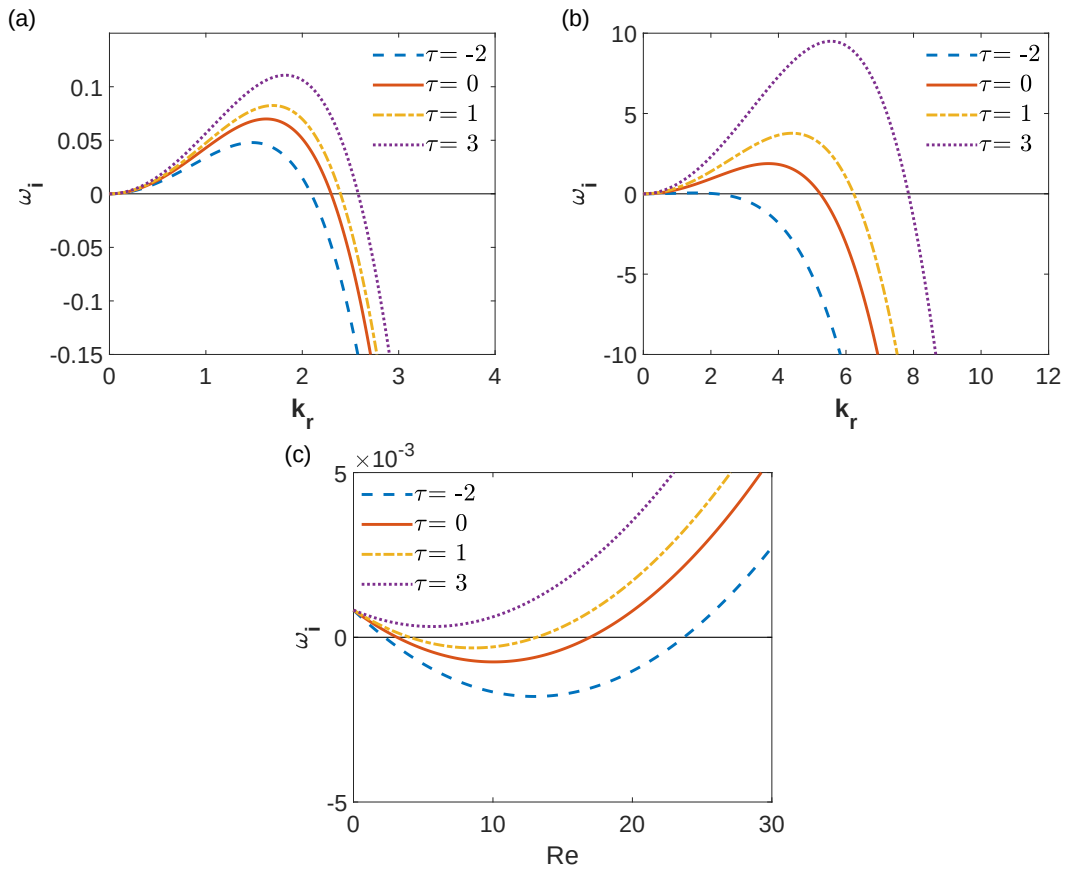

Figure 4.3: The effects of the shear agent τ on the temporal growth rate of a perturbation in a nonvolatile moving base flow subject to the Marangoni instability for $\beta = 20$, $\bar{M}$=0, $\bar{E} = 0$, $V_r = 0$. (a) Temporal growth rate vs wavenumber at $Re = 1$. (b) Temporal growth rate vs wavenumber at $Re = 25$. (c) Temporal growth rate vs Reynolds number at $k = 0.1$.

The two modes of instability can be seen in figure 4.3 as there are now two regions of positive growth rate in the (Re, ω_i) plane. Notice how for $\tau = 3$ the two unstable regions are unified into a single unstable region and the base flow is temporally unstable at all values of Reynolds number. Additionally, a comparison between figure 4.3(a) and figure 4.3(b) reveals that the H-mode is affected to a much larger degree by τ than the S-mode since it is dominated by inertial effects, which τ contributes strongly to.

4.3.3 The effects of τ on the evaporation instability of a volatile base flow

In order to better understand the dynamics of an evaporating liquid film, the evaporation instability is isolated from the Marangoni one by setting $\bar{M} = 0$. Consquently, the temporal stability of an evaporating base flow is governed by

$$\omega_r = k\Big[Resin\beta\bar{h}^2 + \bar{h}\tau + \epsilon\Big(\frac{5}{6}Resin\beta\bar{E}\frac{\bar{h}^3}{\bar{h}+K} + \frac{7}{20}\bar{E}Resin\beta P\frac{\bar{h}^5}{(\bar{h}+K)^3} - \frac{5}{24}Resin\beta\bar{E}\frac{\bar{h}^4}{(\bar{h}+K)^2} - \frac{1}{8}Resin\beta\bar{E}P\frac{\bar{h}^4}{(\bar{h}+K)^3}K + \frac{1}{12}\bar{E}P\frac{\bar{h}^4}{(\bar{h}+K)^3}\tau\Big)\Big], \tag{4.21a}$$

and

$$\omega_i = \epsilon\Big[\frac{2}{15}Resin\beta\bar{h}^6\big(Resin\beta + \frac{\tau}{\bar{h}}\big) + V_r\frac{\bar{h}^3}{(\bar{h}+K)^2} - \frac{1}{3}Recos\beta\bar{h}^3 - \bar{S}\bar{h}^3k^2\Big]k^2. \tag{4.21b}$$

- **Stationary base flow ($\boldsymbol{\beta = 0}$)**

In a stationary volatile base flow, the perturbation phase speed is a function of τ and evaporation effects, since the first term in equation (4.21a) vanishes for $\beta = 0$. As for the temporal growthrate, again the shear agent's effect vanishes due to the base state having no inertia, and what remains is a competition between vapor recoil and the stabilizing effects of hydrostatic pressure and surface tension.

Note how the rate of mass loss represented by the evaporation number $\bar{E}$ does not appear in the temporal growth rate directly. However it does play an indirect role by determining the base state height at a certain point in time as seen in equation (4.10). The evaporation number's effect comes into play after a finite amount of time has passed since it determines the rate at which the film thickness reduces from its initial value of unity. This reduction in base flow height affects the E and H instability modes differently.

The E-mode instability becomes stronger in a thinner film as it can be seen

from equation (4.21b) that the contribution from vapor recoil is $O(\bar{h})$, while the stabilizing contributions of hydrostatic pressure and surface tension are $O(\bar{h}^3)$. On the other hand, the H-mode instability is actually diminished as the film thins due to the increasing dominance of viscosity.

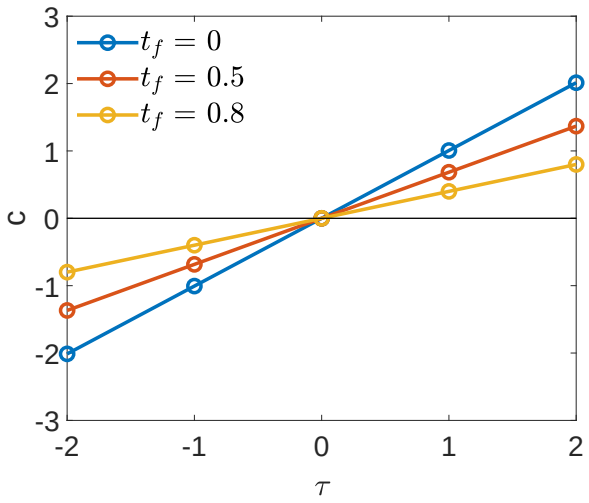

Figure 4.4: The effects of the shear agent and film thickness on the perturbation phase speed in a stationary volatile base flow subject to the evaporation instability for $\beta = 0$, $Re = 1$, $\bar{M}$=0, $\bar{E} = 0.1$, $V_r = 1$.

Contrary to the temporal growth rate, the phase speed of the perturbation for this type of base flow does depend on the shear agent quantity. Figure 4.4 shows the effect of film thickness on the advection of the perturbation in the flow domain under the effect of the shear agent. The figure indicates that resistance to advection of perturbations increases as the film thins.

The change in the E-mode instability as the vapor recoil parameter V_r increases is shown in figure 4.5. It demonstrates the existence of a single unstable domain at relatively low Reynolds numbers which grows with larger values of V_r. By comparing figures 4.5(a) and 4.5(b) with 4.5(c) and 4.5(d) it is obvious that the E-mode instability becomes significantly stronger as the film thickness reduces due to evaporation.

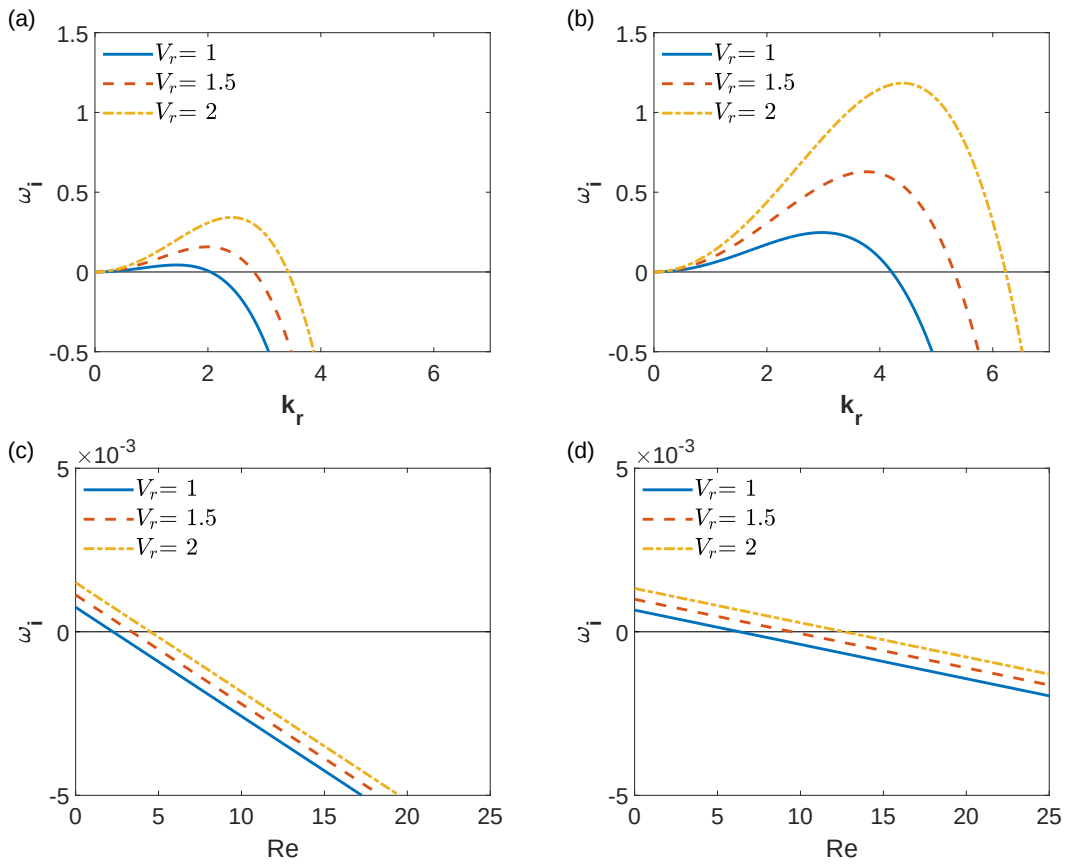

Figure 4.5: The effects of the vapor recoil and film thickness on the temporal growth rate of a perturbation in a volatile stationary base flow subject to the evaporation instability for $\beta = 0$, $\bar{M}$=0, $\bar{E} = 0.1$. (a) Temporal growth rate vs wavenumber at $Re = 1$ and $t_f = 0$. (b) Temporal growth rate vs wavenumber at $Re = 1$ and $t_f = 0.5$. (c) Temporal growth rate vs Reynolds number at $k = 0.1$ and $t_f = 0$. (d) Temporal growth rate vs Reynolds number at $k = 0.1$ and $t_f = 0.5$.

- **Moving base flow ($\beta > 0$)**

In an analogue to a moving base state subject to the thermocapillary instability, an evaporating moving base state diplays two modes of instability; the E-mode at small values of Re due to vapor recoil and the inertial H-mode at relatively larger Re values. Figure 4.7 demonstrates the effect of τ on the temporal

growth rates of this base flow, where this effect differs significantly depending on the flow domain and parameter set. In general both instability modes grow (resp. decay) with positive (resp. negative) values of τ. As for the effect of film thickness, the E-mode becomes stronger in a thinner film due to the weaker hydrostatic pressure, and this is accompanied by diminishing effects of τ as seen in figure 4.7(b). This is due to the fact that viscous effects which directly compete with the shear stress at the interface [25], become stronger as the film thins. Figure 4.6 further confirms these observations. Notice in figure 4.6(b) the plot corresponding to $\tau = 5$ where the E and H modes became separated by a stability window which appeared at the lower film thickness.

As for the H-mode, not only is the change in the instability with τ reduced at the lower film height, but also the instability itself is significantly suppressed. Part (d) shows the H-mode instability completely vanishing even for $\tau = 5$. Again this is due to viscous effects becoming increasingly dominant at reduced film height, and since the H-mode is an inertial instability, it is contested strongly by the viscosity which dominates the thinner films.

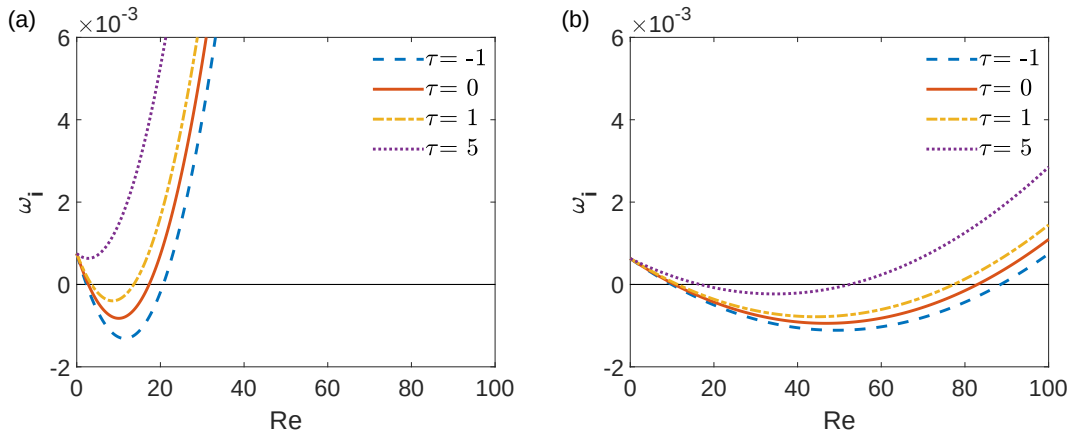

Figure 4.6: The effects of reduction in film height on the temporal growth rate of a perturbation in a moving volatile base flow for $\beta = 20$, $\bar{M}$=0, $\bar{E} = 0.1$, $V_r = 1$. (a) Temporal growth rate vs Reynolds number for $k = 0.1$ and $t_f = 0$. (b) Temporal growth rate vs Reynolds number for $k = 0.1$ and $t_f = 0.6$.

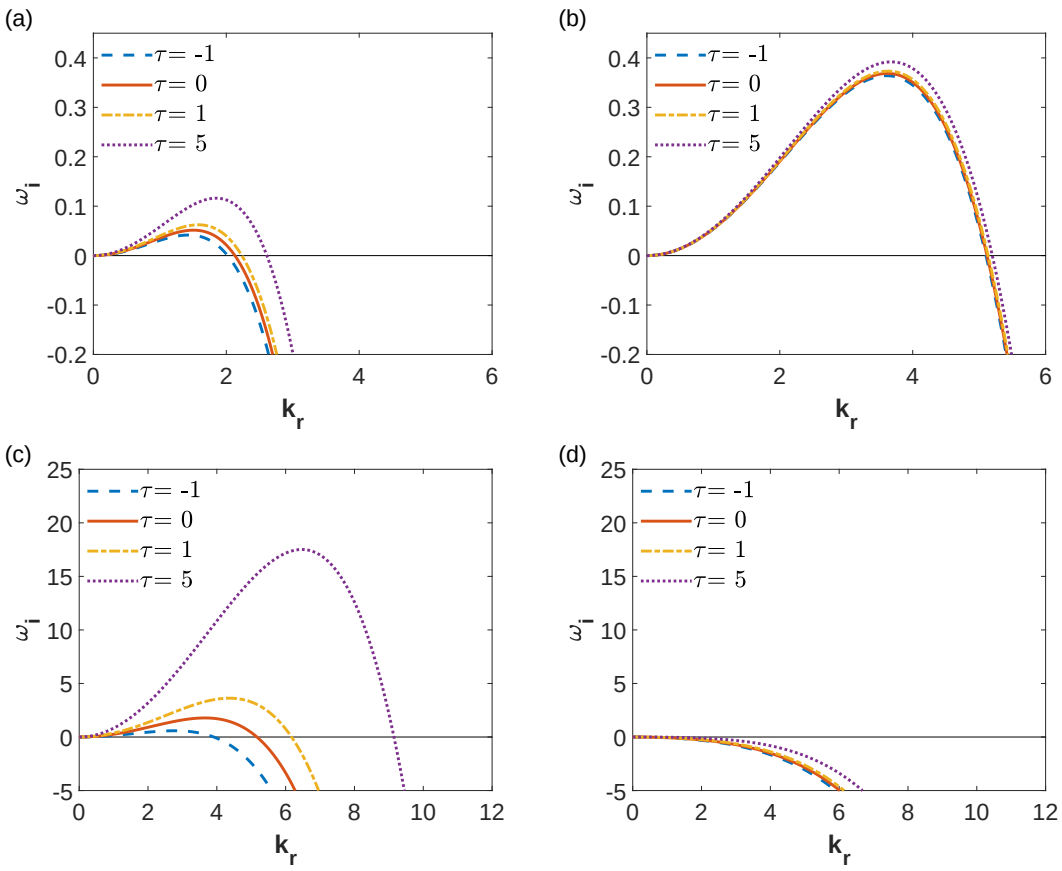

Figure 4.7: The effects of the vapor recoil parameter V_r on the temporal growth rate of a perturbation in a volatile moving base flow subject to the evaporation instability for $\beta = 20$, $\bar{M}$=0, $\bar{E} = 0.1$, $V_r = 1$. (a) Temporal growth rate vs wavenumber at $Re = 1$ and $t_f = 0$. (b) Temporal growth rate vs wavenumber at $Re = 1$ and $t_f = 0.6$. (c) Temporal growth rate vs wavenumber at $Re = 25$ and $t_f = 0$. (d) Temporal growth rate vs wavenumber at $Re = 25$ and $t_f = 0.6$.

4.4 Spatio-temporal stability analysis

The availability of the analytical dispersion relationship greatly simplifies the spatio-temporal analysis, since the temporal growth rate along any spatio-temporal ray $x/t = V$ can be computed directly using equation (3.31). To be noted is the fact that only the values of k resulting in real values of $\partial\omega/\partial k$ will be

retained. Spatio-temporal characteristics of the flow will be studied using (V, σ) diagrams since they present all the important points including maximum temporal growth rate, absolute growth rate, and the velocity of the wavepacket's edges. In order to obtain the (V, σ) diagrams, firstly $\partial\omega/\partial k$ is found analytically from equation (4.15) which in concise form gives

$$\frac{\partial \omega}{\partial k} = 4Ak^3 + 2Ck + D. \tag{4.22}$$

Then using equation (3.31) one can write

$$4Ak^3 + 2Ck + D - V = 0. \tag{4.23}$$

Equation (4.23) is then solved for the 3 spatial branches $k(\omega)$ which are of the form

$$a \pm ib, \qquad -a \pm ib, \quad \text{and} \quad 0 \pm ib.$$

The last two forms are discarded since they are nonphysical, and the temporal growthrate corresponding to a group velocity V is found using equation (3.33). Note that only unstable base flows will be studied in the following analysis, which again will use $\epsilon = 0.1$, $\bar{S} = 0.1$, $K = 0.1$, and $P = 1$.

4.4.1 Spatio-temporal analysis of an isothermal base flow

Figure 4.8 demonstrates the effect of the shear agent on the perturbation wave packet in an isothermal base flow. It can be seen that values of $\tau > 0$ cause an increase in the temporal growthrate and the expansion of the wavepacket, while the $\tau = -2$ caused the suppression of the peturbation wave packet along both axes.

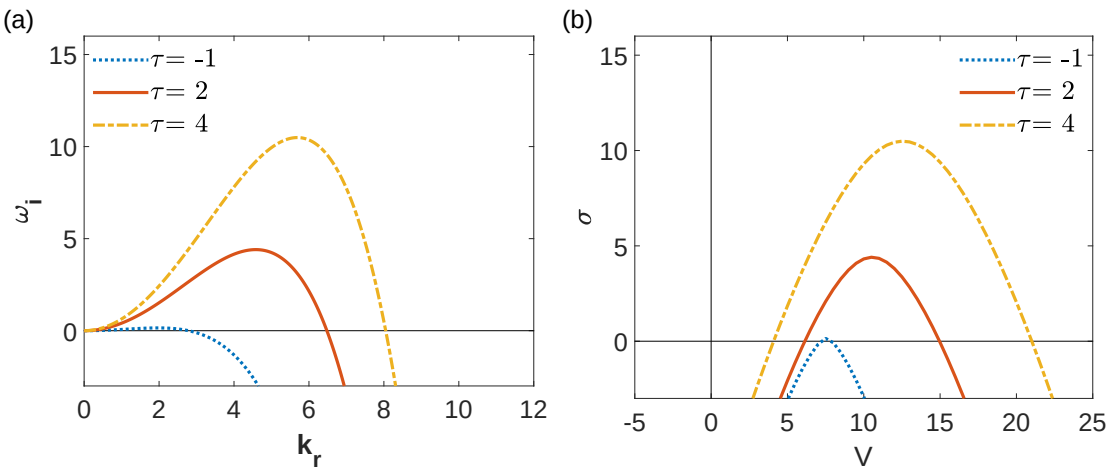

Figure 4.8: Spatio-temporal analysis of an isothermal base flow at different values of τ for $\beta = 20$, $Re = 25$, $\bar{M}$=0, $\bar{E} = 0$, $V_r = 0$. (a) Temporal growth rate vs wavenumber number. (b) Perturbation wave packet in the (V, σ) plane.

4.4.2 Spatio-temporal analysis of a base flow subject to the thermocapillary instability

- **Stationary base flow** ($\boldsymbol{\beta} = 0$)

The Marangoni instability mechanism isn't related to any particular flow direction. Therefore in the absence of any inertial effects; from the base flow's motion or the shear agent, it spreads symmetrically about the origin as seen in figure 4.9. In this case the base flow is absolutely unstable since the absolute temporal growthrate at the origin is larger than zero. However, when inertia is introduced by setting the value of $\tau = \pm 5$, the instability becomes convective since it is advected by the shear agent in the upstream or downstream direction depending on τ's sign. Note that for a stationary base flow the perturbation phase speed depends on τ, but the temporal growth rate does not. Therefore the peaks of the three wave packets in figure 4.9 are all at the same value.

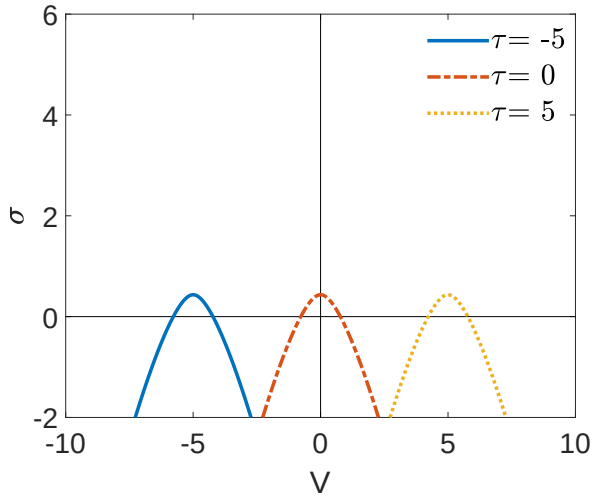

Figure 4.9: Spatio-temporal analysis of a stationary nonvolatile base flow subject to the Marangoni instability at different values of τ for $\beta = 0$, $Re = 1$, $\bar{M}$=2, $\bar{E} = 0$, $V_r = 0$.

For a stationary base flow, maps of absolute/convective transitions can be found by computing the absolute growth rate corresponding to different parameter sets in the $(\tau, \bar{M})$ space, as shown in figure 4.10.

It can be seen from figure 4.10 that increasing the Reynolds number results not only in the suppression of the perturbation temporally by reducing the range of parameters for which the base flow is unstable, but also in weakening absolute instabilities by reducing the absolute temporal growth rate. This behavior is due to the fact that increasing the value of Re has the combined effect of increasing hydrostatic pressure and also promoting the advection of the wavepacket with the flow.

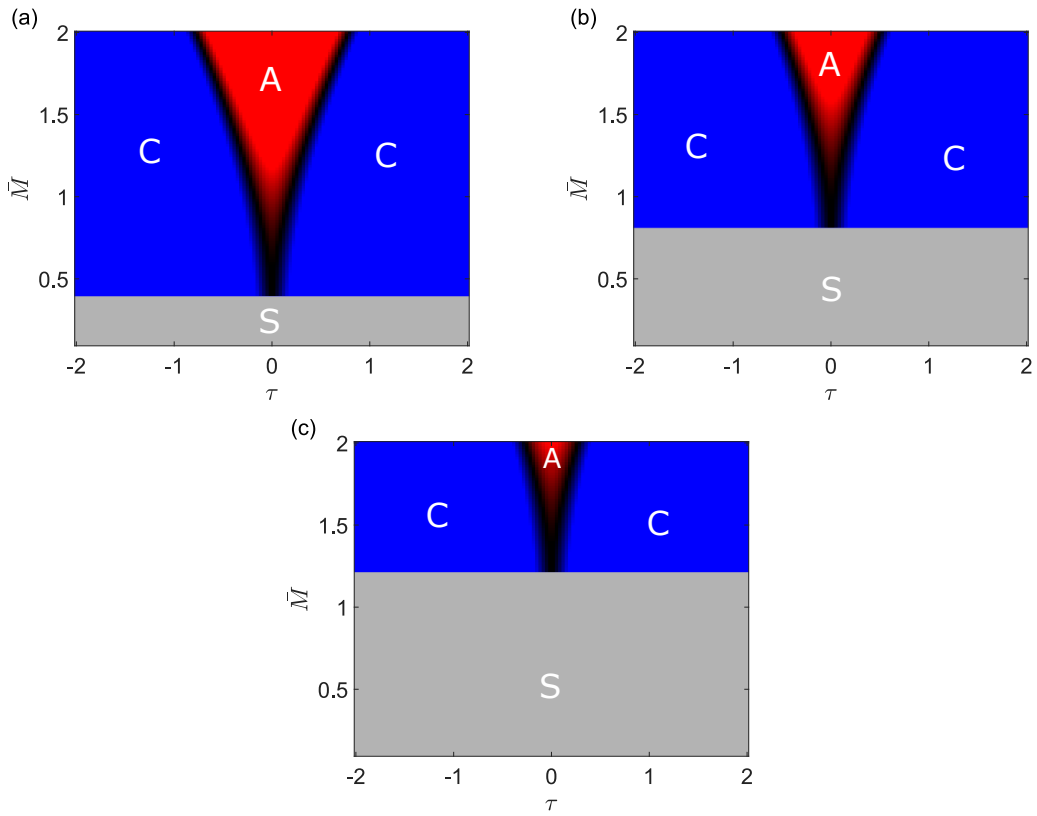

Figure 4.10: The effects of the shear agent on the absolute growth rate in the (τ, M) space for a stationary nonvolatile base flow subject to the Marangoni instability for $\beta = 0$, $\bar{E} = 0$, $V_r = 0$, and (a) $Re = 1$. (b) $Re = 2$. (c) $Re = 3$. Blue regions: convectively unstable, red region: absolutely unstable, gray region: stable.

- **Moving base flow ($\beta > 0$)**

As discussed previously, when the base flow is moving, the shear agent τ starts to affect both the perturbation phase speed and the temporal growth rate. This is seen in figure 4.11. Due to the effect the shear agent now has on the base flow's inertia, negative values of τ can cause an initially convective instability to become absolute and then upwards convective. However this is accompanied by a reduction in the maximum temporal growth rate, so for a negative enough value of τ, the perturbation is completely stabilized. Additionally, by comparing

figures 4.11(a,b) with 4.11(c,d), the role of Reynolds number in both stabilizing the S-mode and promoting the advection of the perturbation downstream can be seen.

Figure 4.12 shows the behavior of the H-mode instability under varying shear agent and Reynolds numbers. In contrast to the S-mode instability, increasing Reynolds number has the effect of promoting the advection of the wave packet and also increasing its temporal growth rate.

The absolute temporal growth rate in the $(Re, \bar{M})$ space is shown for different values of τ in figure 4.13. Figure 4.13(a) corresponding to $\tau = -4$ shows the existence of two regions where the instability is convectively unstable. The left-hand side region is due to upstream induced convection by the shear agent, while the right-hand side is due to convection by the flow's own inertia. The region in between is where these two effects are balanced such that instability becomes absolute and spreads in both directions. Figure 4.13(c) shows the disappearance of the stable region due to the increased downstream inertia imparted by the positive value of τ.

4.4.3 Spatio-temporal analysis of a base flow subject to the evaporation instability

In a manner similar to the Marangoni instability, the evaporation instability is not related to the flow's inertia and spreads symmetrically when the flow is stationary. However, mass loss due to evaporation changes the film thickness, which has significant effect on both the E-mode and the H-mode instabilities as explained ahead. First the spatio-temporal behavior of a stationary base flow is studied.

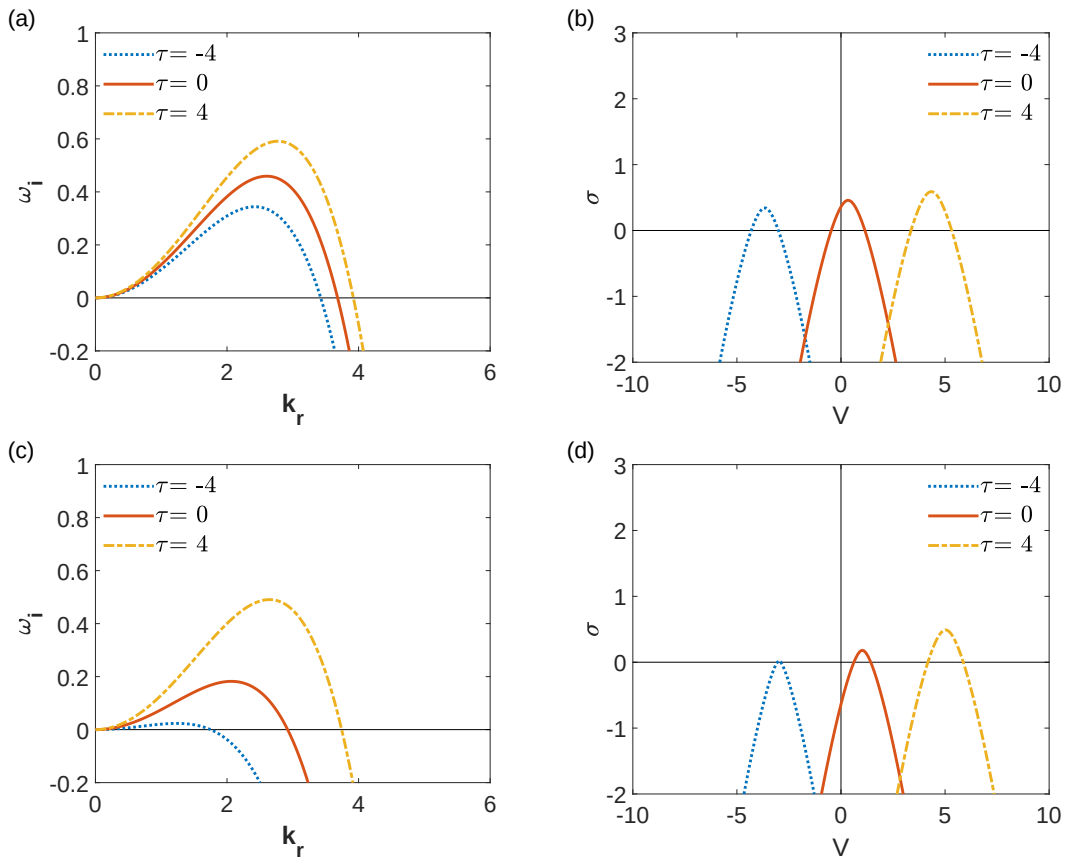

Figure 4.11: Spatio-temporal analysis of a moving nonvolatile base flow subject to the Marangoni instability at different values of τ for $\beta = 20$, $\bar{M}$=2, $\bar{E} = 0$, $V_r = 0$. (a) Temporal growth rate vs wavenumber number at $Re = 1$. (b) Perturbation wave packet in the (V, σ) plane at $Re = 1$. (c) Temporal growth rate vs wavenumber number at $Re = 3$. (d) Perturbation wave packet in the (V, σ) plane at $Re = 3$.

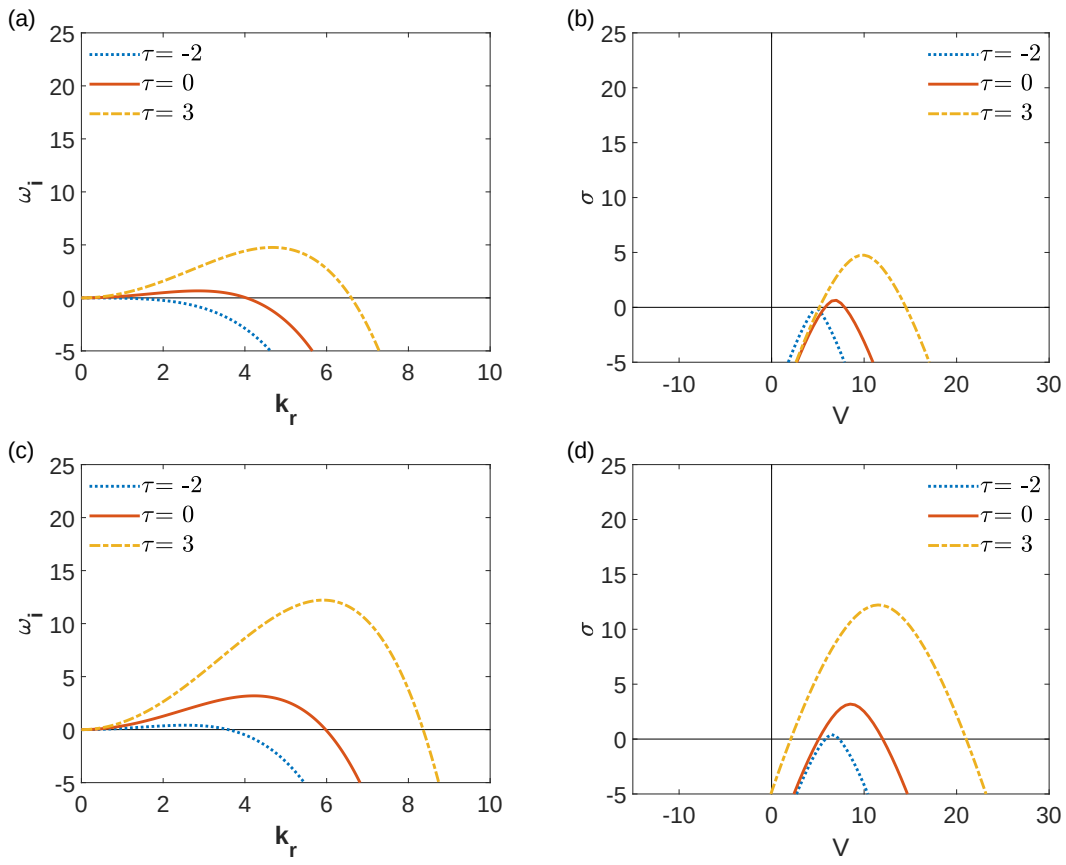

Figure 4.12: Spatio-temporal analysis of a moving base flow for subject to the H-mode instability modified by thermocapillarity at different values of τ for $\beta = 20$, $\bar{M}$=2, $\bar{E} = 0$, $V_r = 0$. (a) Temporal growth rate vs wavenumber number at $Re = 20$. (b) Perturbation wave packet in the (V, σ) plane at $Re = 20$. (c) Temporal growth rate vs wavenumber number at $Re = 25$. (d) Perturbation wave packet in the (V, σ) plane at $Re = 25$.

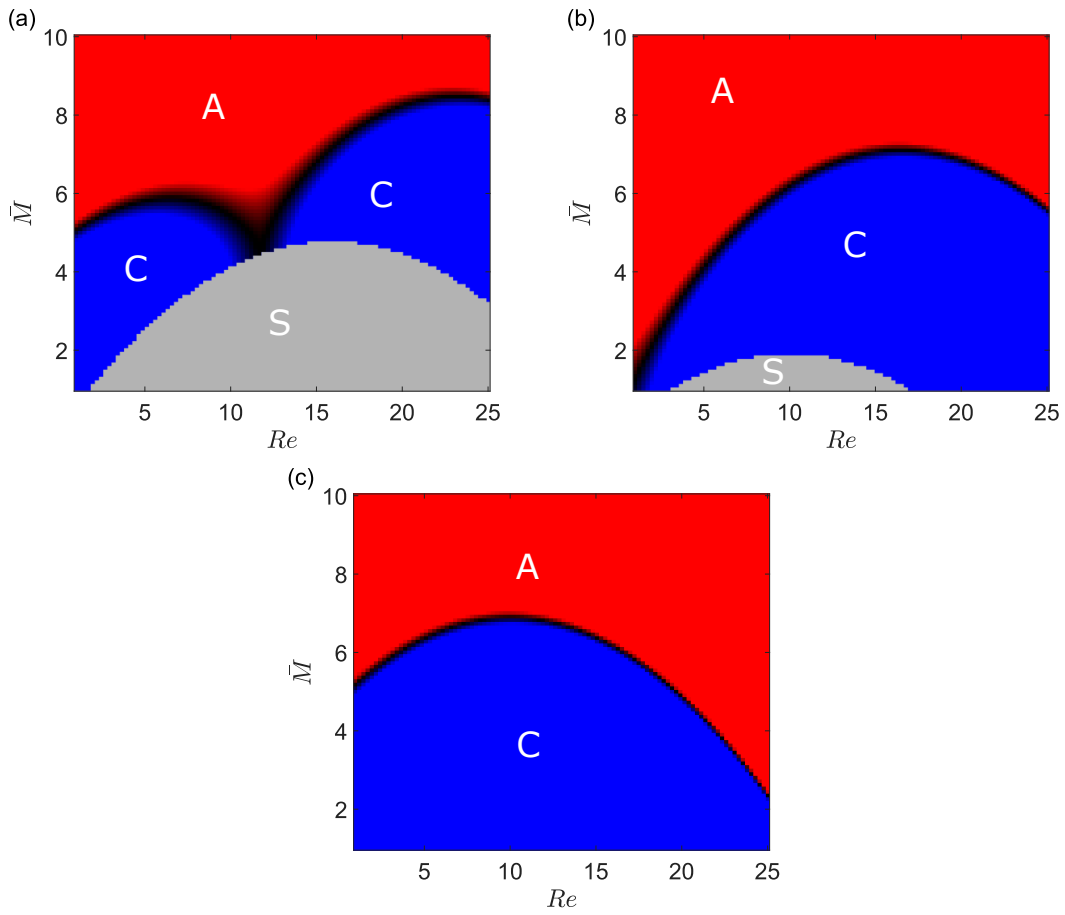

Figure 4.13: The effects of the shear agent on the absolute growth rate in the (Re, M) space for a nonvolatile base flow subject to the thermocapillary instability for $\beta = 20$, $\bar{E} = 0$, $V_r = 0$, and (a) $\tau = -4$. (b) $\tau = 0$. (c) $\tau = 4$. Blue regions: convectively unstable, red region: absolutely unstable, gray region: stable.

- **Stationary base flow** $(\boldsymbol{\beta} = 0)$

A stationary evaporating film is subject to the E-mode instability only, and as predicted by the purely temporal analysis in section 4.3, the shear agent does not affect the temporal growth rate of the perturbation, but causes a shift in its phase speed. Additionally, it was predicted that the reduction in film thickness strengthens the E-mode. However a spatio-temporal analysis shows that as the film thins, the instability becomes increasingly resistant to being convected away

by the flow's inertia. As for the evaporation rate represented by the parameter $\bar{E}$, changing its value does not have a significant effect on the perturbation since it does not contribute to the temporal growth rate and it only appears in the perturbation phase speed at $O(\epsilon)$.

The development of the absolute temporal growth rate in the (τ, V_r) space as the film evaporates is shown in figure 4.15. The same qualitative behavior in figure 4.14 is replicated as the parameter set for which the instability is absolute expands as the film height reduces. Note the reduction in the size of the stable region in the parameter space and then its complete elimination as t_f reduces.

- **Moving base flow ($\beta > 0$)**

Figure 4.16 demonstrates the already established spatio-temporal dynamics of a moving base flow; the shear agent changes both the temporal growth rate and the perturbation phase speed, and the reduction in base flow height promotes absolute instabilities. Additionally, as already established in the purely temporal analysis in section 4.3, the reduction in film height strengthens the E-mode instability while suppressing the H-mode. This results in a smaller perturbation wave packet indeed due to the reduction in the temporal growth rate as seen in figure 4.16(d).

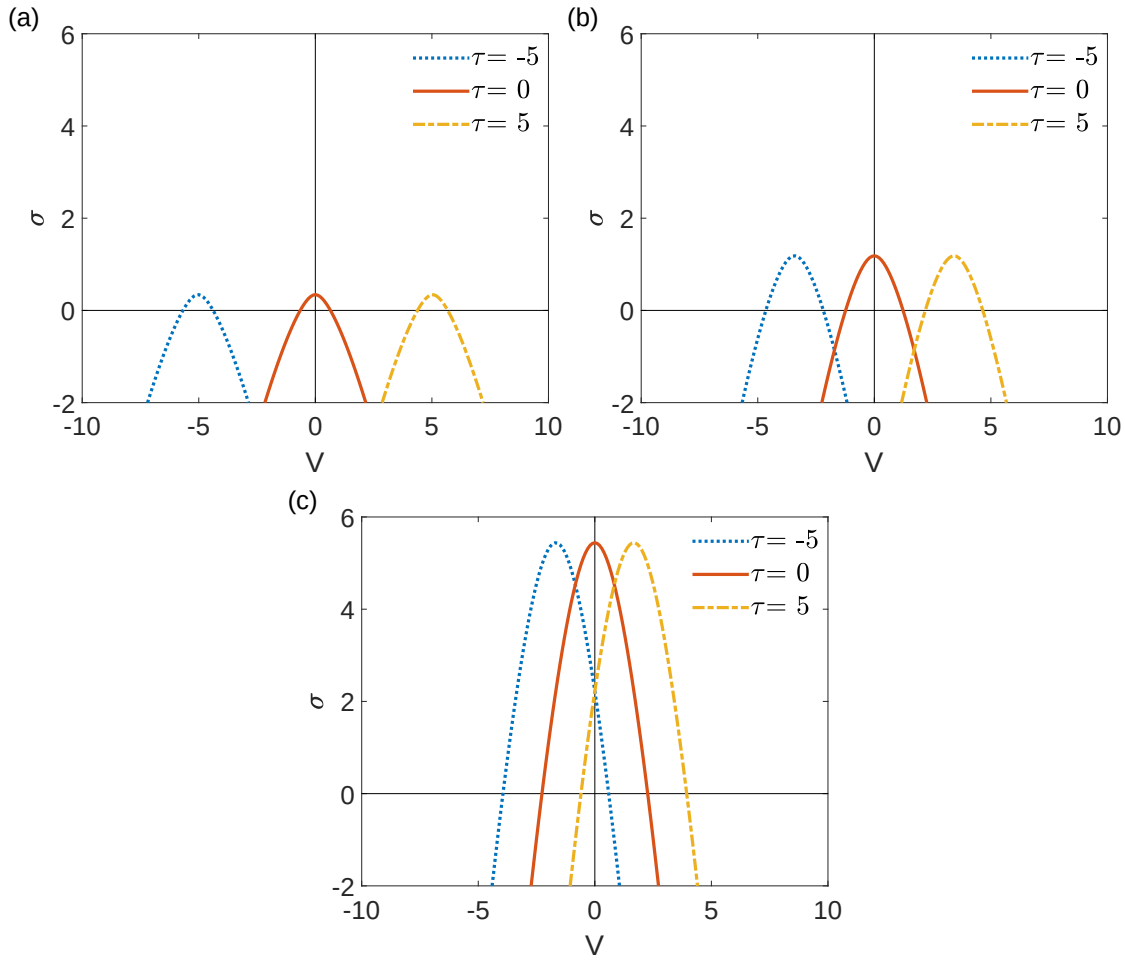

Figure 4.14: Spatio-temporal analysis of a stationary volatile base flow subject to the evaporation instability for $\beta = 0$, $Re = 1$, $\bar{M}$=0, $\bar{E} = 0.1$, $V_r = 2$, and (a) $t_f = 0$. (b) $t_f = 0.5$. (c) $t_f = 0.8$.

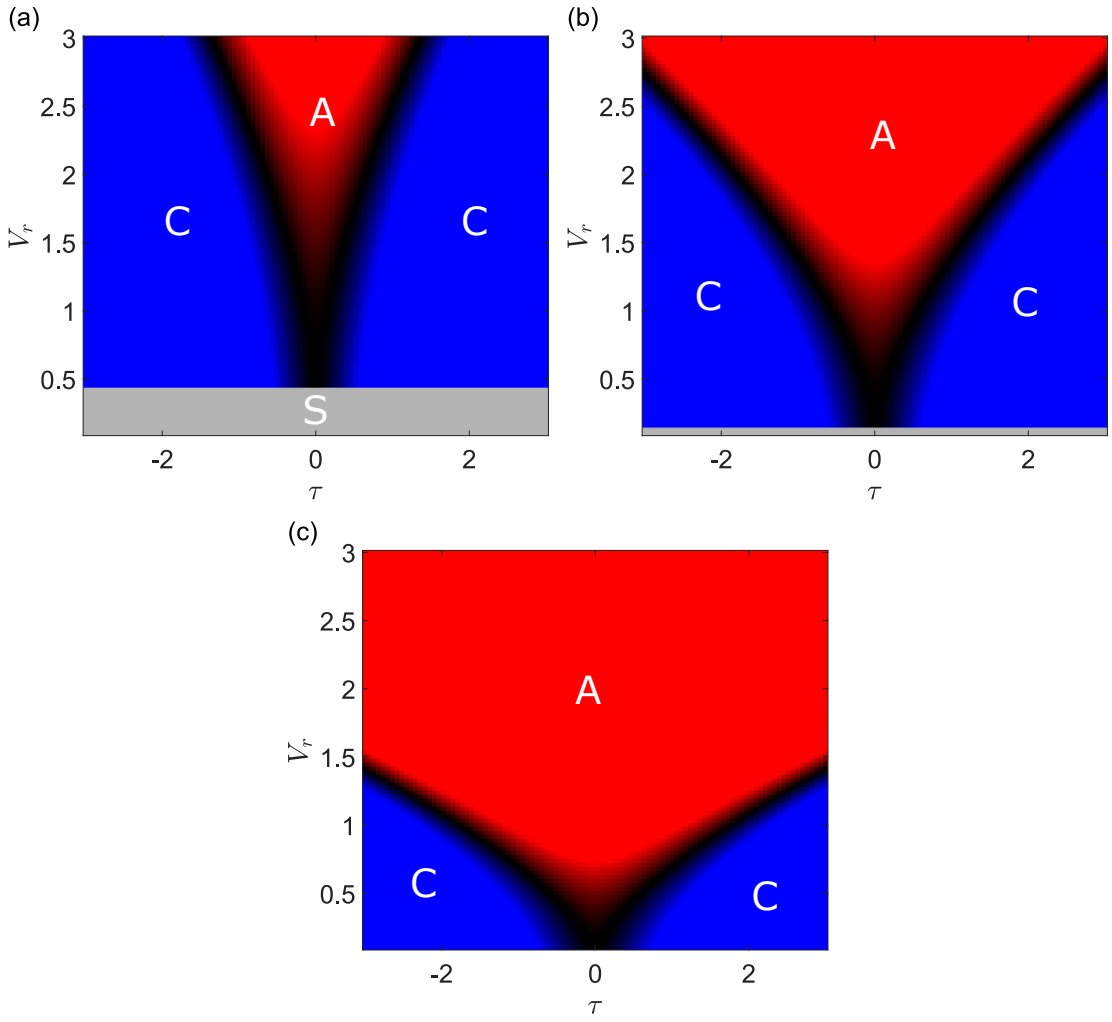

Figure 4.15: The effects of the shear agent on the absolute growth rate in the (τ, V_r) space for a stationary volatile base flow subject to the evaporation instability for $\beta = 0$, $Re = 1$, $\bar{M} = 0$, $\bar{E} = 0.1$, and (a) $t_f = 0$. (b) $t_f = 0.5$. (c) $t_f = 0.8$. Blue regions: convectively unstable, red region: absolutely unstable, gray region: stable.

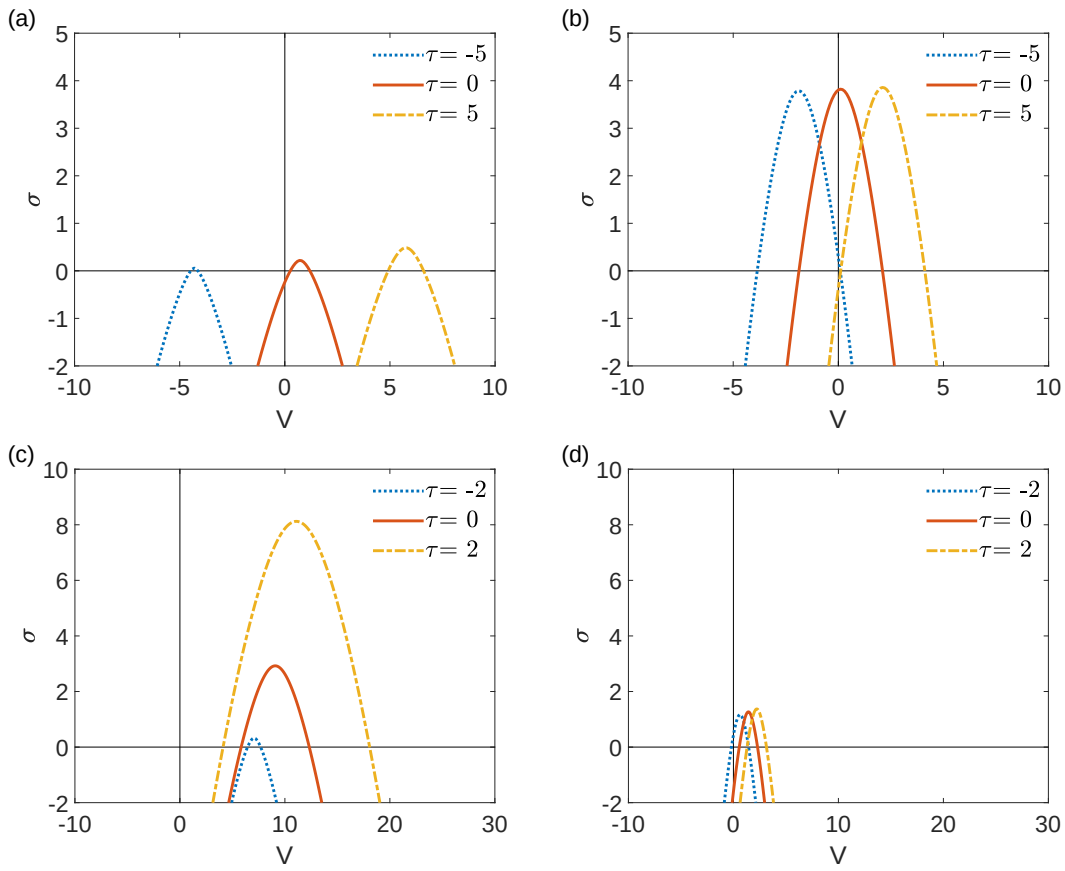

Figure 4.16: Spatio-temporal analysis of a moving volatile base flow subject to the E-mode instability for $\beta = 20$, $\bar{M}$=0, $\bar{E} = 0.1$, $V_r = 2$. (a) $Re = 1$ and $t_f = 0$. (b) $Re = 1$ and $t_f = 0.8$. (c) $Re = 25$ and $t_f = 0$. (d) $Re = 25$ and $t_f = 0.8$.

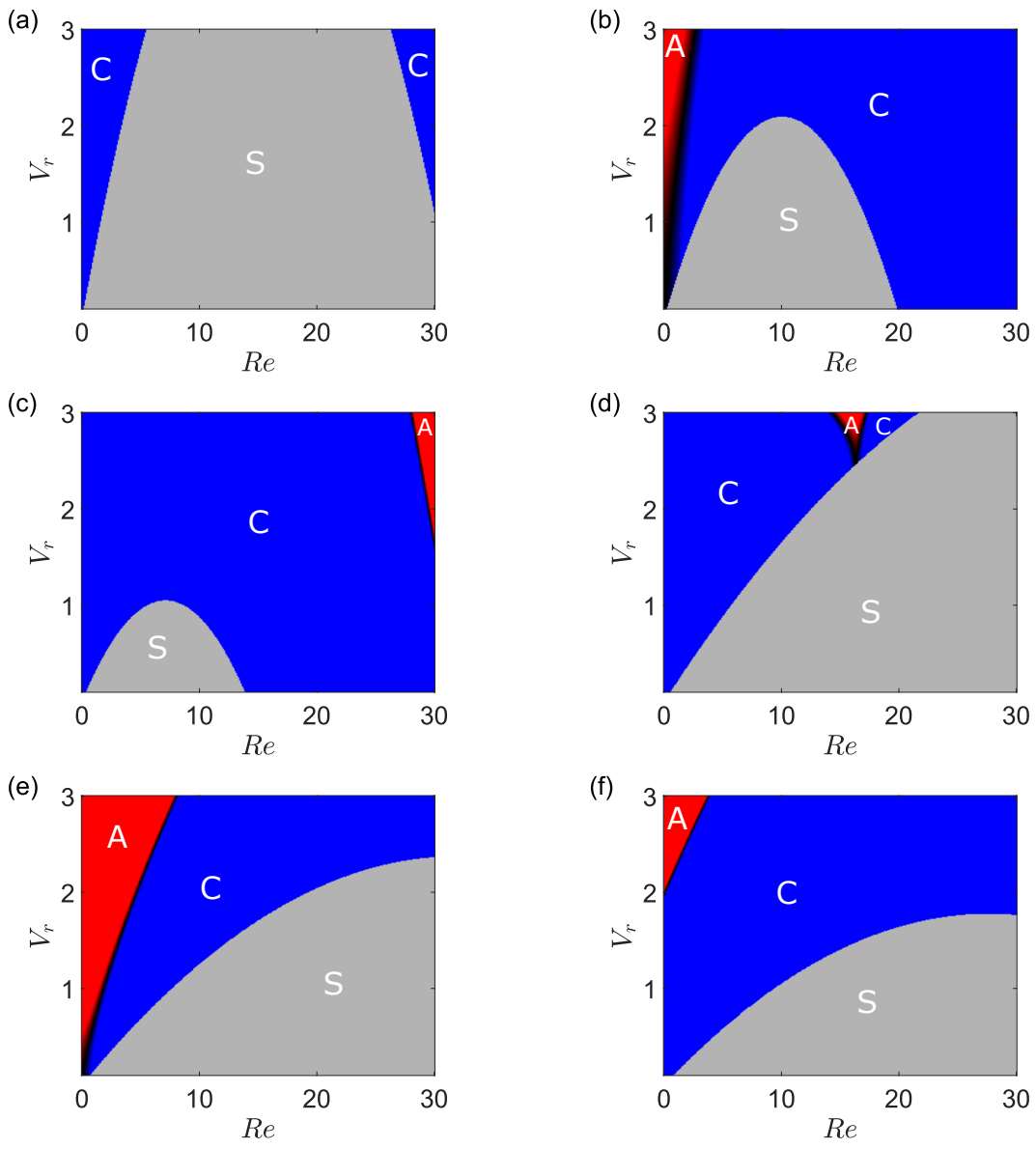

Figure 4.17: The effects of the shear agent on the absolute growth rate in the (Re, V_r) space for a volatile base flow subject to the evaporation instability for $\beta = 20$, $\bar{M}$=0, $\bar{E} = 0.1$. (a) $t_f = 0$ and $\tau = -4$. (b) $t_f = 0$ and $\tau = 0$. (c) $t_f = 0$ and $\tau = 2$. (d) $t_f = 0.5$ and $\tau = -4$. (e) $t_f = 0.5$ and $\tau = 0$. (f) $t_f = 0.5$ and $\tau = 2$. Blue regions: convectively unstable, red region: absolutely unstable, gray region: stable.

The effects of the shear agent and the reduction in film height can also be examined in the (Re, V_r) space as shown in figure 4.17. Comparing figures 4.17(a,b,c) to 4.17(d,e,f), it can be seen that the reduction in film height indeed promotes absolute instabilities as the parameter sets corresponding to absolute perturbations expanded. Additionally, the established effects of strengthening the E-mode instability and suppression of the H-mode one are seen as their corresponding regions expanded and shrunk, respectively. To be noted is the absolute instability region in figure 4.17(c) which has appeared due to the expansion of the perturbation wave packet to extend to the negative side of the V axis, as it is established that long wave model over-predicts the temporal growth rate as Reynolds number increases.

Chapter 5

Nonlinear evolution of the interface

5.1 Introduction

The interface evolution equation (4.9) is solved numerically in the MATLAB programming language using the *ODE15s* solver, which is a variable-step, variable-order solver (VSVO) based on the numerical differentiation formulas of orders 1 to 5. The initial version of the code was written by Dallaston et al. [26]. The problem was solved for two different boundary condition sets; a periodic domain employing a Fourier-spectral method for the spatial derivatives and a non-periodic domain using finite difference. Because a non-periodic domain is much more suitable to observe the simulated spatio-temporal evolution of the interface, the periodic solver was used mainly for the purposes of validating the numerical procedure. This was done by simulating the linear evolution of the interface and comparing the temporal growth rate extracted from the numerical data to that obtained using the linear temporal stability analysis presented in section 4.3.

Furthermore, additional validation was done by comparing the results to those

found by Joo et al. in [24] obtaining excellent agreement. Note that the numerical solution is terminated once minimum interface height approaches zero. The following constant values are used for all the cases simulated in chapter 5: $\epsilon = 0.1,\ \bar{S} = 1,\ K = 0.1,\ P = 1$.

5.2 Linear evolution of the interface over a periodic domain

Equation (4.9) is solved over a periodic domain where the spatial derivatives are evaluated using a spectral method with at least $N \geqslant 64$. The spatial derivatives are evaluated over $(0, 2\pi]$ and then reverted to physical space before time-step advancement.

The derivation of the relationship between the numerical and analytical temporal growth rates begins by assuming a normal mode solution of the form

$$h(t) = \bar{h}(t) + \xi H(t) e^{ikx}. \quad \text{where } \xi \ll 0. \tag{5.1}$$

By substituting this expression into (4.9) and following the same procedure in subsection 4.2.2, one obtains

$$\frac{\dot{H}}{H} = \omega_i. \tag{5.2}$$

where the left hand side can be obtained from the numerical interface evolution data through spectral analysis, and the right hand side can be obtain analytically. The validation was done for both inertial and thermal instabilities with the results presented in figure 5.1.

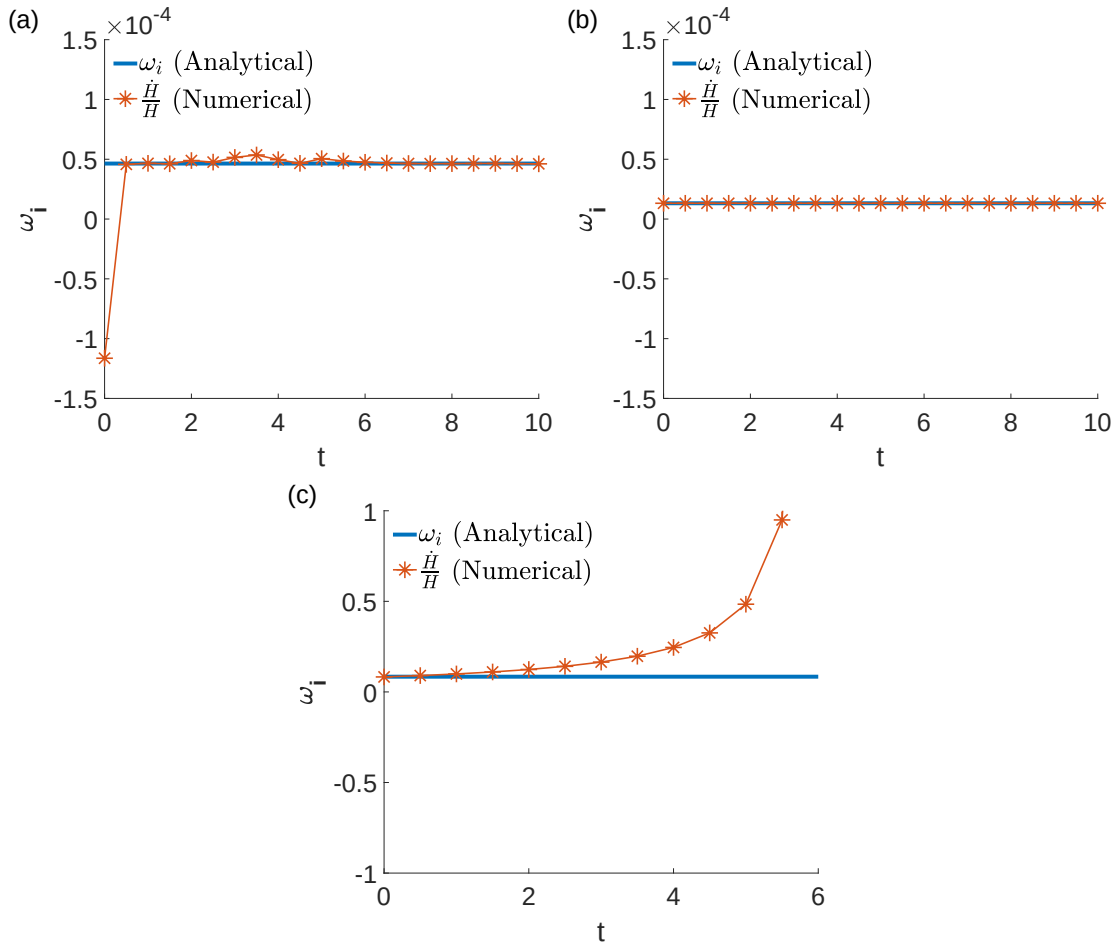

Figure 5.1: Comparison of the analytical and numerically extracted temporal growth rates. (a) Isothermal base flow: $\beta = 20,\ Re = 30, \bar{M} = 0,\ \bar{E} = 0,\ V_r = 0$. (b) Base flow subject to the Marangoni instability: $\beta = 0,\ Re = 1, \bar{M} = 2,\ \bar{E} = 0,\ V_r = 0$. (c) Base flow subject to the evaporation instability: $\beta = 0,\ Re = 1, \bar{M} = 0,\ \bar{E} = 0.1,\ V_r = 1$.

Note in figure 5.1(c) that due to the strength of the evaporation instability, the perturbation growth quickly becomes nonlinear and deviates from the constant value predicted by the linear model.

5.3 Non-linear evolution of the interface over a non-periodic domain

Once the numerical procedure was verified the solver was used to simulate the interface for the different flow domains. The interface is perturbed at the spatio-temporal $(x, t) = (0, 0)$ by a of Guassian pulse of the form

$$h(x, 0) = \bar{h}(x, 0) + 0.1e^{-x^2/2} \tag{5.3}$$

The simulation results are presented ahead. Note that the all of the flows considered where correctly classified by the linear stability framework presented in chapter 4.

5.3.1 Isothermal base flow

Figure 5.2 shows an isothermal base flow driven by gravity in the absence of any thermal or gas shear effects. In figure 5.2(a), the parameter set results in a stable flow. If Reynolds number is increased beyond its critical value of $Re = 20.01$ for the current parameter set, the H-mode is triggered and the perturbation starts to grow as it is being advected downstream. This is shown in figure 5.2(b). To demonstrate the suppression of the H-mode by a counter-flowing shearing gas, τ is set to -3 and the flow is indeed stabilized, as demonstrated by 5.2(c).

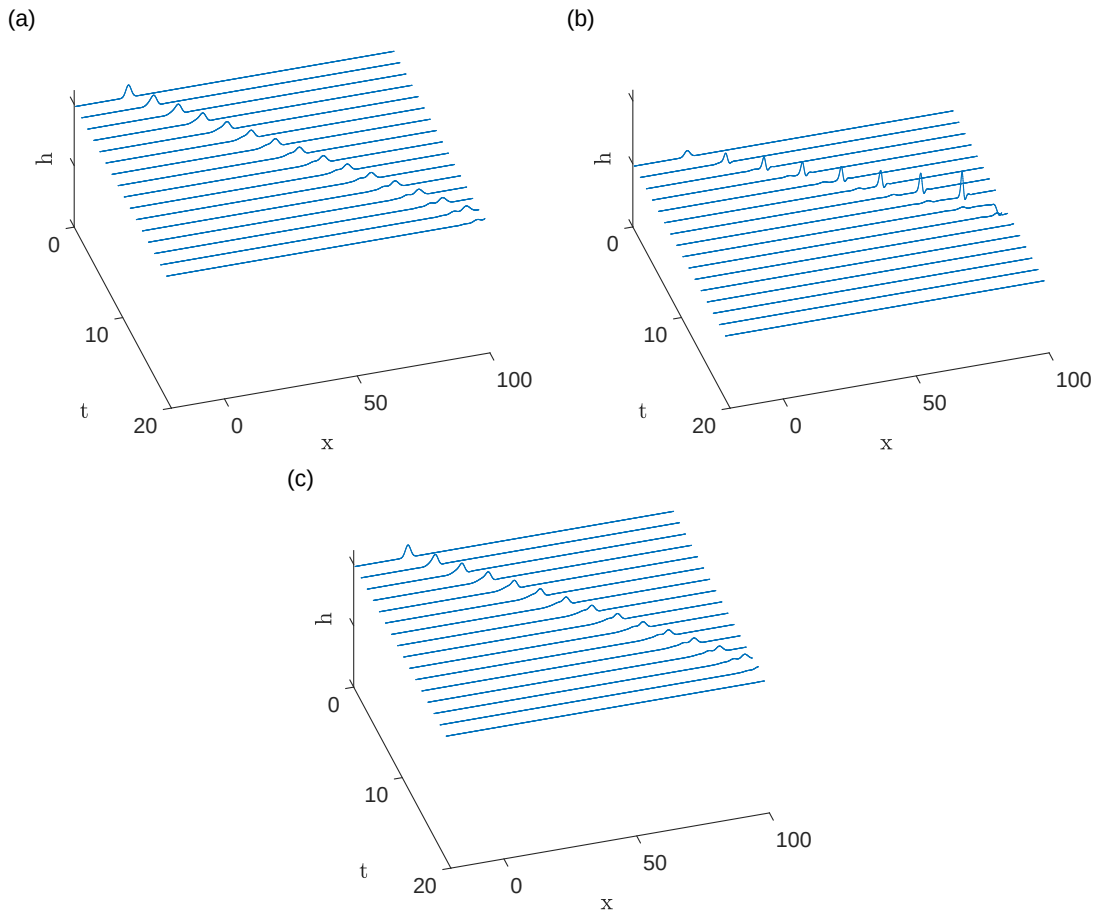

Figure 5.2: Time evolution of the interface of a moving isothermal base flow for $\beta = 20$, $\bar{M}$=0, $\bar{E} = 0$, $V_r = 0$. (a) $Re = 15$ and $\tau = 0$. (b) $Re = 25$ and $\tau = 0$. (c) $Re = 25$ and $\tau = -3$.

5.3.2 Base flow subject to the Marangoni instability

An intially stationary nonvolatile base flow subject to the Marangoni S-mode instability is shown in figure 5.3. The perturbation's absolute nature is strikingly obvious in figure 5.3(a) as it proceeds symmetrically in both directions since there no inertia to interfere with its progress in the domain. However, if the base flow's Reynolds number is increased, as predicted by linear stability theory, the perturbation is suppressed due to the stronger stabilizing hydrostatic pressure as seen in figure 5.3(b).

As discussed previously, the shear agent does not change the temporal growth rate of a stationary perturbation i.e it can not destabilize an inherently stable flow on its own. Therefore, to simulate its effect, the unstable parameter corresponding to figure 5.3(b) is used albeit with non-zero values of τ. The results are presented in figure 5.4 where it is clear that an absolute-convective transition has occurred as the perturbation packet is clearly traveling away from the origin. Note the symmetry due to the absence of the base flow's inertia.

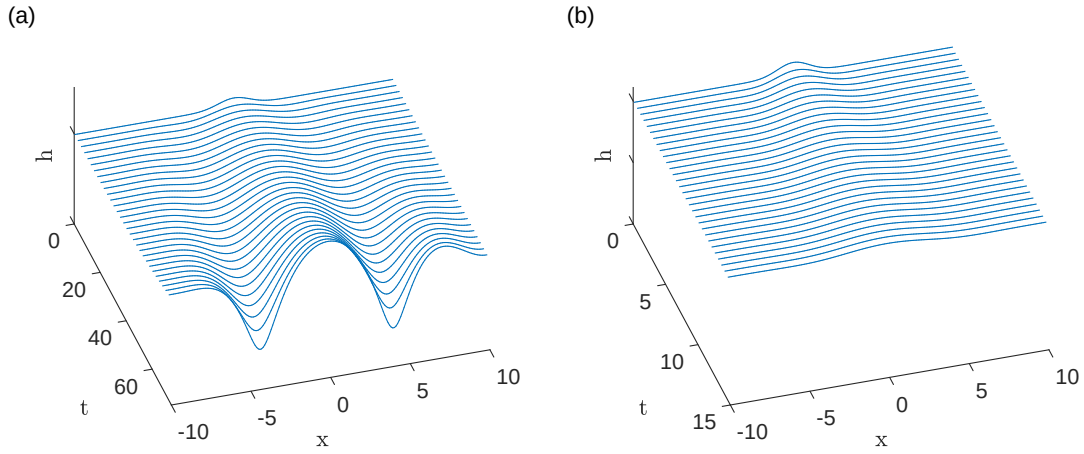

Figure 5.3: Time evolution of the interface of a stationary nonvolatile base flow subject to the Marangoni instability for $\beta = 0$, $\bar{M} = 2$, $\bar{E} = 0$, $V_r = 0$, $\tau = 0$, and (a) $Re = 1$. (b) $Re = 5.5$.

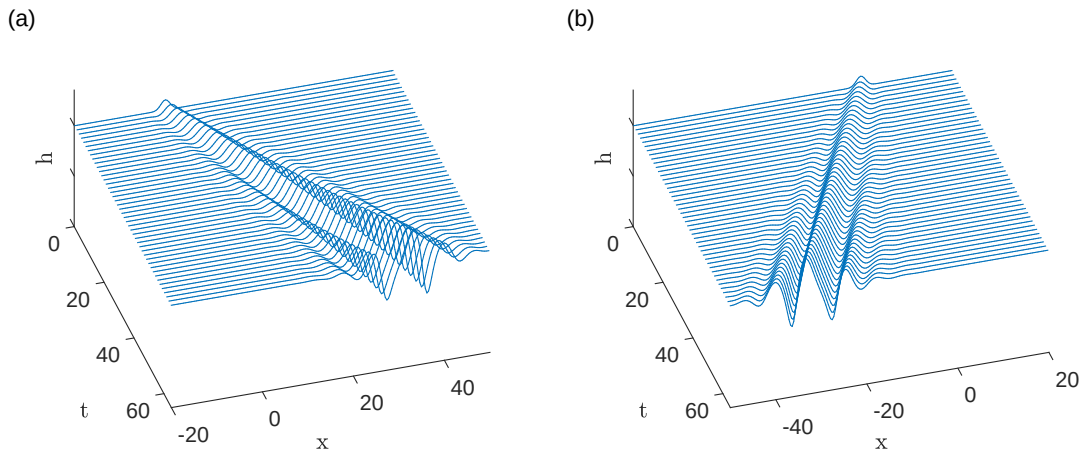

Figure 5.4: Time evolution of the interface of a nonvolatile base flow subject to the Marangoni instability, convected under the influence of the shear agent for $\beta = 0$, $Re = 1$, $\bar{M} = 2$, $\bar{E} = 0$, $V_r = 0$, and (a) $\tau = 0.5$. (b) $\tau = -0.5$.

When the base flow has inertia, the S-mode instability which is absolute for a stationary base flow without shear effects, can become convective under the influence of the flow's own inertia as seen figure 5.5(a). However, under these conditions, negative values of the shear agent can cause a convective-absolute transition by forcing part of the perturbation wavepacket to travel upstream, as predicted by the linear stability analysis. This result is show in figure 5.5(b). If the shear agent's value is reduced even further, then the instability will become convective again, albeit in the upstream direction, as shown in figure 5.5(c)

5.3.3 Base flow subject to the evaporation instability

The dynamics of a stationary base flow subject to the evaporation instability in the absence of inertial forces are shown in figure 5.6 for $t_f = 0$ and $t_f = 0.5$. Note how the narrower width of the perturbation wave is consistent with what was predicted by the linear spatio-temporal analysis at lower film height, and again the symmetry of the perturbation spread due to the absence of the base flow's inertia.

The effects of the shear agent τ on the evaporating base flow are qualitatively similar to those of the thermocapillary instability as it causes an absolute convective transitions as shown in figures 5.7(a,b). Note how the reduction in film height causes the film to resist the advection of the perturbation indicating that a further reduction in film height will lead to the instability becoming absolute. This is indeed confirmed and is shown in figure 5.8

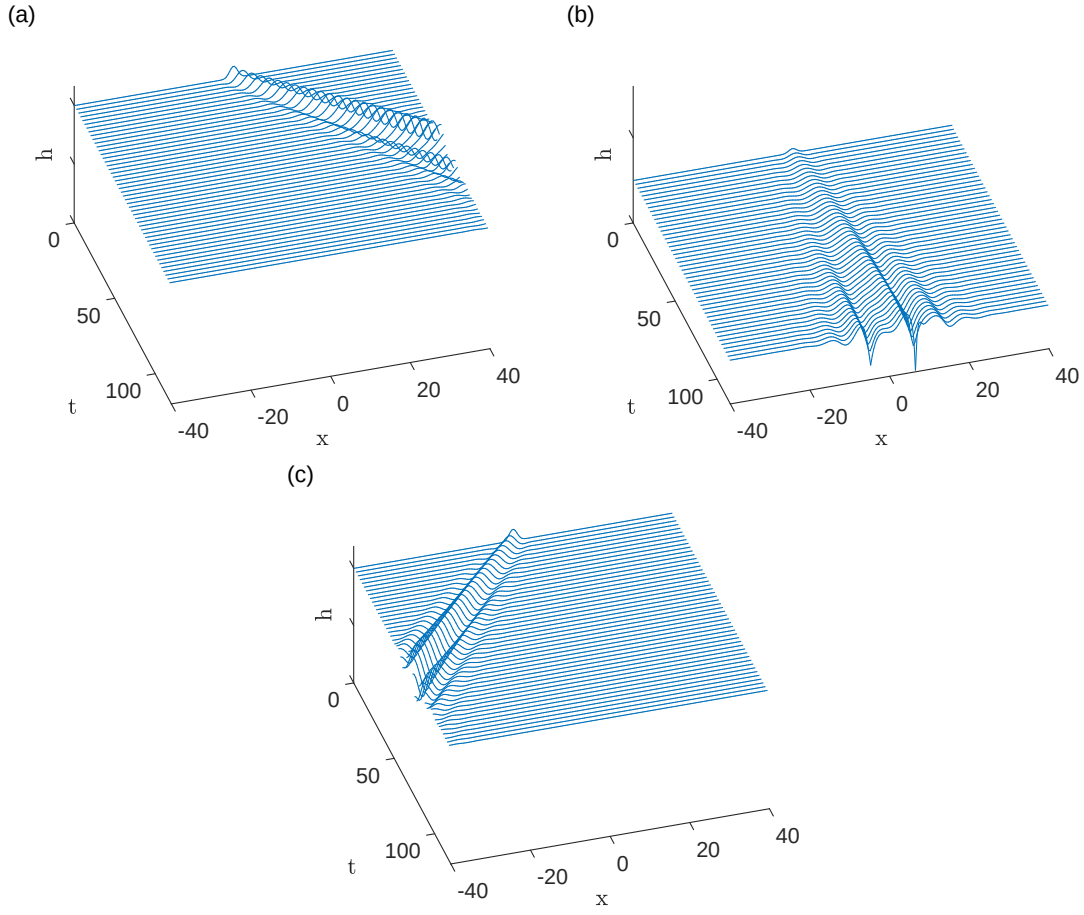

Figure 5.5: Time evolution of the interface of a moving nonvolatile base flow subject to the Marangoni instability for $\beta = 20$, $Re = 1.8$, $\bar{M} = 2$, $\bar{E} = 0$, $V_r = 0$, and (a) $\tau = 0$. (b) $\tau = -0.6$. (c) $\tau = -1.2$.

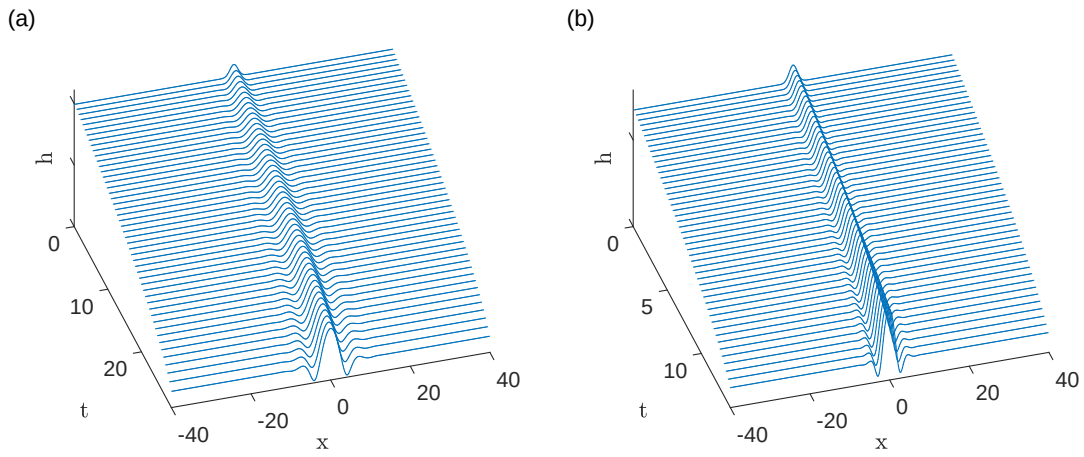

Figure 5.6: Time evolution of a stationary volatile base flow subject to the evaporation instability for $\beta = 0$, $Re = 1$, $\bar{M}$=0, $\bar{E} = 0$, $V_r = 0$, and (a) $t_f = 0$. (b) $t_f = 0.5$.

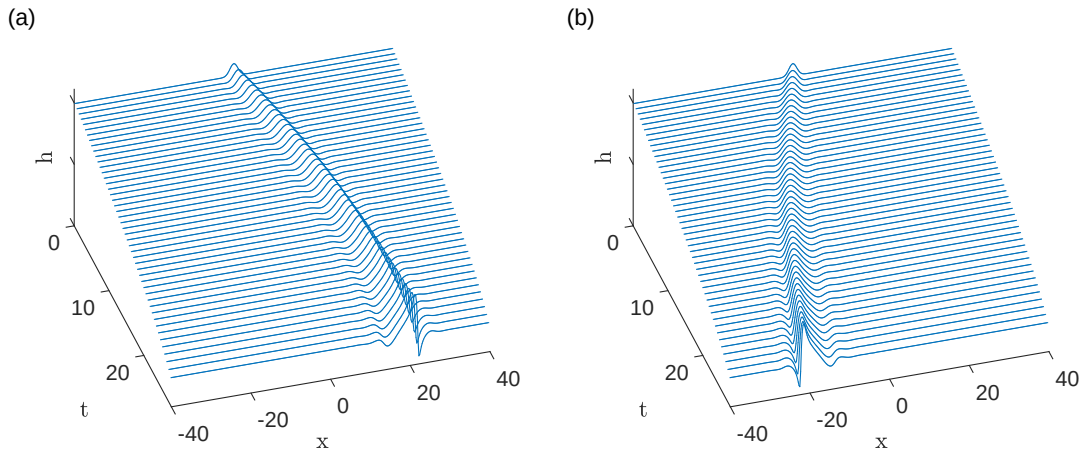

Figure 5.7: Time evolution of a volatile base flow subject to the evaporation instability for $\beta = 0$, $Re = 1$, $\bar{M}$=0, $\bar{E} = 0$, $V_r = 0$, $t_f = 0$, and (a) $\tau = 1$. (b) $\tau = -1$.

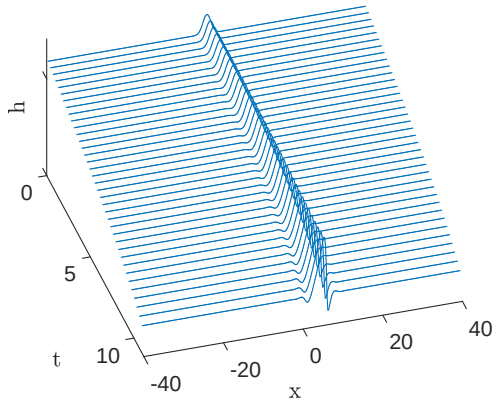

Figure 5.8: Time evolution of a volatile base flow subject to the evaporation instability for $\beta = 0$, $Re = 1$, $\bar{M}$=0, $\bar{E} = 0$, $V_r = 0$, $t_f = 0.6$, $\tau = 1$.

5.4 Rupture analysis

Both thermocapillary and evaporation instabilities can cause the liquid film to rupture, which can have a significant negative effect on applications sensitive to the liquid film's integrity. For instance in coating processes a rupture in the film during application can ruin the resultant surface, or in cooling processes a rupture point can quickly expand into a dry spot causing the local temperature to exceed the device's design threshold.

It is expected that a shearing gas can play a role in mitigating these problems by either preventing rupture all together or altering the evolution of the interface such that film rupture is delayed until the film exits the region where its rupture is detrimental to the system. Note that in the following analysis in the presence of multiple rupture points that the rupture location is considered to be the point closest to the inlet.

It is expected that when the flow has sufficient inertia that rupture is prevented naturally since the flow's perturbation will be carried away from the origin due to the base flow's convective highly convective dynamics. Therefore the focus

in the following analysis will be on cases where the base flow is governed by a combination of parameters resulting in low net inertia. Note that unless otherwise stated, the following constant values are used in the following analysis: $\epsilon = 0.2,\ \bar{S} = 1,\ K = 0.1,\ P = 1$.

5.4.1 Parametric study

1. Rupture caused by thermocapillary instabilities of a non-volatile film

Figure 5.9 shows that the stream-wise rupture location x_r moves closer to the flow inlet as the modified Marangoni number increases. This is expected since larger values of $\bar{M}$ correspond higher temporal growth rates leading to a faster reduction in the minimum film height. Interestingly, at a certain value of $\bar{M}$, the rupture location jumps suddenly downstream, and then again proceeds to move upstream. This trend is persistent for all the values of τ studied. This behavior is explained by examining the interface profiles in the (x, h) plane at rupture as shown in figure 5.10.

Taking the data plot corresponding to $\tau = 0$, the interface profiles in figure 5.10 depict a travelling wave being deformed by thermocapillary forces where the film is heading towards rupture at both of the wave's edges. The first rupture profile corresponds to the point labeled P1, and it is seen that rupture occurs at the wave's trailing edge since the film thins near it faster than at its leading edge.

However as the value of $\bar{M}$ is increased, the rate of decrease in minimum film thickness at the wave's leading edge starts to match that at the trailing edge which is shown in figure 5.10(b). Here rupture seems to occur effectively simultaneously at both of wave's edges. Note that we still consider the rupture to occur at the trailing edge since it is closer to the flow inlet.

Figure 5.10(c) corresponds to the point P3 which clearly shows rupture occurring at the wave's leading edge which explains the sudden increase in rupture

distance. Finally with higher values of $\bar{M}$, the original trend of the rupture point moving towards the flow inlet is again recovered which is seen in figure 5.10(d) corresponding to the point P4.

As for the effect of $\bar{M}$ on rupture time t_r, it does not display the harmonic variation of x_r and decreases continuously with higher values of $\bar{M}$ as shown in figure 5.9(b). Notably, the shear agent doesn't have an effect on rupture time for the parameter set due to the combination of small values of τ and the relatively low flow inertia.

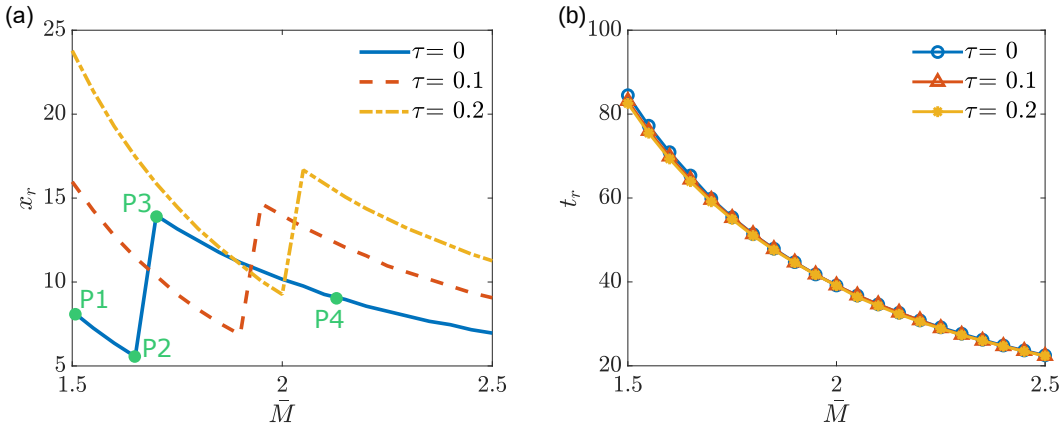

Figure 5.9: Rupture location and time versus $\bar{M}$ for different values of τ for $Re = 1,\ \beta = 10,\ \bar{E} = 0,\ V_r = 0$. (a) x_r vs $\bar{M}$. (b) t_r vs $\bar{M}$.

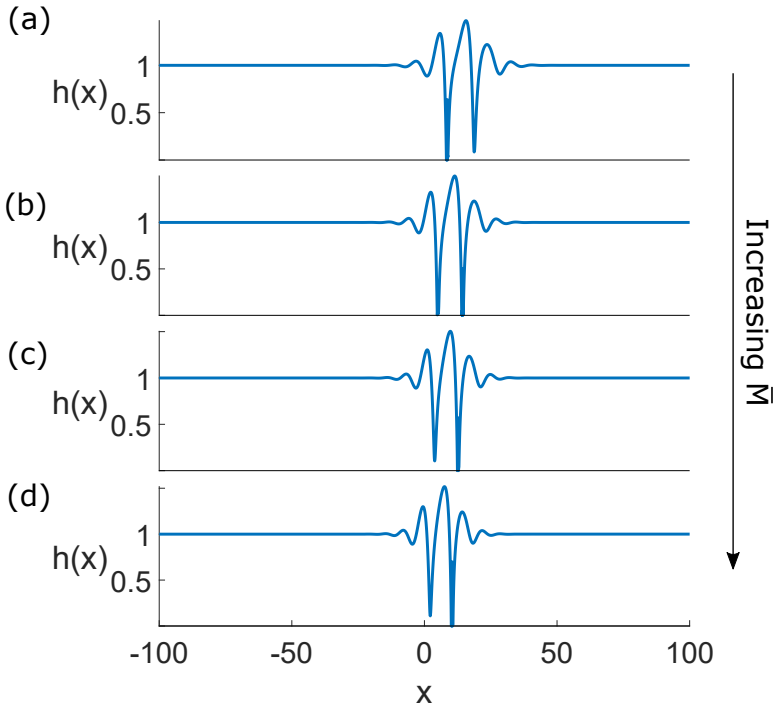

Figure 5.10: Rupture profiles corresponding to different values of $\bar{M}$ for $\beta = 10$, $Re = 1$, $\bar{E} = 0$, $V_r = 0$, $\tau = 0$, and (a) P1, $\bar{M} = 1.5$. (b) P2, $\bar{M} = 1.7$. (c) P3, $\bar{M} = 1.8$. (d) P4, $\bar{M} = 2.1$.

The effects of a counter-flowing gas on rupture location are seen in figure 5.11. It is seen negative values of τ resist the advection of the perturbation away from its origin. Specifically $\tau = -0.2$ causes it to persist approximately at its origin for the range of $\bar{M}$ investigated. However as the value of τ is decreased further to -0.3, the rupture point starts to move upstream. As for t_r the negative sign of τ doesn't seem to cause different behavior.

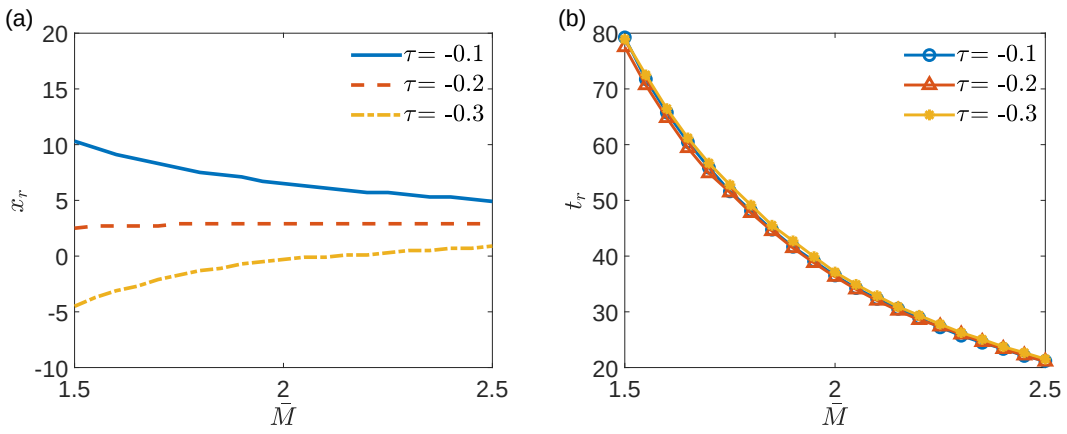

Figure 5.11: Rupture location and time versus $\bar{M}$ for different values of τ for $Re = 1,\ \beta = 10,\ \bar{E} = 0,\ V_r = 0$, and (a) x_r vs $\bar{M}$. (b) t_r vs $\bar{M}$.

2. Rupture caused by evaporation instabilities of a volatile film

Next the effects of the shear agent on the location of rupture caused by evaporation instabilities is investigated for two base flows with different evaporation rates. The results are shown in figure 5.12. It is found that the shear agent's role is severely diminished in determining the rupture point in a volatile base flow, as the dynamics are dominated by the evaporation rate and ultimately film thickness.

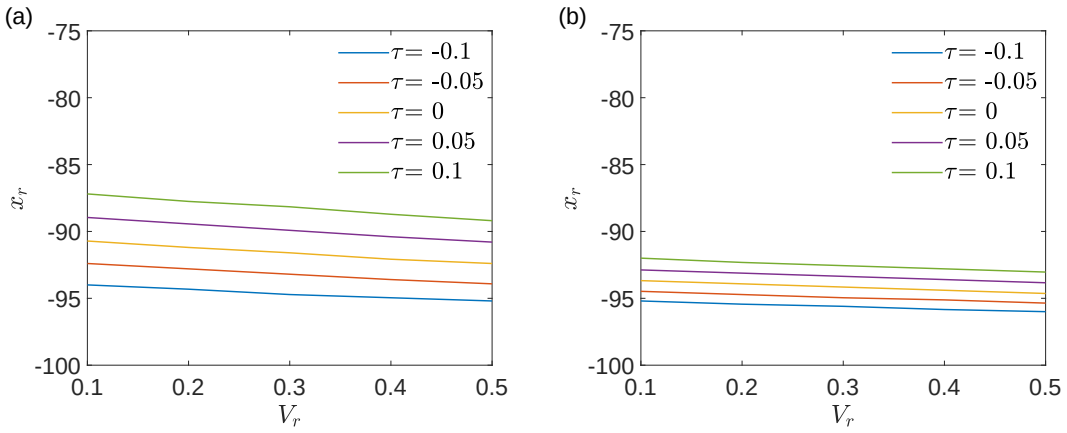

Figure 5.12: Rupture location versus V_r at different values of τ for $\beta = 10,\ Re = 1,\ \bar{M} = 0$, $t_f = 0$, and (a) $\bar{E} = 0.01$. (b) $\bar{E} = 0.02$.

5.4.2 Self-similarity analysis

In order to investigate how the shearing gas represented by the shear agent affects the thermocapillary rupture behavior at very small scales, the film's dynamics very close to rupture are studied via a self-similarity analysis. The following analysis is inspired by the work in [27].

The evolution of a stationary liquid film under the influence of only gravity and thermocapillarity can be modeled by a generalized one dimensional Cahn-Hillard equation [27] of the form

$$\partial_t h + \partial_x \left(h^{\mu-1} \partial_x h + h^{\mu} \partial_{xxx} h \right) = 0, \qquad \mu \geqslant 3 \tag{5.4}$$

The corresponding expression from the interface evolution equation (4.9) is

$$\partial_t h + \tau h \partial_x h + \epsilon \partial_x \left[\bar{M} \frac{h^2 \partial_x h}{(\bar{h}+K)^2} - \frac{1}{3} Recos\beta h^3 \partial_x h + \bar{S} h^3 \partial_{xxx} h \right] = 0. \tag{5.5}$$

In order to match the form in equation (5.4), $\tau h \partial_x h$ is integrated to give $\tau h^2/2 + C$ and is then inserted into equation (5.5).

Now equation (5.5) reads

$$\partial_t h + \partial_x \left[\epsilon \bar{M} \frac{h^2 \partial_x h}{(h+K)^2} - \frac{1}{3} \epsilon Recos\beta h^3 \partial_x h + \epsilon \bar{S} h^3 \partial_{xxx} h + \frac{\tau h^2}{2} \right] = 0. \tag{5.6}$$

Taking the limit $h \to 0$ yields the same expression presented in [27], and the new term containing the shear agent vanishes. Therefore following the same procedure as the authors and assuming self similar solutions of the form

$$h = t^{-1} G(\eta), \text{ and } \quad \eta = x\sqrt{t}. \tag{5.7}$$

One arrives at an ordinary differential equation of the form

$$\eta \partial_\eta G - 2G + 2 \left(G^2 \partial_\eta G + G^3 \partial_{\eta\eta\eta} G \right) = 0, \tag{5.8}$$

which demonstrates an infinite number of oscillations of increasing amplitudes [27], and is unaffected by the shear agent quantity..

Therefore it is concluded that the shear agent does not affect the physical rupture process as its contribution vanishes at such a small scale. This fact is

confirmed by plotting the minimum film height as a function of time which is shown in figure 5.13. As expected, the slope of the minimum height function is unchanged as it approaches zero for the different values of τ which were investigated. This is further confirmed by the plot of h_{min} vs $(t-t_r)$ in log scale as shown in figure 5.13(b) which confirms that the film height function decays according to the same power law since the functions in log scale have approximately the same slope as $h \to 0$.

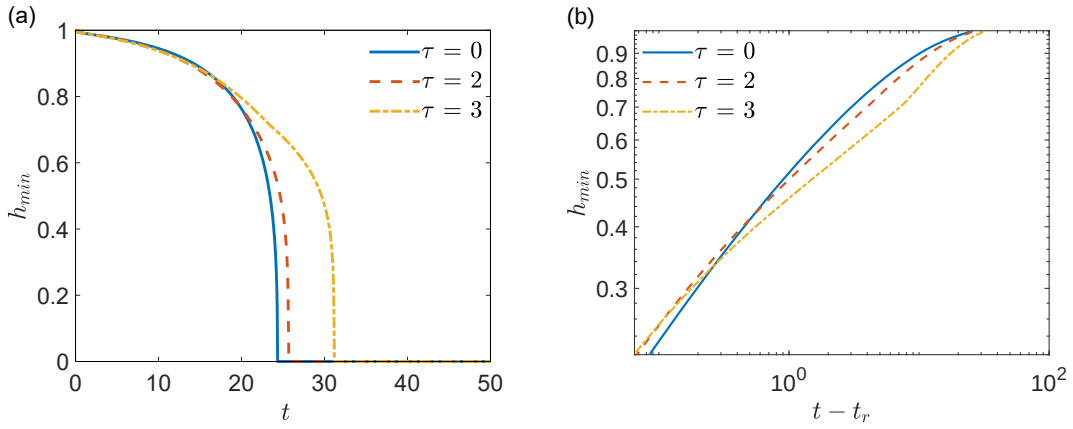

Figure 5.13: The effects of the shear agent on the minimum height function h_{min} for $Re = 1,\ \beta = 0,\ K = 0.01,\ \bar{M} = 2,\ \bar{E} = 0,\ V_r = 0$. (a) h_{min} vs t. (b) h_{min} vs $t - t_r$.

Chapter 6

Conclusions and outlooks

6.1 Summary of findings

In summary, the interface evolution obtained via long wave theory is extended to include the effects of a shearing gas via the introduction of a shear agent parameter modeling a constant value of shear stress along the liquid-gas interface. Subsequently linear temporal and spatio-temporal analyses were performed in order to determine the effects of the different parameters, especially the shear agent, on the stability characteristics of the base flow.

It was concluded that the shear agent acts as a modifier to the base flow's existing inertia and therefore cannot create perturbations in a base flow devoid of inertia. Additionally, it is found that it does not affect the thermal contributions to the temporal growth rate, however it strongly influences the perturbation phase speed phase. This influence appears in the shear agent's ability to cause convective/absolute transitions of the instabilities. It is also found that negative values of the shearing agent representing a counter-flowing shearing gas can completely suppress the inertial instability mode when sufficiently large in magnitude. As for the physical interpretation of the shear agent quantity, it is found that it has the same qualitative effects as that of a turbulent counter-flowing shearing

gas in a strong confinement setting matching [17].

Furthermore, the effect of the reduction in film height on the spatio-temporal stability of the flow was investigated and it was established that a thinner film is more prone to absolute instabilities since it is dominated by viscosity which resists the advection of the perturbations in the film.

The numerical simulation of the interface evolution was performed and validated against the linear stability analysis and existing literature, and confirmed the findings of the linear stability analysis.

Furthermore, Using a self-similarity analysis it is found that the shear agent does not affect the physical behavior of the film close to rupture, instead it is found that it delays rupture time and changes the rupture trajectory while the minimum film height is still close to its original value.

6.2 Outlooks

The investigation performed in this thesis can be expanded in several directions. The effect of the shearing gas in the short wave domain can be investigated by the formulation of the Orr-Sommerfeld eigenvalue problem, since it is expected from work done using the Nusselt scaling for the H-mode instability to persist in the short wave domain, despite being suppressed for long waves. Additionally, the interaction between a shearing gas and thermal instabilities in the short wave domain is quite an interesting problem that should further elucidate the dynamics of this problem.

Another avenue for expansion is the inclusion of the normal stress imparted by the shearing gas which was ignored in this investigation. A simplistic approach to include it is to extend the notion of a shear agent to that of a quantity which includes both the normal and shear components such that they are related via the interface unit vectors which are related through its spatial gradient $\partial_x h$.

Bibliography

[1] J. Humphrey and A. Siebert, "Separation technologies; an opportunity for energy savings," *Chemical Engineering Progress; (United States)*.

[2] S. L. Goren and R. Mani, "Mass transfer through horizontal liquid films in wavy motion," *AIChE Journal*, vol. 14, no. 1, pp. 57–61, 1968.

[3] D. Lucas, C. Caulfield, and R. R. Kerswell, "Layer formation in horizontally forced stratified turbulence: connecting exact coherent structures to linear instabilities," *Journal of Fluid Mechanics*, vol. 832, pp. 409–437, 2017.

[4] L. Lesshafft and P. Huerre, "Linear impulse response in hot round jets," *Physics of Fluids*, vol. 19, no. 2, p. 024102, 2007.

[5] P. Kapitza, "Wave flow of thin layers of a viscous fluid: Ii. fluid flow in the presence of continuous gas flow and heat transfer," *Zh. Eksp. Teor. Fiz*, vol. 18, no. 19, pp. 680–689, 1948.

[6] P. Kapitsa and S. Kapitsa, "Wave flow of thin layers of a viscous fluid. iii. experimental study of the wave flow regime," *Zh. Eksp. Teor. Fiz*, vol. 19, pp. 105–120, 1949.

[7] D. Goussis and R. Kelly, "Surface wave and thermocapillary instabilities in a liquid film flow," *Journal of Fluid Mechanics*, vol. 223, pp. 25–45, 1991.

[8] C. Normand, Y. Pomeau, and M. G. Velarde, "Convective instability: a physicist's approach," *Reviews of Modern Physics*, vol. 49, no. 3, p. 581, 1977.

[9] J. Pearson, "On convection cells induced by surface tension," *Journal of fluid mechanics*, vol. 4, no. 5, pp. 489–500, 1958.

[10] K. Smith, "On convective instability induced by surface-tension gradients," *Journal of Fluid Mechanics*, vol. 24, no. 2, pp. 401–414, 1966.

[11] J. P. Burelbach, S. G. Bankoff, and S. H. Davis, "Nonlinear stability of evaporating/condensing liquid films," *Journal of Fluid Mechanics*, vol. 195, pp. 463–494, 1988.

[12] J.-M. Delhaye, "Jump conditions and entropy sources in two-phase systems. local instant formulation," *International Journal of Multiphase Flow*, vol. 1, no. 3, pp. 395–409, 1974.

[13] H. J. Palmer, "The hydrodynamic stability of rapidly evaporating liquids at reduced pressure," *Journal of Fluid Mechanics*, vol. 75, no. 3, pp. 487–511, 1976.

[14] R. J. Briggs, "Electron-stream interaction with plasmas," 1964.

[15] A. Bers, "Space-time evolution of plasma instabilities-absolute and convective," in *Basic plasma physics. 1*, 1983.

[16] P. Huerre and P. A. Monkewitz, "Absolute and convective instabilities in free shear layers," *Journal of Fluid Mechanics*, vol. 159, pp. 151–168, 1985.

[17] R. Vellingiri, D. Tseluiko, and S. Kalliadasis, "Absolute and convective instabilities in counter-current gas–liquid film flows," *Journal of Fluid Mechanics*, vol. 763, pp. 166–201, 2015.

[18] S. Alekseenko, S. Aktershev, A. Cherdantsev, S. Kharlamov, and D. Markovich, "Primary instabilities of liquid film flow sheared by turbulent gas stream," *International Journal of Multiphase Flow*, vol. 35, no. 7, pp. 617–627, 2009.

[19] G. Lavalle, Y. Li, S. Mergui, N. Grenier, and G. F. Dietze, "Suppression of the kapitza instability in confined falling liquid films," *Journal of Fluid Mechanics*, vol. 860, pp. 608–639, 2019.

[20] M. J. Ablowitz, A. S. Fokas, and A. Fokas, *Complex variables: introduction and applications*. Cambridge University Press, 2003.

[21] G. F. Carrier, M. Krook, and C. E. Pearson, *Functions of a complex variable: Theory and technique*, vol. 49. Siam, 2005.

[22] P. Huerre and M. Rossi, "Hydrodynamic instabilities in open flows," *Collection alea saclay monographs and texts in statistical physics*, vol. 1, no. 3, pp. 81–294, 1998.

[23] D. Benney, "Long waves on liquid films," *Journal of mathematics and physics*, vol. 45, no. 1-4, pp. 150–155, 1966.

[24] S. Joo, S. H. Davis, and S. Bankoff, "Long-wave instabilities of heated falling films: two-dimensional theory of uniform layers," *Journal of Fluid Mechanics*, vol. 230, pp. 117–146, 1991.

[25] R. Kelly, D. Goussis, S. Lin, and F. Hsu, "The mechanism for surface wave instability in film flow down an inclined plane," *Physics of Fluids A: Fluid Dynamics*, vol. 1, no. 5, pp. 819–828, 1989.

[26] M. C. Dallaston, M. A. Fontelos, D. Tseluiko, and S. Kalliadasis, "Discrete self-similarity in interfacial hydrodynamics and the formation of iterated structures," *Physical review letters*, vol. 120, no. 3, p. 034505, 2018.

[27] S. Shklyaev, A. V. Straube, and A. Pikovsky, "Superexponential droplet fractalization as a hierarchical formation of dissipative compactons," *Physical Review E*, vol. 82, no. 2, p. 020601, 2010.